MAX PLANCK SCHOOL

matter to life

Smart boronic acid self-assembling peptide complexes and their biomedical potential

Master Thesis

Maximilian Schuler

First Examiner: Prof. Dr. Tanja Weil

Second Examiner: Prof. Dr. Job Boekhoven

30.11.2022

Abstract

Peptide nanostructures play a crucial role in nature and can be tailored for biomedical applications. Their inherent biocompatibility and versatility make them promising candidates for smart biomaterials. To make supramolecular nanostructures applicable *in vivo*, spatial-temporal control is a prerequisite and trigger-induced self-assembly can push this field forward. pH responsive depsipeptides commonly used to induce self-assembly on demand, expose a cryptic hydroxyl group upon pH neutralization possibly enabling reversible boronic ester formation. Combining pH-irreversible depsipeptide chemistry with reversible dynamic covalent bonds, facilitates the design of novel smart biomaterials. In this study, several self-assembling peptide fragments were synthesized and their ability to react with boronic acid (BA) derivates was investigated by ESI-MS, DOSY-NMR, ARS, MST and computational methods. To address the effect of multivalency, diboronic acid peptides and tetraserine peptide reaction partners were synthesized, and their binding affinities determined. To approach multivalency from a different angle, hydroxyl-presenting self-assembling peptides were synthesized. These peptides interacted with and partly released the boronic acid dye in a proof-of-concept drug release study which was established in this work. The concept was then transferred to build a self-healing hydrogel. This system, however, in which a bisboronic acid PEG-linker served as a peptide nanofibril cross-linker needs further optimization. Taken together, the study presented here, provides insights into binding affinities between BAs and peptides of different valency. This knowledge opens the door for follow-up experiments to make the translation towards biomedical applications.

Acknowledgments

First, I would like to thank Prof. Dr. Tanja Weil for giving me the opportunity to work in such an interdisciplinary, supportive, and inspiring laboratory. I especially enjoyed the international and friendly environment as well as the inspiring input from my colleagues.

I want to thank Prof. Dr. Job Boekhoven for reading and grading my thesis as a second examiner.

Special thanks also go to Dr. Christopher Synatschke as my day-to-day supervisor. I am very thankful for his valuable scientific input, for the general support and for the coordination of this project. His knowledge was very helpful to push this project forward.

Further I would like to thank Bellinda Lantzberg for introducing me to the synthesis of protected BAs and Marius Braun for his valuable support and proof reading of my thesis.

I want to thank Prof. Dr. Fernando Beragmini for conducting the DFT calculations and helping me with the computational part of this thesis. I would like to thank Dr. Manfred Wagner for measuring DOSY-NMR, Yu-Liang Tsai for providing the KIKI peptide material as well as measuring Maldi-TOF samples, Ali Rouhanipour for measuring LCMS, Jiaqi Xing for LCMS and TEM measurements, Ingo Lieberwirth and Katrin Kirchhoff for TEM sample measurements and all other people for helping me in the lab.

I want to thank my family and especially my girlfriend Ninon for supporting me during this last episode of my master studies. I am very thankful for their encouragement and psychological support.

Last but not least, I would like to say thank you to the MPS Matter to Life, the coordination team and the whole MtL network for making this work possible.

List of abbreviations

4CPBA	4-carboxyphenylboronic acid
AA	Amino acid
ABA	3-aminophenlyboronic acid
ARS	Alizarin red S
BA	Boronic acid
BAP	Diboronic acid peptide
BPA	4-borono-L-phenylalanine
CD	Circular dichroism
DFT	Discrete fourier transform
DOSY	Diffusion-ordered spectroscopy
ESI-MS	Electrospray ionization mass spectrometry
Fmoc-SPPS	Fmoc solid phase peptide synthesis
HPLC	High performance liquid chromatography
K_d	Dissociation constant
LCMS	Liquid chromatography-mass spectrometry
Maldi-TOF	Matrix-assisted laser ionization time of flight
MMP	Matrix metalloproteinase
MST	Microscale thermophoresis
NMR	Nuclear magnetic resonance
NOESY	Near oppenheimer effect spectroscopy
PF	Peptide fragment
PNF	Peptide nanofibril
RT	Room temperature
SAP	Self-assembling peptide
SAPF	Self-assembling peptide fragment
TEM	Transmission electron microscopy
TSP	Tetraserine peptide

Table of contents

1 Motivation

In the scope of this master thesis, a double pH-responsive peptide-BA strategy is developed to be exploited as hydrogel and drug delivery system. To date, to the best of our knowledge, the pH-responsivity of depsipeptides has not been considered for reactions with boronic acids (BA). The cryptic hydroxyl group that is exposed upon pH-neutralization could react with BAs to form acid labile boronic esters (Figure 1). Self-assembly and cross-linking of peptide nanostructures could be triggered simultaneously to afford new hydrogels with self-healing properties. On the other hand, hydroxyl presenting self-assembling peptide nanofibrils could form boronic esters with BA drug derivatives to enhance encapsulation efficiency and drug protective properties.

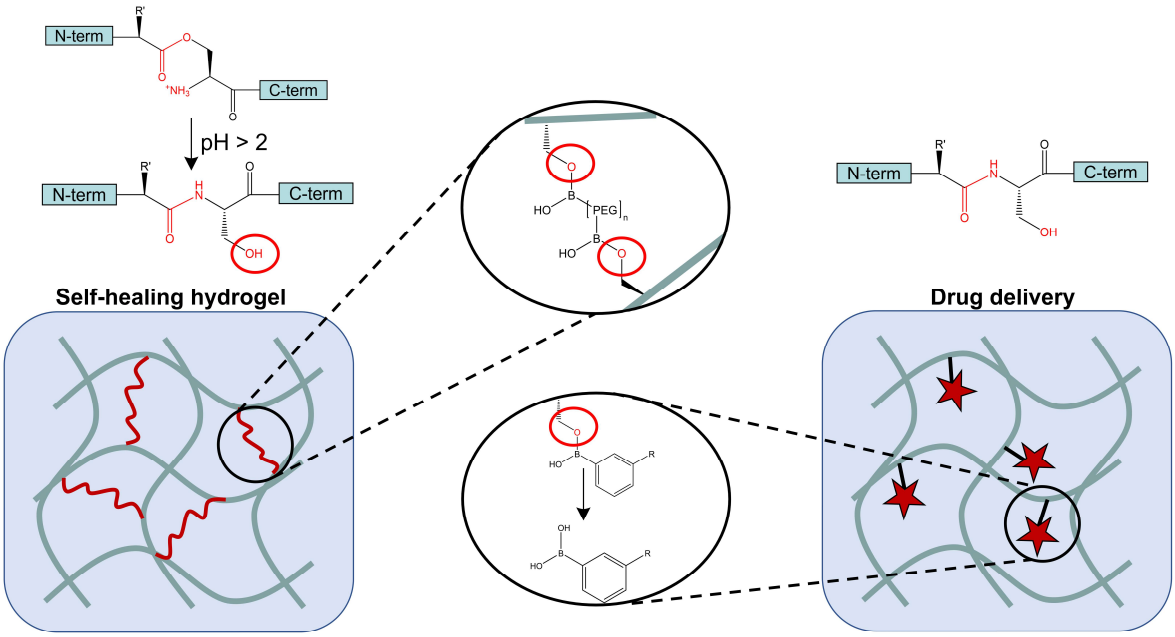

Figure 1: pH-responsive BA-depsipeptide complexes: Cryptic hydroxyl groups which are presented by depsipeptides upon pH neutralization react with BAs to afford self-healing hydrogels (left side). Hydroxyl presenting peptide nanofibrils can be used as drug delivery system and release BA-drugs at neutral pH (right side).

To approach this concept, molecularly dissolved self-assembly peptide fragments (SAPFs) are synthesized. The amphiphilic SAP sequence CKIKISQINM thereby serves as a building block for SAPF selection with varying amount of hydroxyl groups and spacer length. BA binding is investigated with ESI-MS, NMR methods, ARS displacement assays and MST measurements. On the other hand, computational

approaches are utilized to predict optimal structures for multivalent interactions between di- and tetraserine motifs and bisboronic acid peptides. Further, the effect of multivalency is examined experimentally by the ARS displacement assay and MST measurements. Sequences with promising binding affinities are coupled to the CKIK motif to afford nanostructures of different morphology. Using a proof of principle fluorescent BA molecule, drug encapsulation efficiency and release is investigated. Moreover, the gained insights from the fibril affinity assay are transferred to design a pH-responsive hydrogel that makes use of the reveal of the cryptic binding site. A linear bifunctional BA PEG cross-linker is synthesized and its impact on hydrogel stability investigated with the vial inversion test.

2 Introduction

2.1 Proteins in nature

Proteins play a crucial role in all living organisms. They are built from 21 natural amino acids (AA) by the ribosomal machinery in a very precise and controlled fashion to exert various relevant functions such as signalling, enzymatic reactions, or energy production to name a few [1]. Proteins are stabilized by their secondary, tertiary, and quaternary structure. The stabilizing intra- and intermolecular interactions cover the whole spectrum from weak dipole-dipole and π-π stacking in the lower kJ mol^{-1} range up to hundreds of kJ mol^{-1} for ion-ion interactions [2]. Supramolecular interactions between proteins which drive self-assembly to create higher ordered structures, is a key feature of life. Viruses for instance make use of protein self-assembly to build their virus shells and thereby encapsulate viral RNA. Membranes and DNA can only incorporate proteins and function as genetic code, respectively, after self-assembly has occurred. Tubulin and actin, central proteins of the cytoskeletal machinery, self-assemble into filamentous structures and thereby carry out cell division and molecule transport [3,4]. Self-assembly is hence ubiquitous in nature and therefore has been matter of active study for decades.

2.2 Self-assembling peptides

Proteins show very high complexity and their structural nature as well as their mode of interactions are poorly understood. Even though computational approaches have been developed, to date it is still impossible to design new structures on a protein level *in silico* [5] . This lack of information on a macromolecular level, has fostered the focus of research on smaller, better controllable molecules, peptides. Not only that the automated solid phase peptide synthesis (SSPS) opens the door for the incorporation of natural and unnatural amino acids with ease, but also the fact that peptides are inherently bioactive, biodegradable and ubiquitous in nature make them interesting for biomedical studies [1,6]. The synthesis on the solid phase allows the N-terminal elongation of oligopeptides by a condensation reaction between the carboxyl and the amine group of two AAs, catalysed by activator and activator bases. Orthogonal protection group chemistry ensures stable peptide synthesis with decent yields [7].

The peptide's sequence is directly related to its structure and rational design is required to achieve the desired function. By carefully balancing the intermolecular interactions

of AAs in a peptide the formation of higher-ordered nanostructures can be achieved through self-assembly [1]. Molecular self-assembly is a spontaneous phenomenon where individual molecules organize into higher-order supramolecular structures with long-range order. Driving forces for molecular self-assembly are ionic bonds, hydrophobic interactions, hydrogen bonding, dipole-dipole interactions, Van der Waals forces and π-π stacking [8]. Individual bond strengths of supramolecular interactions are comparably weak, but the accumulation of these interactions can give rise to stable nanostructures [1,9]. The type of nanostructures and the self-assembly propensity can partly be predicted by adapted theories from different fields, but the knowledge gap between the primary AA sequence and the final nanostructures is still not fully bridged [10,11]. Environmental parameters which influence the self-assembly process are peptide concentration, pH, ionic strength and the polarity of the surrounding medium as well as temperature [12]. Even though the impact of these triggers are not finally understood, the versatility and bioactivity of the peptide nanostructures led to various applications in regenerative medicine [13–15].

2.3 Self-assembling peptide design and nanostructures

The pool of natural and unnatural amino acids represents a versatile toolbox for self-assembling peptide designs and several motifs of different complexity have been exploited to form distinct nanostructures.

Dipeptides represent one of the simplest designs currently available. The diphenylalanine sequence FF, specifically, has gained increased attention as the core recognition motif of the Alzeimer's amyloid peptide [16]. FF itself shows self-assembly into highly-ordered tubular structures in aqueous solution [17]. N-terminal Fmoc based modification allows the application as a hydrogelator (Figure 2) [18,19].

Heptad sequences, in turn, display a more complex AA sequence. Their motif is based on a abcdefg repeat with a and d being nonpolar residues and the other residues being polar [20,21]. Alpha helical fibrous structures with collagen-like properties are obtained (Figure 2) [2,22].

β- hairpin peptides exhibit two interlinked peptide sequences that are connected by proline residues which results in the characteristic β- hairpin structure. The most common motif is the MAX1 motif [$(VK)_4V^D$ PPT-$(KV)_4$-NH_2]. Hydrogen bonding and

hydrophobic association stabilize β- sheet formation and causes nanofibril formation (Figure 2) [23]. The fibrillar nanostructures were utilized as antibacterial dressings [24].

Inspired by the structural features of Z-DNA, the Zhang group has developed self-complementary peptides. This class of peptides often possesses derivatives of the sequence $[X\text{-}Y\text{-}Z\text{-}Y]_n$ with X being a positively charged, Y hydrophobic and Z being a positively charged residue. Self-complementary RADA16 peptides were reported to assemble into nanofibers and were applied as drug carrier and hydrogels (Figure 2) [25,26].

Surfactant-like peptides represent another type of building block. They possess a $(X)_6Y_{1\text{ or }2}$ AA motif, where X represents an nonpolar AA such as alanine and Y being a polar or charged AA (Figure 2) [27]. Peptide amphiphiles with alkyl groups expand the hydrophobic part on the N-terminus further by the coupling of fatty acids. In aqueous solutions, these self-assembling peptides readily collapse to shield their hydrophobic core from the surrounding polar solvent. The resulting nanostructures is thereby strongly dependent on the structure of the hydrophobic tail and the headgroup and hence also on the packing parameter.

$$P = \frac{V_o}{a l_0}$$

The packing parameter is a function of V_o, the volume and a, the equilibrium area of the hydrophilic head group as well as l_o, the length of the hydrophobic tail. With increasing packing parameter, the morphology changes from curved structures to more planar structures [28]. Multiple equilibrium structures such as nanotapes, nanotubes, micelles, vesicles and nanofibers have been reported and exploited as drug delivery systems (Figure 2) [14,15].

Amphiphilic peptides possess a pattern with alternating hydrophilic and hydrophobic residues. This regularity promotes the formation of stable cross β- sheets into well-defined nanofibrils and the motif CKFKFQF was shown to enhance neuronal activity of the peripheral nervous system (Figure 2) [29].

	Peptide design	Self-assembly and nanostructure
Fmoc-FF	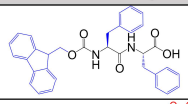	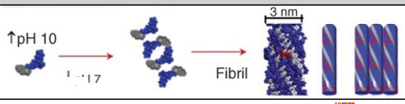
$[HRG]_4[POG]_4[EPG]_4$	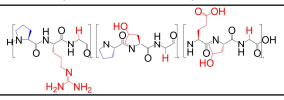	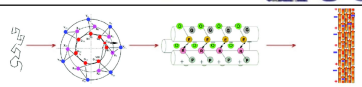
MAX1	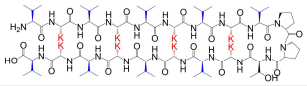	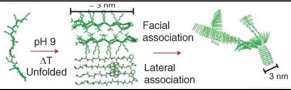
RADA	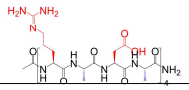	
V_6D	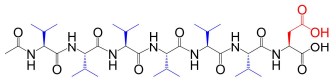	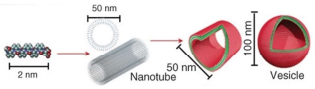
K_3PA	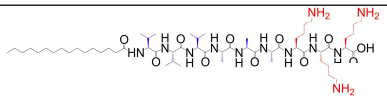	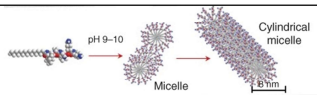
CKFKFQF	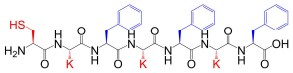	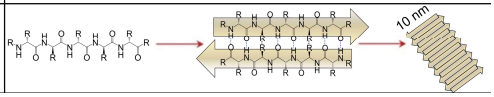

Figure 2: Selection of SAP designs: The selection comprises structures, mode of assembly and the corresponding nanostructures of dipeptides (Fmoc-FF), heptad motif peptides ($[HRG]_4[POG]_4[EPG]_4$). β-hairpin peptides (MAX1), self-complementary peptides (RADA), surfactant-like peptides (V_6D), peptide amphiphiles (K_3PA) and amphiphilic peptides (CKFKFQF). Structures which drive self-assembly are colour labelled accordingly (hydrophobic blue, hydrophilic red). Structures, mode of assembly and nanostructures were extracted and or adopted from [1,22,29].

As can be seen, the versatility offered by the pool of natural AA in particular is already enormous, and this selection represents only a small part of the established peptide designs. Introduction of unnatural AA such as β - AA opens the door for new peptide nanomaterials with higher resistance towards degradation and new nanostructures [30]. Outlining this, however, would exceed the scope of this work.

2.4 Scope amphiphilic peptides

2.4.1 Self-assembly of amphiphilic peptides

As described previously, the design of amphiphilic peptides relies on an alternating motif of hydrophilic and hydrophobic residues. The alternation causes the hydrophilic residues to phase in one, the hydrophobic residues to the other direction (Figure 3).

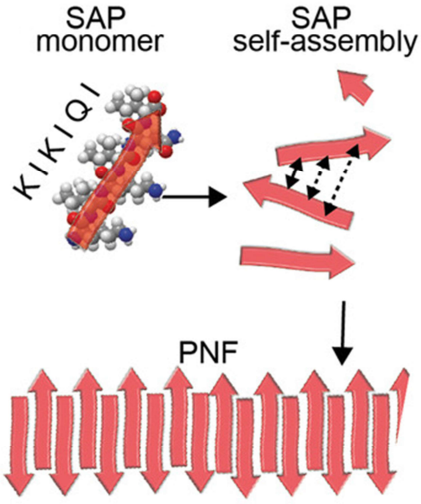

Figure 3: Mode of amphiphilic peptide self-assembly: Attractive forces of SAPs between AA residues of the same hydrophilicity drive β-sheet formation. Stacking of antiparallel β-sheets builds up peptide nanofibrils (PNF). Extracted and adapted from [29].

The packing of monomeric peptide molecules into 3D nanostructures is governed by intermolecular hydrogen bonding and shielding of hydrophobic residues from the aqueous solution. Antiparallel β-sheet formation occurs perpendicularly to the direction of fibril lamination and extension [31].

Models have been developed to simulate the peptide fibril formation. They predict a nucleation-driven elongation process. The formation of the nanofibril starts with an initial nucleation process (Figure 4).

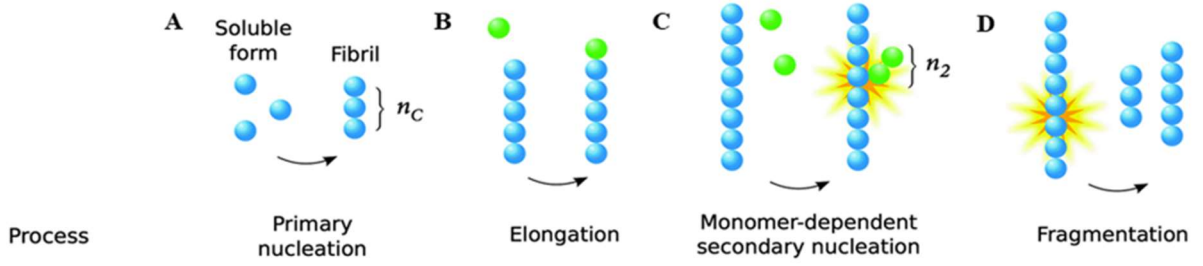

Figure 4: Model of the nucleation and peptide nanofibril formation process: Primary nucleation of monomeric peptides leads to a longitudinal elongation of the peptide nanofibril. Secondary nucleation and fragmentation processes can follow. Extracted and adapted from [32] .

An elongation process leads to peptide stacking into nanofibrils [33]. Due to the dynamics of the supramolecular network, a monomer-dependent secondary nucleation

can follow where new monomers integrate inside the peptide fibril [32]. Fragmentation into smaller fibril can occur.

2.4.2 CKIKI-a versatile amphiphilic motif

As outlined before, amphiphilic peptide motifs can assemble into higher order nanostructures. Derivatives of the CKIKI motif have been studied extensively for years in our research group. Modified sequences of this amphiphilic peptide were shown to boost viral gene transduction. Yolamanova et al. proofed that the HIV envelope protein derived enhancement factor EF-C (QCKIKQIINMWQ) self-assembles in well-defined positively charged nanofibrils [34]. By presumably bridging the gap between virions and cells, EF-C successfully competed with the frequently used transduction enhancer RetroNectin. Further insights into the structure-activity relationship of EF-C were gained by optimizing EF-C derivative sequences towards their best transductional efficiency. It was shown that cross β-sheet structures and positively charged residues are essential for retroviral gene transfer [35]. Sequence optimization yielded three promising short peptides (CKFKFQF, CKFKFQFNM, CKIKIQINM) with high conversion rates and high infectivity rates. The despipeptide derivative CKIKI(O-C(O))SQINM was grafted on denatured HSA to form physical cross-links in a self-healing hydrogel [36]. Upon pH neutralization, the amphiphlic peptide expands into peptide nanofibrils which interlock HSA molecules to achieve a sol-gel transition. Since CKIKI(O-C(O))SQINM is known to form nanofibrils under various conditions and has high bioactivity as well as low toxicity, derivatives of this sequence were used in this study.

2.5 Trigger-induced assembly strategies of peptides

To push peptide nanomaterials towards clinical applications, trigger-induced self-assembly strategies are required to design smart materials. The peptide sequence can be design such that environmental parameters serve as external triggers to induce a morphology and thus bioactivity change on demand. Nanomaterials which respond to external stimuli increase spatial-temporal control. The trigger can be of different nature.

Temperature induced self-assembly relies on elastin-like peptides which can form micelles through temperature change [37,38]. FF dipeptides also change their self-assembling properties through temperature cycles [39]. Besides temperature-induced

self-assembly, enzymatic approaches have been studied as well. Thermolysin, Subtilisin, Phosphatases and Chemotrypsin were shown to promote self-assembly by methyl-ester hydrolysis, condensation or dephosphorylation reactions of short aromatic peptides [40]. Drug release was as well achieved by this [41]. Photo-induced self-assembly processes represent another promising strategy towards smart materials. Photoacid generators or photo-switchable azobenzenes have been employed for this purpose [42,43]. Redox-sensitive strategies often include cysteine residues which form reversible disulfide bonds in response to their redox environment [44,45]. Another approach is pH-sensitivity which is mostly governed by charged AA residues that change their physicochemical properties upon pH change [46]. Materials can be tuned such that minor pH changes lead to drastic changes in nanostructure [47].

Depending on the final application, irreversible switches can be desirable for which different molecular designs are necessary. pH-responsive depsipeptides are one possible candidate. In depsipeptides which are naturally occurring in algae and cyanobacteria and are usually used to avoid aggregation during SPPS, a peptide bond is substituted by an ester bond (Figure 5) [48,49].

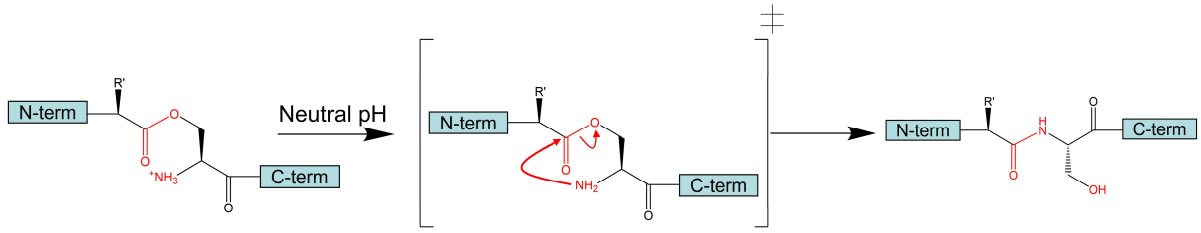

Figure 5: pH dependent linearization of depsipeptides: The hydroxyl group of serine or threonine can react with carboxylic acids of another AA in an esterification reaction to afford an ester bond. This ester bond leads to a kinked structure of a molecule that is reversed upon N-terminal deprotonation of serine or threonine at pH > 2. An intramolecular O,N-acyl shift linearizes the peptide.

Under acidic conditions (pH < 2) the ester bond causes a kink in the peptide structure which hinders it from self-assembling (Figure 5). When the pH value becomes higher than 2, the deprotonation of the N-terminus of serine or threonine occurs. The amine group acts as a nucleophile towards the ester group which results in the peptide bond formation. Positioning the responsive AA at a specific position centrally of the peptide, renders the peptide pH responsive. However, depending on the application, a pH

switch at pH 2 can be unfavourable. To expand this concept to broader pH ranges, caging groups can be introduced.

2.6 Suitable caging groups for depsipeptides

Caging groups find application where spatial-temporal control is desirable. The uncaging can be achieved by enzymes, light or altered redox environment. Glutamate for instance was successfully caged at the side chain and n-terminus (Figure 6).

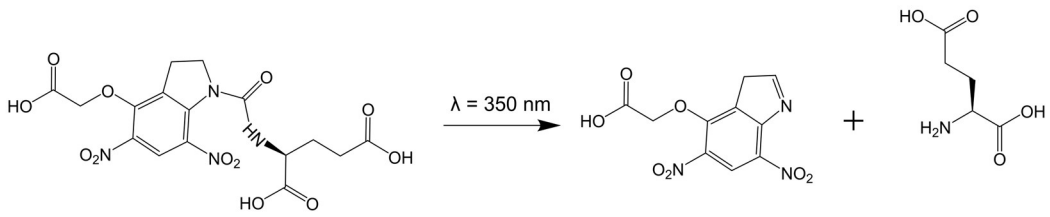

Figure 6: Photo-induced uncaging of glutamate. Upon UV-irradiation, the caging group is removed and glutamate is being released [50].

UV-irradiation resulted in the cleavage of the caging group and the controlled release of glutamate in mouse hippocampi [50]. Caging a serine or a threonine containing depsipeptide on its N-terminus would provide orthogonal sensitivity towards light and pH. However, the study also showed that the uncaging process for N-terminal caged glutamates is slower compared to sidechain protected glutamate. Nitrobenzyl derivatives could probably help to overcome this problem. 2-nitrobenzyl groups for example were already covalently attached in the centre of peptide amphiphiles to induce morphology changes upon irradiation [51].

Besides light-modulated uncaging strategies, enzymatic reactions could be used as well.

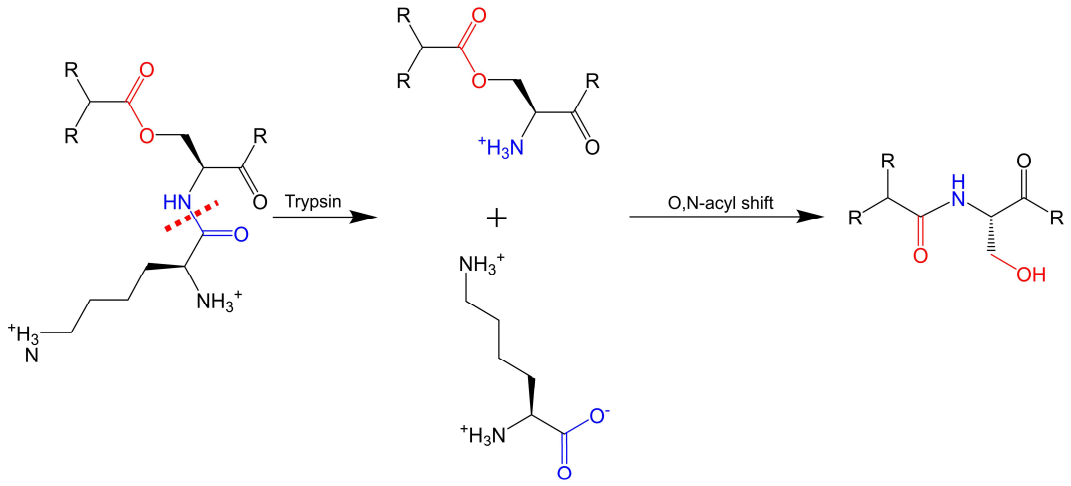

Figure 7: Enzyme mediated uncaging of depsipeptides: Lysine expands serine at its N-terminus. Upon addition of trypsin, the peptide bond is cleaved, making the N-terminus of serine accessible. The intramolecular O,N-acyl shift linearizes the peptide. Inspired by unpublished results from John Matson.

By expanding the N-terminus of the serine or threonine with specific AAs, an enzymatic cleavage reaction could uncage the intramolecular O,N-acyl shift (Figure 7). A straightforward method would be to extend the serine in N-terminal direction with a trypsin sensitive AA arginine or lysine. However, targeted and cell specific uncaging would require enzyme cleavage motifs sensitive to enzymatic biomarkers. For cancer cell treatment for instance, it would be necessary to design the N-terminal domain to be cleavable by matrix metalloproteinase or cathepsin B [52].

Redox sensitive strategies represent another possible option. Work has been published on H_2O_2 sensitive boronic acid caging groups.

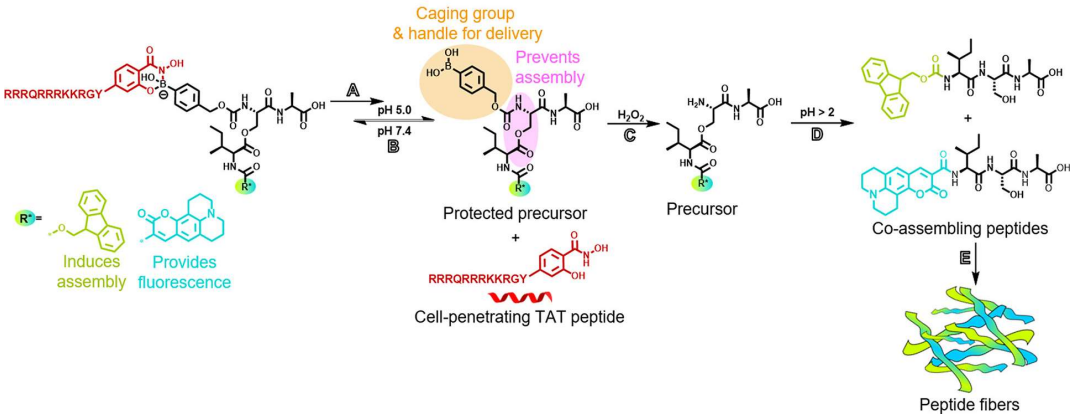

Figure 8: Redox-sensitive depsipeptide caging strategy: First, salicylhydroxamate-TAT is hydrolysed by the acidic microenvironment (step A). The boronic acid caging group is then cleaved by intramolecular H_2O_2 (step C) which triggers the molecular rearrangement of the despipeptide (step D) and fibre formation (step E). Extracted and adopted from [53].

A salicylhydroxamate-TAT sequence was attached to a boronic acid carbamide caged depsipeptide. By decreased pH of the cancer cell, the TAT sequence was hydrolysed and cleaved. Increased intracellular H_2O_2 concentrations cleaved the carbamide bond of the boronic acid caging group which induced the O,N- acyl shift and molecular self-assembly [53].

2.7 Boronic acids

2.7.1 Boronic acids and their mode of binding

Boronic acid derivates have been implemented for several biomedical purposes. They find application in glycoprotein purification, as hydrogen peroxide or sugar sensors as well as catalysts in several cross-coupling reactions [54–57]. The tendency to establish dynamic covalent bonds with nucleophiles render them a versatile character. This bond can reversibly be broken by acids or competitive molecules. The p-orbital which is orthogonal to the planar geometry of tridendate boronic acids allow the molecule react as mild Lewis acids with nucleophiles such as oxygen, sulfur, nitrogen and phosphorus with different denticity [58]. They show high tendency to bind vicinal nucleophiles like diols or catechols. Depending on the denticity, the boronic acid either resembles a trigonal planar or tetrahedral structure with one negative charge in aqueous solution (Figure 9).

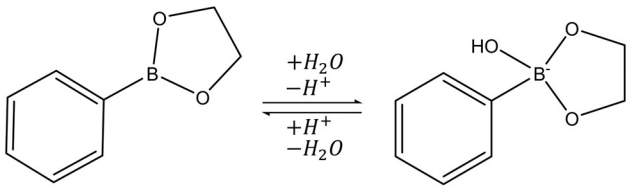

Figure 9: BA in aqueous solutions: Depending on the denticity, BAs show either a trigonal planar (left) or tetrahedral conformation (right). Inspired from [58].

2.7.2 Boronic acid binding affinities

The binding affinity of boronic acids towards nucleophiles is dependent on several parameters. Not only buffer composition, pH and temperature play a role, but also the chemical nature of the boronic acid compound and its ligand is determining the binding strength [59].

The electron-density of the boron and of the ligand are critical parameters to be controlled to increase the binding affinity. The more electron-deficient the boron molecule and the more electron-rich the ligand, the stronger the resulting interaction. Steric hindrance plays as well a role since less bulky interaction partners contribute to stronger binding affinities [58].

Additional stabilizing effects such as keto-enol tautomerism of molecules adjacent to the boron atom can result in higher binding affinities [59]. Worth mentioning is also salicylhydroxamate which represents a potent boronic acid binder. Since it can form stable complexes with BA in a five- or six-membered ring, it shows increased binding affinities as compared to natural saccharides and amino acids [60].

The concept of multivalency seems to play another important role for tuning boronic acid binding affinities [61,62]. Expanding the number of BAs from one to three in a peptide, increased the binding affinity towards catechol 70-fold as determined by microscale thermophoresis (Figure 10) [61].

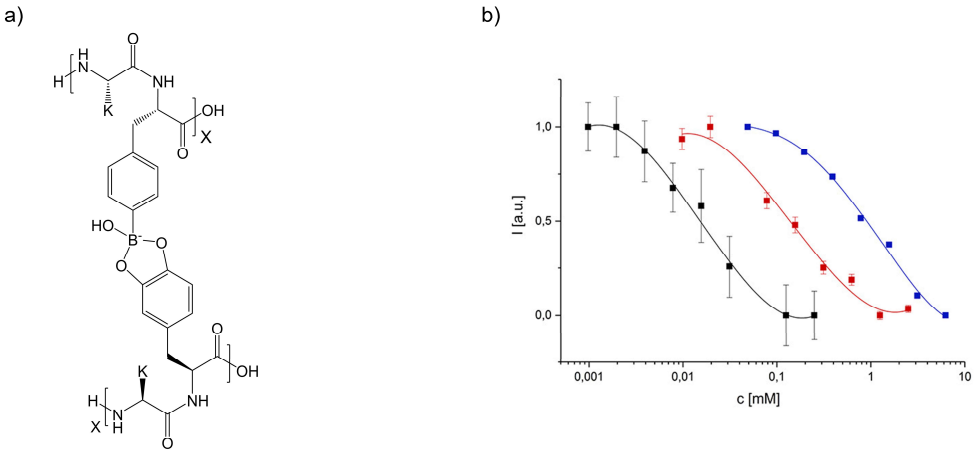

Figure 10: The effect of multivalent BA-catechol peptide binding: (a) Molecular structures of BA and catechol containing peptide tags where X indicates the number of repeating units with X=1 corresponding to $(AX)_1$.- $(BX)_1$, X=2 to $(AX)_2$ - $(BX)_2$ and X=3 to $(AX)_3$.- $(BX)_3$. (b) Microscale thermophoresis binding curves of monovalent (blue), divalent (red) and trivalent (black) reaction partners in PB 300 mM, pH 7.4. Extracted and adapted from [61].

Saccharides and sorbitol show association constants 70-fold and 35-fold lower than the trivalent complex, demonstrating that rational design of the binding partners can push the binding affinities tremendously [59].

Another study has shown that boronic acids of defined geometry can bind to tetraserine motifs [63]. A rhodamine-derived bisboronic acid was used as a reporter molecule (Figure 11).

a)

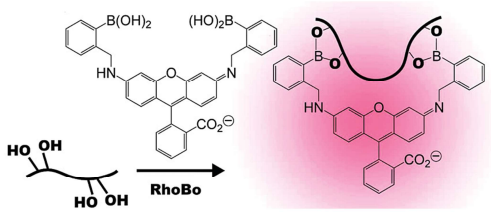

b)

		$K_{app}(\mu M)$		$K_{app}(\mu M)$
1	Ac-WD**SS**PG**SS**K-NH_2	0.45 ± 0.11	**Gal**	29,000 ± 5,000
2	Ac-WDAAPGG**SS**K-NH_2	No ΔF	**Glc**	13,000 ± 3,000
3	Ac-WD**SS**P**SS**K-NH_2	No ΔF	**Man**	29,000 ± 6,000
4	Ac-WD**SS**K**SS**K-NH_2	No ΔF	**Fuc**	445,000 ± 16,000
5	Ac-WD**SS**PGG**SS**K-NH_2	No ΔF	**Sia**	21,000 ± 4,000
6	Ac-WD**SS**GG**SS**K-NH_2	No ΔF	**GlcNAc**	No ΔF
7	Ac-WD**TT**PG**TT**K-NH_2	No ΔF	**CHD**	No ΔF
8	Ac-WD**YY**PG**YY**K-NH_2	No ΔF	**10**	0.35 ± 0.23
9	Ac-WD**DD**PG**DD**K-NH_2	No ΔF		

Figure 11: Binding of bisboronic acid to tetraserine motifs: (a) Molecular design and proposed mode of binding of RhoBo to tetraserine motifs. (b) Selection of designed peptide molecules as potential target binders and control molecules with the respective apparent association constants. Extracted and adapted from [63].

Spacing of the peptide motifs as well as the number of serine residues had to be critically controlled to induce fluorescence upon binding. The binding affinity was increased up to 100 k-fold compared to saccharide molecules. Interestingly, when the tetraserine motif was substituted by tetrathreonine motifs, no fluorescence was detected. This illustrates the steric demands placed upon BA binders.

2.8 Biomedical applications

2.8.1 Self-healing hydrogels

Hydrogels have gained increased attention in tissue engineering over the last decades. Their hydrophilicity, porous structure, high swelling properties and nutrient storage capacities make them promising candidates for regenerative medicine. Frequently exploited as ECM mimics, they provide physical and chemical support for various cell types [64]. Initial approaches have been focused on covalently cross-linked hydrogels which yielded nanometre-sized pore hydrogels, often cross-linked under harsh conditions [65,66]. However, in order to provide optimal support for cellular outgrowth, it is necessary that the hydrogel's design facilitate cell-matrix interaction and ECM remodelling.

To obtain systems that resemble the natural cell niche, physically cross-linked hydrogels have been developed. Building blocks which form supramolecular networks come with high dynamics and self-healing properties. By making use of these dynamics, the designed systems come one step closer towards the natural ECM [67]. Supramolecular building blocks utilize host-guest chemistry, hydrogen bonding, metal ligand complexation and hydrophobic interactions, to name a few [68–71]. The conversion from amphiphilic peptides into peptide nanofibrils was widely used to design potent hydrogelators [72]. Exceeding the critical hydrogelation concentration allow high aspect ratio nanofibrils to entangle to build fibrous ECM-like structures on the micrometer scale. The supramolecular nature of the ECM mimic promotes cell-growth and proliferation [31,73,74].

Hydrogel designs which rely on dynamic covalent bonds as cross-links have been studied as well. Reversible exchange reactions of disulfide bonds, for instance, were already utilized as hydrogel cross-linkers [75]. However, since the thiol-disulfide bond equilibrium time is very long, cytotoxic oxidants such as H_2O_2 must be used [76].

Boronic esters were exploited as cross-links in reversible addition and condensation reactions. Using catechols to complexate BAs represent one approach towards dynamic covalent hydrogels [77–79]. Work on hybrid materials where phenylboronic acid was grafted on cellulose and bound to PVA to build biocompatible, self-healing and ion conductive hydrogels has been reported as well [80]. Yang et al. published interesting work on boronic esters in combined network. Phenylboronic acid and benzaldehyde were coupled to a multifunctional PEG molecule. With the addition of glycol and chitosan, boronic esters as well as imines could be formed which rendered the hydrogel its self-healing properties [81].

2.8.2 Peptide nanofibrils as drug delivery system

Rational design of biomaterials is required to obtain spatial-temporal control of drug release *in vivo.* In general, the drug-loading efficiency of the carrier should be high, and the drug must not leak while circulating inside the body [32]. The respective carrier must protect the active compound maintaining its activity, stability and thereby reduce its toxicity. Moreover, the drug must be released and interact in a cell-specific manner without showing adverse effects to adjacent cells [32]. After drug release, body clearance without causing side-effects needs to occur.

SAPs have already been applied as nanocarriers for drugs. They show superior drug loading and drug protective properties as compared to traditional nanoparticles or liposomes [72,82,83]. The structure of the nanometre-sized material strongly affects the biodistribution and drug loading performance. Peptide nanofibers have ten times longer circulation times than peptide nanoparticles. Furthermore, the drug release of nanofibers is prolonged, and NP’s suffer from low encapsulation efficacy [32].

2.8.2.1 Drug delivery strategies

The type of drug delivery is governed by the assembling strategy of the peptide nanomaterial. Peptide nanofibrils which were self-assembled *ex vivo* can encapsulate bioactive substances and be delivered to cancer sites through body circulation. Maligne growth properties of cancer cells lead to gaps between cancer endothelial cells which facilitate the accumulation of nanomaterials via the passive enhanced permeability and retention effect [84]. However, this delivery strategy is only applicable for tumors larger than 4.6 nm in diameter [85]. Doping the peptide nanostructures with

aptamers, antibodies or other tumor specific molecules improve the enrichment of the nanocarrier [32].

More recent work utilizes the self-assembly of peptide nanofibrils itself to induce cytotoxic effects. The reverse-assembly approach lets the nanofibrils form inside specific cells to disrupt metabolic pathways [32].

2.8.2.2 Drug encapsulation strategies

Drug incorporation can be achieved through different approaches. Drugs are frequently encapsulated by peptide amphiphiles. The interaction between the nanofibrils and the drug is often unspecific in nature and the active substance is either released by diffusion or disruption of peptide nanofibrils [72,86–88].

Acid-labile boronic esters have been utilized for nanocarriers as well. In one study, a polydopamine building block was co-assembled with a phenylboronic acid decorated hydrophobic building block. The resulting micelles were able to physically encapsulate the hydrophobic drug Doxorubicin. In the acidic environment of the cell, micelle disruption and burst release of Doxorubicin led to cytotoxic effects [89].

However, to date, there is comparably little work on peptide nanocarriers which react with drugs through reversible chemical bonds. Specific interactions between nanocarriers and their drugs could potentially outcompete physically trapped systems in terms of drug-loading efficiency and drug protective properties. One example was published by Cao et al. [83]. Six surfactant-like peptides with different nanostructures were synthesized and their ability to condensate DNA via electrostatic interactions was investigated. The authors suggest a two-step mechanism where the DNA first interacts with via electrostatic interactions with the peptides. This nucleation then promoted hydrophobic interaction between monomeric peptides molecules inducing self-assembly.

In another study, researchers were able to release bortezomib, a boronic acid derived dipeptide anticancer drug, by means of a catechol-based polymer (Figure 12).

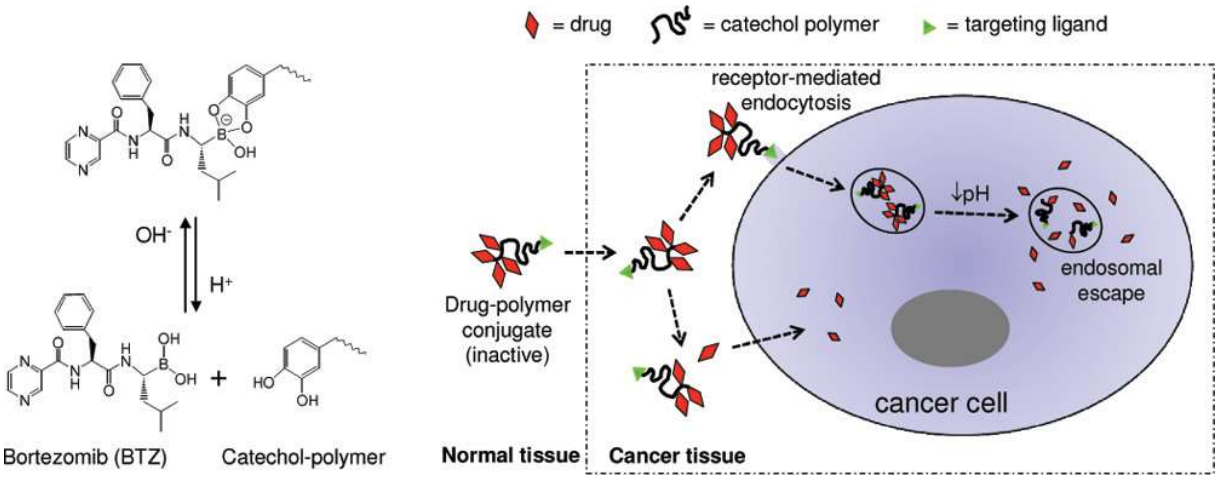

Figure 12: Drug delivery through reversible chemical bonds: Bortezomib was complexated by a catechol-polymer. After internalization of the drug-polymer conjugate, decreased environmental pH released the drug in maligne cancer cells. Extracted from [90].

The boronic ester facilitated the encapsulation of Bortezomib which was cleavable under acidic pH conditions [90]. After receptor-mediated endocytoses, the decreased pH in cancer cells released the drug from the drug-polymer conjugate, diminishing survival of breast cancer cells.

3 Materials and Methods

3.1 List of chemicals

All chemicals were purchased with highest quality and no further purification has been done if not stated otherwise.

Dimethylsulfoxide-d_6 (DMSO-d_6, CAS: 2206-2-1, Sigma-Aldrich); trifluoroacetic acid (TFA, CAS76-05-1, Thermo-Scientific);4-Borono-L-phenylalanine (BPA, CAS: 76410-58-7,Molekula);acetonitrile (ACN, CAS: 75-05-8, Honeywell); dimethylsulfoxide (DMSO, CAS: 67-68-5, Sigma-Aldrich); ammoniumbicarbonate buffer (ABC buffer, CAS: 1066-33-7, Sigma-Aldrich); uranyl acetate (CAS: 6159-44-0, Merck), Fmoc-Gly-Wang ((100-200 mesh) CAS: 65307-63-1, Novabiochem ®), Fmoc-Lys-(Boc)-Wang ((100-200 mesh) CAS: 65307-53-1, Novabiochem-®); Fmoc-Met-Wang ((100-200 mesh) CAS: 04-12-2058, Novabiochem ®); side and n-terminal protected AA (Novabiochem ®); *N,N'*-Diisopropylcarbodiimide (DIC, CAS: 693-13-0, TCI); OxymaPure (Oxyma, CAS: 3849-21-6, Matrix Innovation); *N,N*-Diisopropylethylamine (DIPEA, CAS: 7087-68-5, Sigma-Aldrich); Benzotriazole-1-yl-oxy-tris-pyrrolidino-phosphonium hexafluotophosphate (PyBOP, CAS: 128625-52-5, Sigma-Aldrich); piperidine (CAS: 110-89-4, Carl Roth); dichloromethane (DCM, CAS: 75-09-2, Fisher Chemicals); methylboronic acid (CAS: 13061-96-6, Alfa Aesar); diethylether (CAS: 60-29-7, Honeywell); Tris(2-carboxyethyl)phosphine hydrochloride (TCEP, 51805-49-9, Sigma-Aldrich), Fluorescein-5-maleimide (Fluorescein-maleimide CAS: 75350-56-8, Biomol); Fmoc-AEEAc (Fmoc-AEEAc, CAS: 166108-71-0, Carbolution); 3-aminophenylboronic acid (ABA, CAS: 30418-59-8, Sigma-Aldrich); sodium bicarbonate (CAS: 144-55-8, Sigma-Aldrich); magnesium sulfate (CAS: 22189-08-8, Fisher Chemicals); alizarin red S (ARS, CAS: 130-22-3, VWR chemicals); NHS-Fluorescein (5/6-carboxyfluorescein succinimidyl ster)(Fluorescein-NHS;CAS:117548-22-8,ThermoFisher Scientific); sodium hydroxide (NaOH, CAS: 1310-73-2, Sigma-Aldrich); hydrochloric acid (HCL, CAS: 7647-01-0, Sigma-Aldrich); tetrahydrofuran anhydrous (dry THF, CAS: 109-99-9); toluol (CAS: 108-88-3, Thermo Scientific); (1S,2S,3R,5S)-(+)-pinanediol (Pinanediol, CAS: 18680-27-8, Sigma-Aldrich); petrolether (PE, CAS: 1013161-46-5, Sigma-Aldrich); 4-carboxphenylboronic acid (4CPBA, CAS: 14047-29-1, Agros Organics); N-(9-Fluorenylmethoxycarbonyloxy)succinimide (Fmoc NHS,

CAS: 82911-69-1, Novabiochem ®); tetrahydrofuran (THF, CAS: 203-726-8, Honeywell); ethylacetate (EA, CAS: 141-78-6, Sigma-Aldrich); acetic acid (CAS: 64-19-7, Fisher Chemicals); fructose (CAS: 57-48-7, Sigma-Aldrich).

3.2 Characterization methods

3.2.1 NMR and DOSY-NMR

^{1}H NMR spectra were recorded by a 400 MHz ^{1}H NMR spectrometer (Bruker). 2 to 7 mg material of interest was dissolved in 600 µL of DMSO-d_6. 32 scans were chosen as default measurement. ^{1}H NMR spectra were calibrated to the DMSO-d_6 signal (δ = 2.50 ppm).

For DOSY-NMR of BA compounds, 2.53 µmol of peptide material and 2.53 µmol of BPA were pre-dissolved in 30 µL of DMSO-d_6 each. After merging the two solutions, 540 µL of ABC buffer 11.1 mM was added. As a reference, peptide and BA solutions with only DMSO-d_6 were prepared.

^{1}H and DOSY spectra for BA binding studies were recorded on a 500 MHz Bruker spectrometer using water suppression. These measurements were conducted by Dr. Manfred Wagner.

3.2.2 Maldi-TOF

If not stated otherwise, at least 50 nmol of material was dissolved in 0.1 vol% TFA in pure MilliQ (MQ) water (MQ was always used for this purpose). The samples were crystallized by adding 1 vol equivalent of α-cyano-4-hydroxycinnamic acid matrix solubilized in 0.1 vol% TFA in MQ and ACN (1:1 vol/vol). After mixing, 1 µL of the solution was applied on the target plate. Maldi-TOF measurements were conducted by Stephan Türk and Yu-Liang Tsai. Spectra were recorded on a Bruker Reflex III spectrometer.

3.2.3 LC-MS

LCMS was recorded on a Shimadzu LC-MS 2020 device. Samples were dissolved at 0.5 mg mL^{-1} in MQ water. Moderately soluble compounds were centrifuged for 15 min at 13.8 k rpm (high speed table centrifuge) and the supernatant injected for analysis. Samples possessing auto-fluorescent properties were measured with a detector wavelength of 254 nm and 214 nm. Samples lacking this property were measured with

a detector wavelength of 190 nm and 204 nm. Column: Shimadzu Kinetex 2.6 µm EVO C18 100 Å LC 50x2.1 mm. Measurements were conducted by Ali Rouhanipour and Jiaqi Xing.

3.2.4 TEM

TEM samples were first dissolved at 10 mg mL^{-1} in DMSO and then diluted 1:9 (vol/vol) in ABC buffer 11.1 mM pH 7.4 to a final concentration of 1 mg mL^{-1}. After 12 h of incubation at 37 °C (400 rpm on thermoshaker), the samples were quickly centrifuged (table centrifuge) and 5 µL were applied on a formvar-layer coated copper grid. After 10 min of incubation, the excess solution was removed with a filter paper. The active surface of the grid was then deposited on 10 µL of a 4 vol% uranyl acetate solution to improve sample contrast (5 min of incubation). The excess solution was again removed, and the grids washed 3 times with MQ. After final removal of excess solution, the grids were stored at RT until further use. TEM measurements were performed by Jiaqi Xing, Katrin Kirchhoff and Ingo Lieberwirth.

3.2.5 CD

CD samples were prepared at 1 mg mL^{-1} in MQ and incubated overnight at 37 °C (400 rpm on thermoshaker). Samples were quickly centrifuged (table centrifuge). Data was acquired from 260 nm to 180 nm on a JASCO J-1500 device. To assess whether dilutions are applicable at 180 nm wavelength, the HT-value was measured, and the material diluted accordingly such that the HT value would not exceed 800 (100 µM for investigated peptides). Samples were measured at 25 °C with a bandwidth of 1 nm, a D.I.T. value of 1 sec, a data pitch of 0.1 and a scanning speed of 10 nm min^{-1}. Spectra were blank (MQ) subtracted and smoothened twice with the binomial smooth function (JASCO Spectra Manager II). For secondary structure analysis, the PLS computation was chosen.

3.3 Synthesis

3.3.1 SPPS

All peptides were synthesized using standard Fmoc-SPPS on a CEM Liberty Blue Automated Peptide Synthesizer. 0.1 mmol scales were used for all peptides. Preloaded Wang resins (Fmoc-Gly-Wang, Fmoc-Lys-(Boc)-Wang, Fmoc-Met-Wang) were swollen for 1 h at RT in DMF and then transferred to the SPPS reaction vessel.

AA were dissolved in appropriate amount of DMF and sonicated for 5 min. DIC (0.5 M) and Oxyma (1.0 M) served as activator and activator base, respectively. Standard coupling procedures were applied for all SPPS steps:

Deprotection:

- Add 20 vol% piperidine in DMF (10 mL), heat to 70 °C for 25 s, heat to 90 °C for 65 sec, drain.

Wash:

- Add DMF peptide grade (7 mL), drain for 7 sec.

Coupling:

- Add AA solution (0.2 M in DMF, 2.5 mL), add DIC solution (0.5 M, in DMF, 1 mL), add Oxyma solution (1 M in DMF, 0.5 mL). Heat to 70°C (30 sec), heat to 90 °C (120 sec), drain.

3.3.2 Manual coupling

For manual coupling DIPEA and PyBoP were chosen as activator base and activator, respectively. For a 0.1 mmol scale, the AA (0.5 mmol) of interest was dissolved in 2.5 mL of DMF and added to the resin. PyBoP (1.15 mmol) was dissolved in 1 mL of DMF and applied to the resin as well. Further, DIPEA (0.5 mmol) was added, followed by an overnight incubation (RT, 400 rpm on standard shaker). Afterwards, the resin was washed five times with DMF. For Fmoc deprotection a 25 vol% piperidine solution in DMF (2 mL) was applied for 10 min (RT, 400 rpm on standard shaker). The washing and deprotection steps were repeated once.

3.3.3 Peptide deprotection and cleavage from resin

Swollen resins were transferred to peptide reactors (Carl Roth) and the DMF pushed out of the syringe. The resin was washed twice with DMF and DCM and air-dried for 15 min. Standard peptides were cleaved from resin by shaking in a solution of 95 vol% TFA, 2.5 vol% TIPS, 2.5 vol% MQ for 2 hours (RT, 400 rpm, standard shaker).

For BA containing peptides, the cleavage cocktail was supplemented with methylboronic acid (6 mol excess/ BA, 72 mg for 0.1 mmol scale) and the whole reaction mixture incubated overnight.

For microcleavage reactions, the resin was washed with DMF and DCM and then air-dried for 15 min. One drop of TFA was added and the reaction vessel shaken for 30 min (400 rpm, standard shaker). The reaction was then quenched with three drops of MQ and submitted for Maldi-TOF analysis.

The peptide-cleavage cocktail mixture was precipitated in 40 mL of icecold diethylether. The precipitate was isolated after centrifugation (4000 rpm, 15 min, 4 °C) by removal of the supernatant. Pellets were air-dried overnight at RT.

Synthesis Fluorescein-BAP

Boronic acid peptides were fluorescently labelled as similarly described in [61]. In brief, boronic acid containing peptides (0.52 µmol, 1 equivalent) were dissolved in 500 µL degassed phosphate buffer 200 mM pH 7.1. TCEP (26 µmol , 50 equiv.) was added and the reaction stirred for 2 h under nitrogen atmosphere. Fluorescein-maleimide (10.4 µmol mg, 20 equiv.) was dissolved as a 10 mg mL^{-1} solution in DMF and added dropwise to the solution. The reaction mixture stirred overnight, and the resulting crude product was purified by HPLC.

3.3.4 ABA-AEEAc-Fluorescein

Fmoc-AEEAc (29.19 µmol), DIPEA (116.7 µmol), PyBop (58.4 µmol) and ABA (14.6 µmol) were dissolved in 5 mL of DMF in a round bottom flask. The reaction mixture was stirred overnight and solvents were removed under HV. Then, Fmoc was cleaved off by addition of 292 µL of 20 vol% piperidine solution in 2 mL of DMF (10 min, RT, 800 rpm). Solvents were again removed under HV and the crude product solubilized in 9 mL (900 µL for dye without linker) of sodium bicarbonate. Afterwards, NHS-Fluorescein (14.6 µmol) was dissolved in 1 mL (100 µL for dye without linker) of DMF and dropwise added to the reaction mixture which stirred overnight at RT. The crude product was concentrated under HV and purified by HPLC.

3.3.5 BPA N-terminal protection

The N-terminal protection of BPA was performed as similarly described in [61]. In brief, BPA (4.78 mmol) was dissolved in 15 mL NaOH (1 M) in a round bottom flask (15 mL) and stirred at RT for 30 min. Fmoc-NHS (5.97 mmol) was dissolved in 14 mL THF and dropwise added to the solution which became clear and stirred overnight. THF was evaporated and the reaction mixture washed 4x with 40 mL of EA (pH > 10 adjusted with NaOH). The aqueous solution was then acidified in a becher with appropriate amount of 1 M HCl to pH 1. The precipitate was dissolved in 3x 30 mL EA and washed 2x with HCL acidified water. The combined organic layers were dried with magnesium sulfate and concentrated under vacuum which gave a white solid.

3.3.6 BPA side chain protection

The crude product was redissolved in 50 mL of dry THF/Toluol (1:1) mixture. Pinanediol (9.56 mm) was pre-dissolved in 5 mL of the same solvent mixture and then added to the crude solution which became clear upon addition. After one hour of incubation, the material was concentrated under vacuum, affording a yellow oil. Silica gel chromatography (PE/EA, 4:1 vol/vol with 1 % acetic acid yielded a yellow oil product (R_f value 0.3) which was co-evaporated with 3 x 40 mL of toluol to afford a white solid under HV.

3.4 Purification

3.4.1 HPLC

HPLC samples were first dissolved in 15 mL 0.1 vol% TFA, vortexed and sonicated. Up to 30 vol% ACN was added until complete dissolution. The solution was centrifuged (4000 rpm, 15 min, RT, Eppendorf centrifuge) and the supernatant filtered (cellulose filter: 0.2 µm). The filtrate was first purified with a standard 0.1 vol% TFA MQ/ACN ramp (Figure S 1) (flow rate 25 mL min^{-1}) on a Shimadzu C18 Phenomenex column (reverse phase). The methods were adjusted according to the respective product, matching its initial ACN concentration (i.e. method start at 10 vol% ACN if compound was dissolved in this condition). Fractions of interest were pooled and lyophilized (CHRIST Alpha 2-4 LSCbasic).

3.5 Binding studies

3.5.1 ESI-MS

ESI-MS spectra were recorded with an Advion ESI-MS spectrometer. If not stated otherwise, samples were dissolved at 100 µM in DMSO and diluted 1:99 vol/vol with ABC buffer (pH 7.4, 10.1 mM). The respective BA binder was dissolved at 2 mM in DMSO and serially diluted 1:1 vol/vol in DMSO. The respective BAs (-peptide) dissolved in DMSO were further diluted 1:99 vol/vol with ABC buffer (pH 7.4, 10.1 mM). The standard peptide and BA (-peptide) solutions were then combined 1:1 vol/vol and the reaction shook for 1 ½ h (400 rpm, RT, standard shaker). Afterwards, 50 µL of sample were injected for ESI-MS analysis.

3.5.2 ARS calibration:

ARS (3.57 mM) was dissolved in DMSO and serially diluted (1:1 vol/vol) in DMSO. The ARS containing DMSO solutions with decreasing concentrations were mixed 1:99 vol/vol with ABC buffer (pH 7.4, 10.1 mM). The BA binder (3.57 mM for 4CPBA and 0.179 mM for BA peptides) was dissolved in DMSO, serially diluted in DMSO (1:1 vol/vol) and then mixed 1:99 vol/vol (4CPBA) or 1:9 vol/vol (BA-peptide) with ABC buffer (pH 7.4, 10.1 mM (4CPBA), or 11.1 mM (BA-peptide). Pre-diluted ARS and BA binder samples were then mixed in a 1:1 vol/vol and mol/mol ratio (highest final concentration ARS: 17.85 µM, lowest final concentration ARS: 0.558 µM). The resulting solutions incubated for 15 min (400 rpm, RT, standard shaker). Fluorescence emission intensities were recorded with a Spark 20M microplate reader (Tecan®), with $\lambda_{excitation}$ = 495 nm and $\lambda_{emission}$ = 556 nm. 17.85 µM ARS in ABC buffer (pH 7.4, 10 mM) and 10 vol% DMSO served as a blank. Samples were measured as quadruplicates in a fluorescence microplate (384 Well Plate, PS, Small Volume, LoBase, Greiner Bio-One) using 25 µL of reaction volume.

3.5.3 ARS displacement assay

After the optimal ARS concentration has been determined by an ARS calibration dilution, this concentration was chosen for displacement studies. For this, the ARS DMSO stock solution was 300x concentrated (i.e. 6.6 mM) to the final ARS concentration (22 µM). The ARS stock solution was then diluted 1:99 vol/vol with ABC buffer (pH 7.4, 10.1 mM). The BA binder was dissolved in DMSO (6.6 mM for 4CPBA

or 0.33 mM BA-peptide) and further diluted 1:99 or 1:9 with ABC buffer (pH 7.4, 10.1 mM (4CPBA), or 11.1 mM (BA-peptide). The resulting solutions were combined 1:1 vol/vol and mol/mol and shook for ½ h (400 rpm, RT, standard shaker). The serine containing peptides (82.5 mM) were dissolved in DMSO and serially diluted (down to 2.57 mM) in a 1:1 vol/vol ratio with DMSO. Afterwards, the serine containing peptides were diluted with ABC buffer (pH 7.4, 11.1 mM) 1:9 vol/vol. Fructose (660 mM) served as a positive control, was dissolved in DMSO and serially diluted as described for the serine containing peptides.

The dilutions were then supplemented with 1:2 vol/vol BA-ARS mix (highest final concentration: 4CPBA 22 µM, ARS 22 µM, serine peptide 2.75 mM) and shook for 1 ½ hours (400 rpm, RT, standard shaker), before fluorescence emission was detected as described previously. The blank consisted of the final ARS concentration with 10 vol% DMSO in ABC buffer (pH 7.4, 10 mM). As fluorescence signal reference, DMSO was used instead of serine peptides solubilized in DMSO. The gain was automatically optimized for every concentration by the microplate reader and the intensity compared to the reference.

3.5.4 MST calibration

MST dyes were dissolved in DMSO (0.31 mM). The material was then serially diluted in DMSO (1:1 vol/vol) (down to 0.076 µM) and then mixed 1:19 vol/vol with ABC buffer (pH 7.4, 10.53 mM). The material was quickly mixed, centrifuged (standard table centrifuge) and analysed with the microscale thermophoresis device (Monolith NT.115 of NanoTemper Technologies GmbH). Measurement settings: 20 % LED laser power, blue excitation. Fluorescence counts were held constant between 500 and 2000.

3.5.5 MST assay

The MST dye of interest was dissolved in DMSO in accordance with the MST calibration and diluted 1:9 vol/vol with ABC buffer (pH 7.4, 11.1 mM) as described previously. The peptides (78.31 mM) were dissolved and serially diluted (1:1 vol/vol) in DMSO to a concentration of 4.77 µM. The peptides were then further diluted in ABC buffer (pH 7.4, 11.1 mM) 1:9 vol/vol. For fructose as positive control, however, a higher concentration (4.66 M) in DMSO was chosen and serially diluted 1:4 vol/vol. The other steps were held constant between peptides of interest and fructose. The resulting solutions were combined with the diluted MST dye (1:1 vol/vol) (highest and final

concentration peptides: 3.92 mM, highest and final concentration fructose: 233 mM). The solutions were quickly shaken and centrifuged (standard table centrifuge) before being measured by the MST device. Measurements were conducted at 20 % LED laser power (blue excitation), 20 % and 40 % MST power, respectively at 23 °C. Before every MST measurement, the capillary scan was carried out.

3.5.6 Fibril affinity assay

Peptides (64 mM) were dissolved in DMSO and serially diluted 1:1 vol/vol in DMSO to a concentration of 470 µM. A control concentration with only DMSO was prepared as well. The respective peptide solutions (5 µL) were further diluted 1:9 vol/vol with ABC buffer (pH 7.4, 11.1 mM) (45 µL) and incubated for 12 h (37 °C, 400 rpm, thermoshaker). After quick centrifugation (standard table centrifuge), 50 µL of Fluorescein-AEEAc-ABA (50 µM in 10 vol% DMSO in ABC buffer (pH 7.4, 11.1 mM) was added 1:1 vol/vol to the diluted peptides (highest peptide concentration: 3.2 mM). The solutions were quickly mixed and transferred to a white transparent absorbance greiner plate (384-well standard polystyrene microplate, non-sterile, colour plate/bottom: clear, Greiner-Bio-One) (30 µL measurement volume, in triplicates). ABC buffer (10 vol% DMSO, pH 7.4, 10 mM) served as a blank and was used for subtraction. The turbidity assay at 500 nm and 600 nm wavelength was conducted with a Spark 20M microplate reader (Tecan®). Next, the plate was sealed with parafilm and shaken for 2 h on an orbital shaker and the same assay was repeated. Afterwards, the triplicate solutions were pooled again in one Eppendorf tube for each concentration and 85 µL of solution was transferred to a new Eppendorf tube which was centrifuged for 1 h (14.8 k rpm, RT, high-speed table centrifuge). Supernatants (1) of concentrations of interest were analysed with fluorescence microscopy using an a YFP filter ($\lambda_{excitation}$ = 500 nm, $\lambda_{emission}$ = 535 nm) and then transferred to a fluorescence microplate (25 µL measurement volume, in triplicates). Fluorescence measurements were carried out at $\lambda_{excitation}$ = 495 nm, $\lambda_{emission}$ = 556 nm and the fluorescence gain optimized automatically by the microplate device (blank (1): 10 vol% DMSO ABC buffer pH 7.4 10 mM). Supernatants (1) of interest were collected for TEM imaging. For dye release studies the pellets (1) were mixed properly and 5 µL of each concentration was transferred to a new Eppendorf tube and diluted (75 µL) with 0.01 vol% TFA MQ (adjusted the solution to pH 4). The remaining pellet (1) was used for TEM imaging. The diluted pellet (2) was incubated for 30 min (400 rpm, RT, standard shaker) and

then centrifuged for one hour (14.8k rpm, RT, high-speed table centrifuge). Supernatants (2) were transferred to a fluorescence microplate (25 µL measurement volume, in triplicates) and fluorescence intensity was measured as described before (blank (2): 5 µL blank (1) + 75 µL of 0.01 vol% TFA). Supernatants (2) of interests were analysed with fluorescence microscopy as outlined previously and collected for TEM imaging. Further, the pellets (2) were diluted in 20 µL of MQ water and fluorescence intensities were recorded (n=1) and later collected for TEM imaging (blank (3): 5 µL blank (2) + 20 µL MQ).

3.6 Hydrogel preparation and vial inversion test

The depsipeptide CKIKISQINM (309.23 nmol) and diboronic acid cross-linker (154.62 nmol) or PEG_{1000}-diamine (236.8 nmol) were mixed in 0.1 vol% TFA MQ solution to a final volume of 200 µL. The samples were shaken (1/2 h, 400 rpm) and the pH neutralized with PB pH 9 300 mM. For positive control samples, 1.65 mM of CKIKISQINM was prepared in the same way.

3.7 Computational chemistry

3.7.1 Energy minimizations

Structures of interest were drawn in ChemDraw and imported in Chem3D as sdf data files. Structures were minimized using the MM2 (RMS Gradient 0.0100, 10000 iterations) or MMFF94 function. As a comparison, structures were drawn from scratch in Avogadro and minimized using UFF (9999 iterations, deepest descent, 10^{-7} convergence).

3.7.2 DFT calculations

DFT calculations of BA-tripeptide complexes were carried out with the B3LYP hybrid functional [91] and the aug-cc-pVDZ basis set [92] for all atoms using ORCA software. Geometric optimizations were performed with a convergence criterion of 10^{-9} a.u. for the density and 10^{-6} for the gradient. A polarizable continuum model was utilized to simulate the effect of water in the geometry optimization. All structures were confirmed as minima of the potential energy surfaces using the same level of theory.

3.8 Softwares

OriginPro 2021b (64-bit) (version: 9.8.5.201) was used for data visualization. NMR data evaluation was conducted with Topspin (version: 4.1.4). Dissociation constants were computed with the nanotemper analysis software.
Chemical structures were drawn with ChemDraw (version 21.0.0). Energy minimizations were performed with Chem3D (version: 21.0.0), Avogadro (version: 1.1.1) and ORCA (version: 5.0.3.). Optimized structures were drawn with Mercury (version: 3.8).

3.9 Statistics

Standard deviations were calculated using error propagation for blank subtraction and relative intensities:

$$Subtraction: \bar{z} = \bar{x} - \bar{y}$$

$$\sigma_z = \sqrt{(\sigma_x)^2 + (\sigma_y)^2}$$

$$Division: \bar{z} = \frac{\bar{x}}{\bar{y}}$$

$$\sigma_z = \bar{z} * \sqrt{(\frac{\sigma_x}{\bar{x}})^2 + (\frac{\sigma_y}{\bar{y}})^2}$$

With $\bar{z}$, $\bar{x}$, $\bar{y}$ being averages and σ being standard deviations.

$$\mathrm{f_c} = \mathrm{b} + \frac{\mathrm{b} - \mathrm{u}}{2} * (FluoConc + c + K_d - \sqrt{((\mathrm{FluoConc} + \mathrm{c} + K_d)^2 - 4 * \mathrm{FluoConc} * \mathrm{c}}$$

With $\mathrm{f_c}$ fraction bound, b being the fluorescence signal of the bound, and u of the unbound state, FluoCon being the concentration of the fluorophore and c the concentration of the ligand.

4 Results and Discussion

4.1 Diserine motifs

4.1.1 SAPF selection and synthesis

In this study, the SAP sequence CKIKISQINM was selected as the core building block since it was shown to form high aspect ratio nanofibrils, to be biocompatible, to be applicable as hydrogel and to function as depsipeptide [36]. Further, the sequence exhibits a serine residue which can be exploited for BA reactions. However, since most techniques that determine binding affinities rely on molecularly dissolved compounds, SAPs fall out of this scope. Self-assembling peptide fragments (SAPF), SAP derivatives which omit the CKIKI part crucial for self-assembly, were first utilized to derive relevant interaction parameters for BAs. Since in the end these sequences should again be coupled to the CKIKI backbone to form nanostructures, SAPFs which are as similar as possible to CKIKISQINM were designed (Figure 13). They were synthesized by standard Fmoc-SPPS and successfully purified by HPLC as determined by LCMS (Figure S 10, Figure S 11).

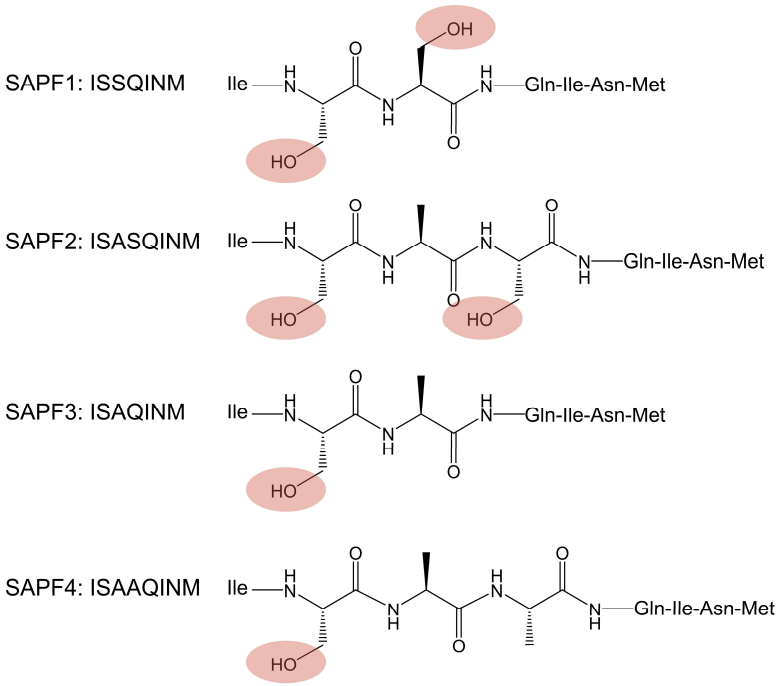

Figure 13: Self-assembling peptide fragment selection: Molecular structures of selected SAPFs are depicted. Potential BA binding sites are indicated in red. Primary AA sequences are described as one letter code, AA which are not directly involved in the BA reaction are abbreviated as three letter code.

Since BAs preferentially react with hydroxyl groups, SAPFs with different number, position and spacing of serine residues were designed. Previous publications have shown that two adjacent serine residues can potentially interact in a bidentate fashion with BA compounds [63]. Therefore, SAPF1 which exhibits two consecutive serine residues was chosen (Figure 13). In SAPF2, a spacer was inserted to assess BA binding of pre-oriented diols which face in the same direction. Alanine was chosen as a spacer residue since it is not sterically demanding, chemically inert and offers the backbone more rigidity than glycine which could impair self-assembly when coupled to CKIKI. In SAPF3 and SAPF4 serine was substituted by the structurally related alanine residue. These structures represent negative control peptides for SAPF1 and SAPF2, respectively.

4.1.2 Binding studies

4.1.2.1 ESI-MS

To get a qualitative impression of the BA-peptide reaction, mass spectrometry was carried out. First, Maldi-TOF measurements with varying amounts of BA binders were conducted. However, due to the harsh measurement conditions and or due to the acidic nature of the Maldi-TOF matrix, no signals which correspond to the BA-peptide complex were detected (data not shown). As an alternative approach, ESI-MS measurements were performed which limited the choice of applicable buffers. The binding strength between BA and diols or catechol is strongly dependent on pH and buffer conditions [59]. Phosphate buffers (PB) with concentrations exceeding 100 mM are commonly used to measure these reactions [61]. However, PB caused SAPF precipitation (data not shown). Another buffer system was required and established. The SAPFs were first pre-dissolved at a 100-fold or 10-fold concentration in DMSO and then diluted with to final ammoniumbicarbonate (ABC) buffer concentration of 10 mM (pH 7.4). The buffer conditions were suitable to buffer BAs in titration experiments. If not stated otherwise, this buffer condition was used for all subsequent experiments.

To test whether BAs can react with the SAPFs at all, ESI-MS titration experiments were performed. The potential binder 4-carboxyphenylboronic acid (4CPBA) was titrated against a constant amount of SAPFs (100 µM).

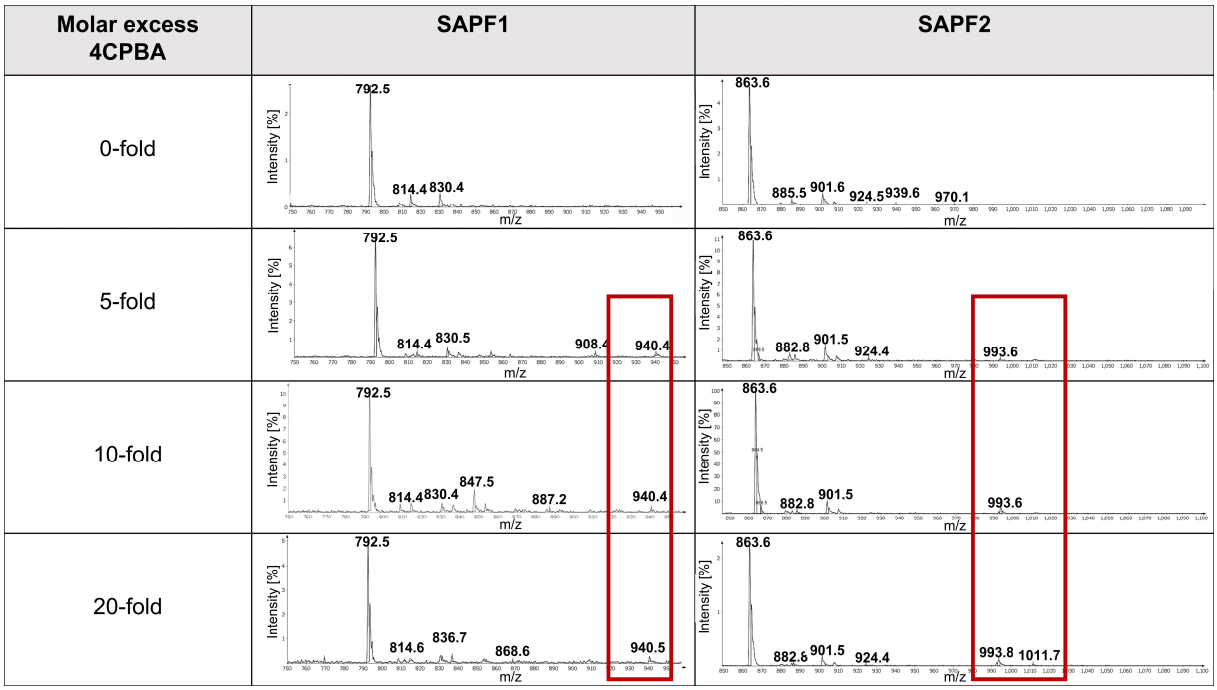

Figure 14: ESI-MS of SAPF1 and SAPF2 with varying amount of 4CPBA: Titration of 4CPBA against SAPF1 (left side) and SAPF2 (right side) yielded masses corresponding to monodentate binding for both peptides and bidentate binding signals only for SAPF2. SAPFs concentrations were 100 µM. Expected mass for SAPF1 monodentate: $[M+H]^+$ = 940.85 m/z, detected: $[M+H]^+$ = 940.4 m/z; for SAPF2 monodentate $[M+H]^+$ = 1011.93 m/z, detected: $[M+H]^+$ = 1011.7 m/z. Expected mass for SAPF1 bidentate: $[M+H]^+$ = 922.84 m/z, for SAPF2 bidentate: $[M+H]^+$ = 993.91 m/z, detected: $[M+H]^+$ = 993.6 m/z. Measurements were conducted in 1 vol% DMSO, ABC buffer 10 mM pH 7.4.

Titration of 4CPBA against SAPF1 yielded signals which corresponded to a reaction in which one hydroxyl group was involved in the formation of a boronic ester with 4CPBA (monodentate reaction) (Figure 14). Contrarily, SAPF2 showed stronger signals for the bidentate reaction independent of BA concentration. Similar observations were reported for SAPF3 and SAPF4.

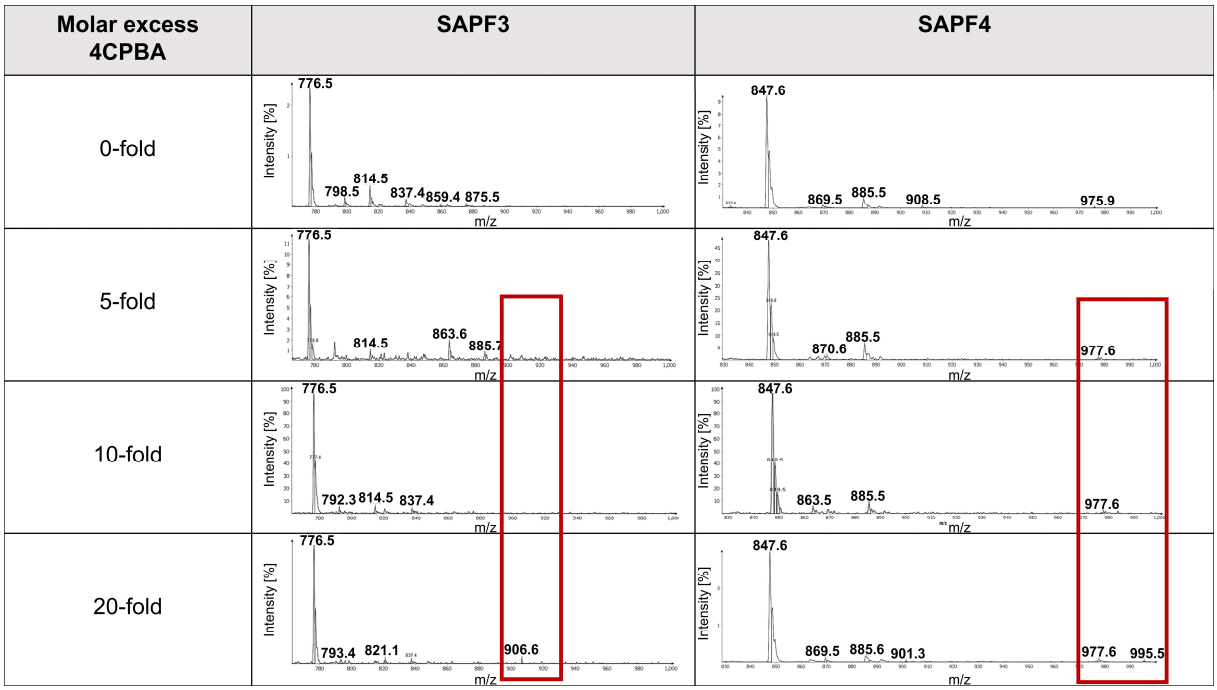

Figure 15: ESI-MS of SAPF3 and SAPF4 with varying amount of 4CPBA: Titration of 4CPBA against SAPF3 (left side) and SAPF4 (right side) yielded masses corresponding to monodentate reactions (SAPF4) and bidentate reaction signals (SAPF3 and SAPF4). SAPF concentrations were 100 µM. Expected mass for SAPF3 monodentate: $[M+H]^+$ = 922.88 m/z; for $[M+H]^+$ = SAPF4 monodentate $[M+H]^+$ = 995.93 m/z, detected: $[M+H]^+$ = 995.5 m/z. Expected mass for SAPF3 bidentate: $[M+H]^+$ = 906.8 m/z, detected: $[M+H]^+$ = 906.6 m/z, for SAPF4 bidentate: $[M+H]^+$ = 977.92 m/z, detected: $[M+H]^+$ = 977.6 m/z. Measurements were conducted in 1 vol% DMSO, ABC buffer 10 mM pH 7.4.

SAPF3 showed bidentate mass signals when combined with 20-fold excess 4CPBA (Figure 15). For SAPF4, in turn, bidentate mass signals were detected for all concentrations and only the highest excess of 4CPBA yielded monodentate binding signals.

The interpretation of the data is limited to the ESI-MS technique and the involved compounds. Due to the different propensity of molecules to be charged, to fly and complexes to fragment, ESI-MS can only provide qualitative information. This is reflected in the interaction peaks which barely change by the variation of 4CPBA (Figure 14, Figure 15). The signal to noise ratio is low and hence quantitative interpretation is not possible. The absence of binding for SAPF3 in lower concentrations is thus also not fully informative. Furthermore, the analysis of boronic acid compounds with mass spectrometry is tedious since dehydration in the gas phase can readily occur [62]. Due to the fact that the mass difference between monodentate and bidentate reactions equals Δ18 m/z, it is not possible to assess whether 4CPBA

reacted with one or two hydroxyl groups or lost water by dehydration effects. It could eventually explain the mass signals of SAPF3 and SAPF4 corresponding to a bidentate reaction even though they only exhibit one serine residue (Figure 15). Nevertheless, the data allows to conclude that all SAPFs reacted with 4CPBA in these conditions and that the binding occurred in a 1:1 stoichiometry (Figure 14, Figure 15).

4.1.2.2 ^{1}H NMR

To assess the role of the spacer of diserine peptides, semi-quantitative ^{1}H and DOSY-NMR experiments were performed next. Therefore, SAPF1 and SAPF2 were selected. ESI-MS has shown that reactions between SAPFs and BAs can occur. To ensure that this phenomenon is not only limited to one BA ligand, 4CPBA as potential diol binder was substituted by 4-Borono-L-phenylalanine (BPA) and ^{1}H NMR measurements were carried out.

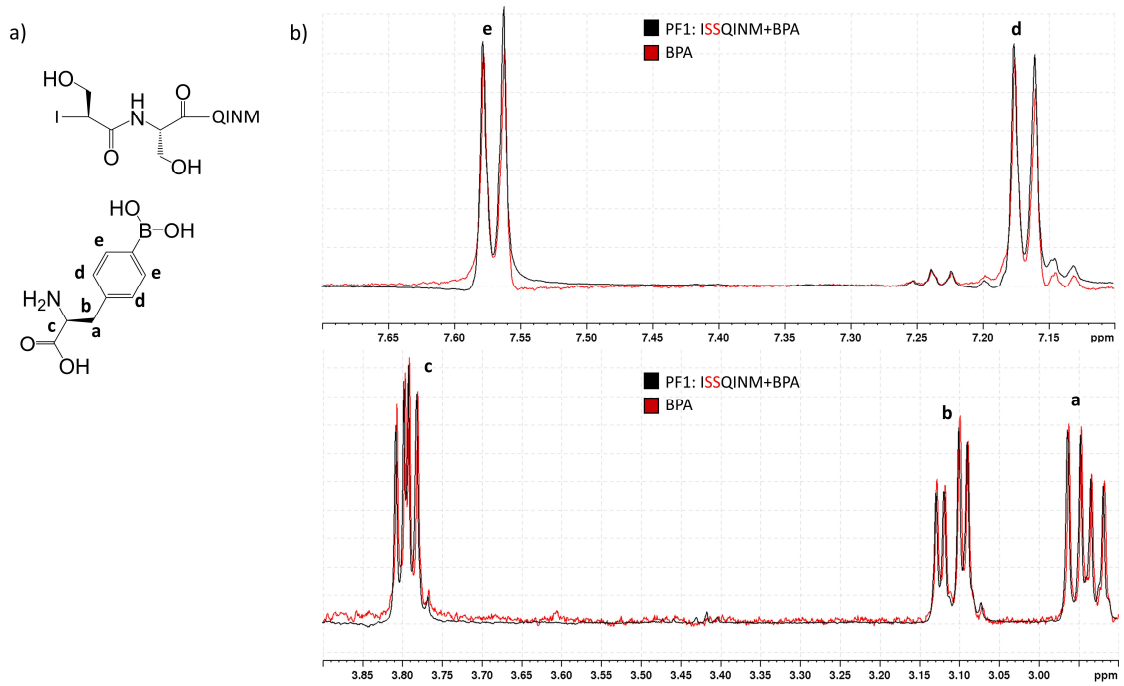

Figure 16: ^{1}H NMR of SAPF1 with PBA: (a) Molecular structure of SAPF1+BPA. H atoms corresponding to the depicted peaks are labelled accordingly. (b) Magnification of regions of interest are presented. No changes in chemical shifts are detected upon stoichiometric addition of BPA. Measurements were conducted in DMSO-d_6 : ABC buffer pH 7.4 10 mM 1:9 at 500 MHz using water suppression at 298 K. Spectra were calibrated to the DMSO-d_6 signal (δ = 2.50 ppm).

Since the peptide signals were poorly resolved as can be seen in (Figure S 21), the signals of BPA signals were used as a reference. The ^{1}H NMR spectrum of BPA did not show any changes in chemical shifts upon the addition of SAPF1 (Figure 16**Fehler! Verweisquelle konnte nicht gefunden werden.**). The signal overlap indicates that no relevant binding took place. In contrast, changes in chemical shifts were reported for SAPF2.

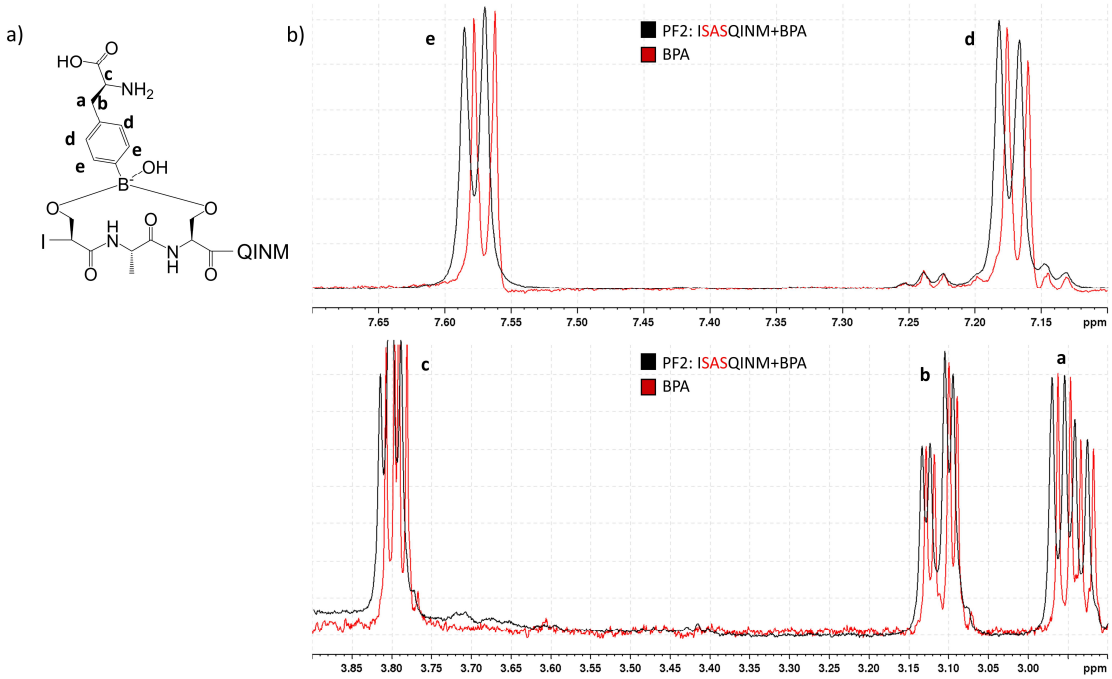

Figure 17: ^{1}H NMR of SAPF2 with PBA: (a) Molecular structure of SAPF2+BPA and one possible mode of interaction. H atoms corresponding to the depicted peaks are labelled accordingly. (b) Magnification of regions of interest are presented. Peak shifts are labelled. Measurements were conducted in DMSO-d_6: ABC buffer pH 7.4 10 mM 1:9 at 500 MHz using water suppression at 298 K. Spectra were calibrated to the DMSO-d_6 signal (δ = 2.50 ppm).

The changes in chemical shifts were observed for all regions of interest (Figure 17). The fact that they were from different magnitude indicates true interaction between SAPF2 and BPA. In principle, ^{11}B NMR would also provide insights for relevant interactions with the boron atom. However, most probably due to the applied measurement settings, the signals did not allow to deduce whether an interaction took place or not (data not shown). DOSY-NMR was carried out next to investigate the effect of binding on the diffusion coefficient.

4.1.2.3 DOSY-NMR

In accordance with the ^{1}H NMR results, a stronger decrease in diffusion coefficient was detected for SAPF2-BPA samples.

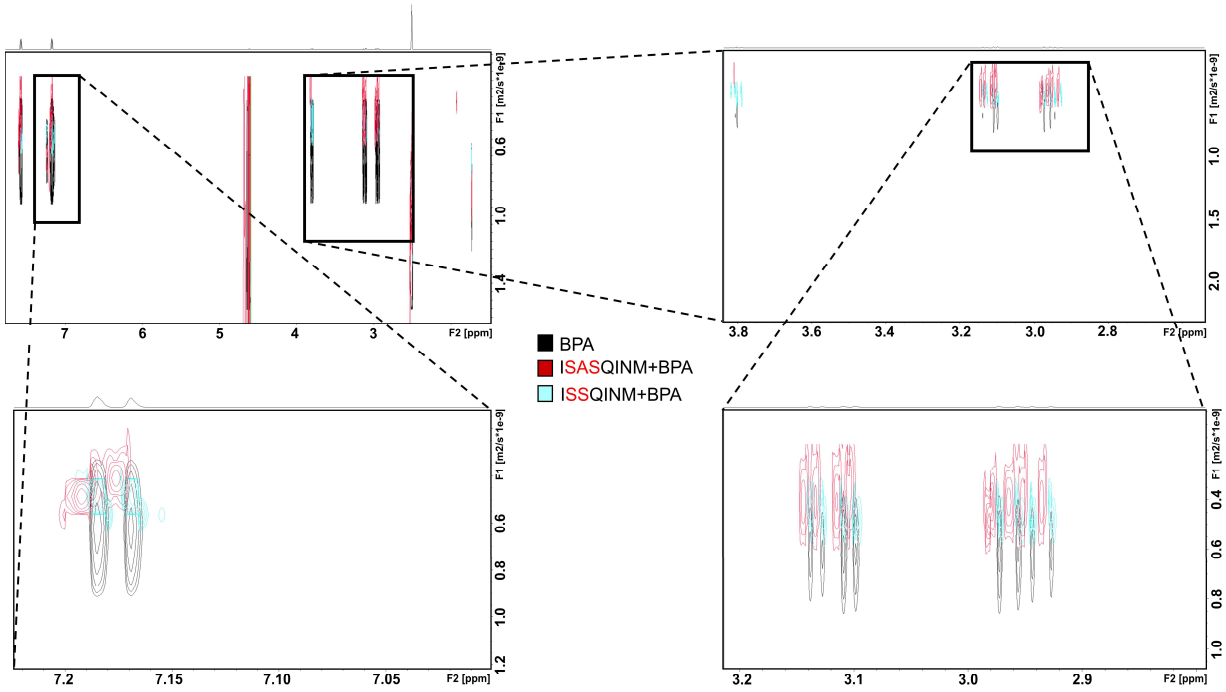

Figure 18: DOSY-NMR of SAPF1/SAPF2-BPA complexes: Signals of interest are extracted from the whole spectrum and magnified accordingly. A change in diffusion coefficient and chemical shift is observed for SAPF2-BPA complexes whereas overlapping signals are detected for SAPF1-BPA and BPA only. Diffusion coefficients are given in m^2/s on a linear scale. Measurement conditions are DMSO-d_6: ABC buffer pH 7.4 10 mM 1:9 at 500 MHz using water suppression at 298 K. Spectra were calibrated to the DMSO-d_6 signal (δ = 2.50 ppm).

Not only were the chemical shifts for SAPF2-BPA complexes different from BPA alone, but also species with lower diffusion coefficients were reported (Figure 18). Contrarily, SAPF1-BPA complexes showed almost completely overlapping signals with BPA alone suggesting SAPF2 to be more prone to react with BPA in these conditions. Even though the decrease in diffusion coefficient was minor for SAPF2 samples, it was still relevant as the involved molecules were low in molecular weight.

Taken together, ^{1}H NMR measurements are in line with DOSY-NMR results. A spacer between two consecutive serine residues was favourable and required to facilitate reactions with BAs. In contrast to ESI-MS, NMR analysis did not show any relevant binding of SAPF1 to BA (Figure 14, Figure 16). This can be attributed to the 1:1 molar ratio utilized in NMR experiments as compared to 5-fold BA excess in ESI-MS. However, this circumstance did not impair the reaction of SAPF2 with BPA and

therefore further underlines the hypothesis of SAPF2 being the more potent reaction partner.

4.1.2.4 DFT calculations

To approach the role of the spacer in diserine peptides computationally, a minimal model which is computationally cheap and feasible in the scope of this master thesis, was chosen. Four tripeptide sequences were designed.

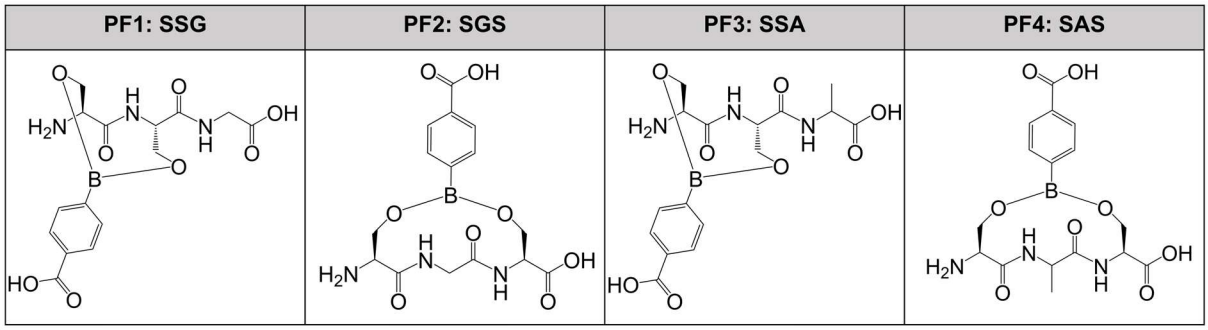

Figure 19: Peptide fragment-4CPBA complexes: Molecular structures of peptide fragments used for DFT calculations. 4CPBA represented the proof of principle BA binder.

The selected peptide fragments (PF) possessed two consecutive serine residues (PF1, PF3) or diserine separated by spacers either being glycine (PF2) or alanine (PF3) (Figure 19). Glycine was selected as a comparison to investigate the impact of backbone flexibility. To keep the total number of residues constant and the systems comparable, the respective AA which served as a spacer was attached on the C-terminus affording SSG and SSA (Figure 19). The energy minimization was first conducted individually for both interaction partners using DFT calculations. Next, 4CPBA was attached in a bidentate manner as depicted in (Figure 19) and resubmitted for energy minimization. After solving imaginary frequencies, optimized structures were obtained (Figure 20).

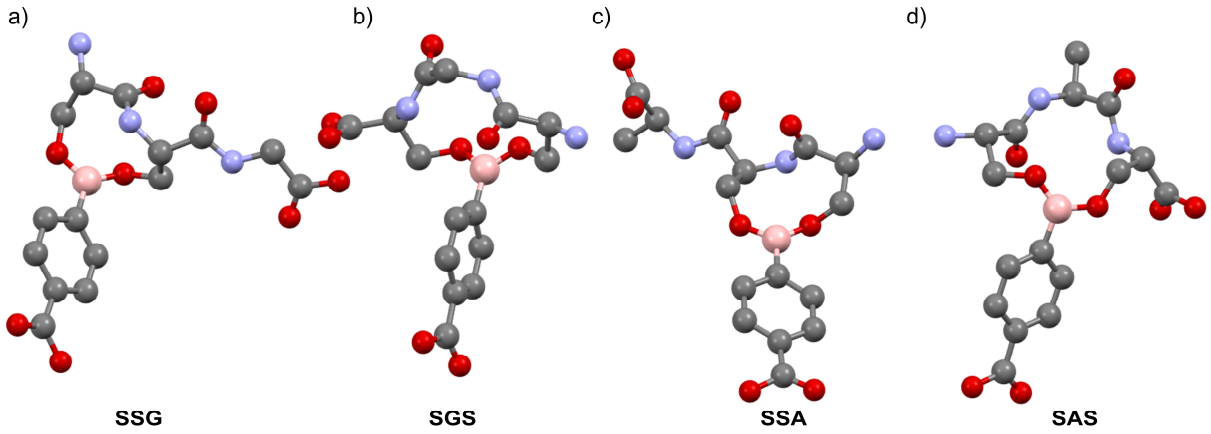

Figure 20: Tripeptide-4CPBA optimized structures: Model of the DFT optimized structures of (a) PF1, (b) PF2, (c) PF4 and (d) PF5. Hydrogen atoms were intentionally omitted for better visualization. Calculations were carried out using the B3LYP hybrid functional and aug-cc-pVDZ basis set. The PCM model was chosen to simulate water effects on geometric optimization. XYZ data is summarized in Table S 2, Table S 3, Table S 4, Table S 5.

The optimized structures exhibited different levels of Gibbs free energy.

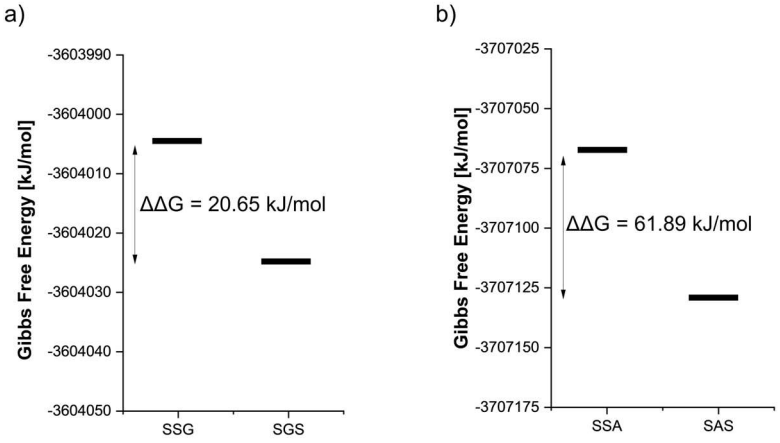

Figure 21: Total Gibs free energy of optimized tripeptide-4CPBA complexes: Energy differences for PF1 to PF4 are depicted. Systems with spacer show lower energies than consecutive serine residues. Calculations were carried out using the B3LYP hybrid functional and the aug-cc-pVDZ basis set. The PCM model was chosen to simulate water effects on geometric optimization.

The tripeptide-BA complexes with spacers showed lower energies than tripeptides with consecutive serine residues (Figure 21). This was consistent independent of the type of spacer. Interestingly, PF4 and PF5 optimized structures showed lower Gibbs free energies as compared to PF3 and PF5. It can be hypothesized that the entropic penalty

of the glycine spacer when confined by 4CPBA leads to an increase in total energy. However, experimental data which support this assumption are required.

Furthermore, it needs to be considered that the DFT calculations neglected buffer contributions and the direct interactions of water molecules with the boron atom. The conformational change of the boron atom from trigonal planar to tetrahedral is consequently not taken into consideration. Nevertheless, the obtained results were in accordance with the experimental data. It further underlines the hypothesis that bidentate reactions and thus higher binding affinities can probably be achieved by inserting an alanine spacer between consecutive serine residues.

4.1.2.5 ARS displacement SAPFs

To determine quantitative interaction parameters between BA and SAPFs, an alizarin red s (ARS) displacement assay was performed. ARS reacts with BA of specific geometry and thereby increases fluorescence emission. This can be utilized to derive BA-diol and BA-catechol binding constants [59]. However, before doing so, a suitable concentration of ARS-BA complexes needed to be determined. For this, different concentrations of ARS and 4CPBA (1:1 molar ratios) were screened and their fluorescence emission measured. The ARS concentration was chosen such that the

emission was significantly higher than empty wells after blank subtraction (Figure S 23).

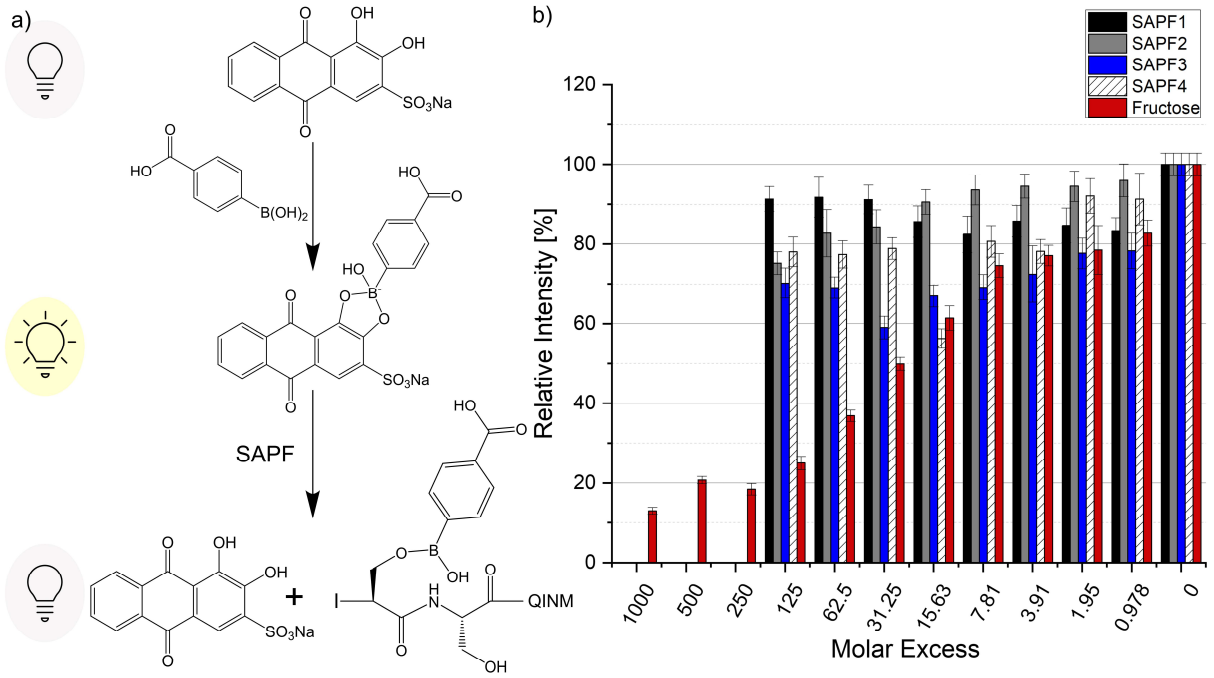

Figure 22: ARS displacement assay of SAPFs: (a) Molecular structures of ARS and the binding partners. The lightbulb indicates fluorescence emission at $\lambda_{emission}$ = 556 nm upon excitation at $\lambda_{excitation}$ = 495 nm. (b) Relative fluorescence intensities of ARS after the addition of SAPFs or fructose were referenced against pure ARS-4CPBA samples. Molar excess refers to the final ARS concentration of 22 µM. Due to the limit of solubility, data points for 250-1000-fold molar excess of SAPFs are missing. Measurements were conducted in 1:9 vol/vol DMSO ABC buffer pH 7.4 10 mM. Error bars are standard deviations calculated by error propagation.

For the displacement studies, ARS and 4CPBA were first preincubated (molar ratio 1:1) and the BA then displaced by titrating SAPFs against the ARS-4CPBA complex (Figure 22 a). Fructose thereby represented the positive control. By displacing the BA from the ARS pocket, a decrease in fluorescence emission was expected. Fructose could compete with ARS as BA reaction partner, leading to a 7-fold decrease in fluorescence upon addition of 1000-fold excess which was also reported in literature [59].

For the SAPFs, however, the decrease in fluorescence emission was not as drastic as for fructose. The investigated concentration window which was determined by peptide solubility showed a fluorescence decrease of 1.7-fold maximum. For SAPF1, the

relative fluorescence was almost constant throughout the whole concentration window (Figure 22 b) and showed the highest signals at the highest peptide concentration. For the peptide exhibiting an alanine spacer, SAPF2, in contrast a constant decrease in relative fluorescence intensity with increasing concentration was detected. Surprisingly, for SAP3 the highest binding affinity was detected as compared to the other SAPFs at almost every concentration. The peptide could compete with the positive control up to a molar excess of 31.25 µM (Figure 22). The signal dropped below 60 % and slightly increased again at higher concentrations. Like SAPF3, SAPF4 could compete with the fructose positive control up to a concentration of 15.63 molar excess and showed increase in fluorescence intensity by further concentration increase (Figure 22 b).

Consequently, the number of serine residues did not correlate with the decrease in relative fluorescence intensity. The absence of complete fluorescence depletion can be explained as follows. The affinity between serine residues of different number and 4CPBA is too low to effectively displace ARS from the ARS-4CPBA complex due to steric hindrance or the absence of bidentate binding. Another factor can be attributed to the ARS displacement assay itself. Using ARS and the BA binder in a 1:1 molar ratio is common in literature [61]. However, at this ratio, the ARS binding sites are not saturated as observed by titration experiments of BA against ARS (up to 200-fold, data not shown). Even though this fact is taken into consideration when computing apparent association constants, competing ARS molecules can impair the SAPF induced displacement of 4CPBA from ARS-4CPBA complexes. The increase in relative fluorescence intensity with increasing peptide concentration is probably caused by particle aggregation effects.

Taken together, ARS displacement assays come with certain constrains put upon the association strength and the geometry of the involved molecules. Therefore, microscale thermophoresis (MST) was conducted next to quantify the direct interaction between SAPFs and BAs.

4.1.2.6 MST SAPFs

4.1.2.7 Synthesis ABA-Fluorescein

For a proof of principle study and to learn the handling of the assay, fluorescein--NHS was conjugated to the free amine of 3-aminophenylboronic acid (ABA) (Figure 23).

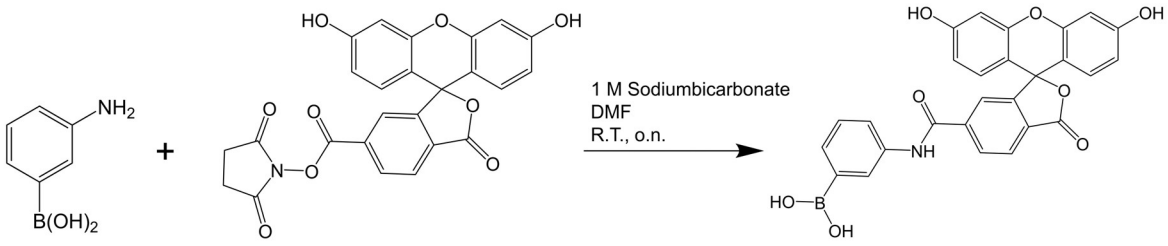

Figure 23: Synthesis of ABA-Fluorescein: The free amine of ABA reacts with the NHS moiety of Fluorescein-NHS.

The product was purified by reversed phase HPLC and successfully confirmed by LCMS (Figure S 16).

4.1.2.8 ABA-Fluorescein MST

To detect relevant thermophoresis changes, ABA-Fluorescein was titrated and the dye concentration yielding the fluorescence count recommended by the manufacturer was selected (data not shown). SAPFs were titrated against a constant amount of dye

leading to a change in fluorescence and temperature.

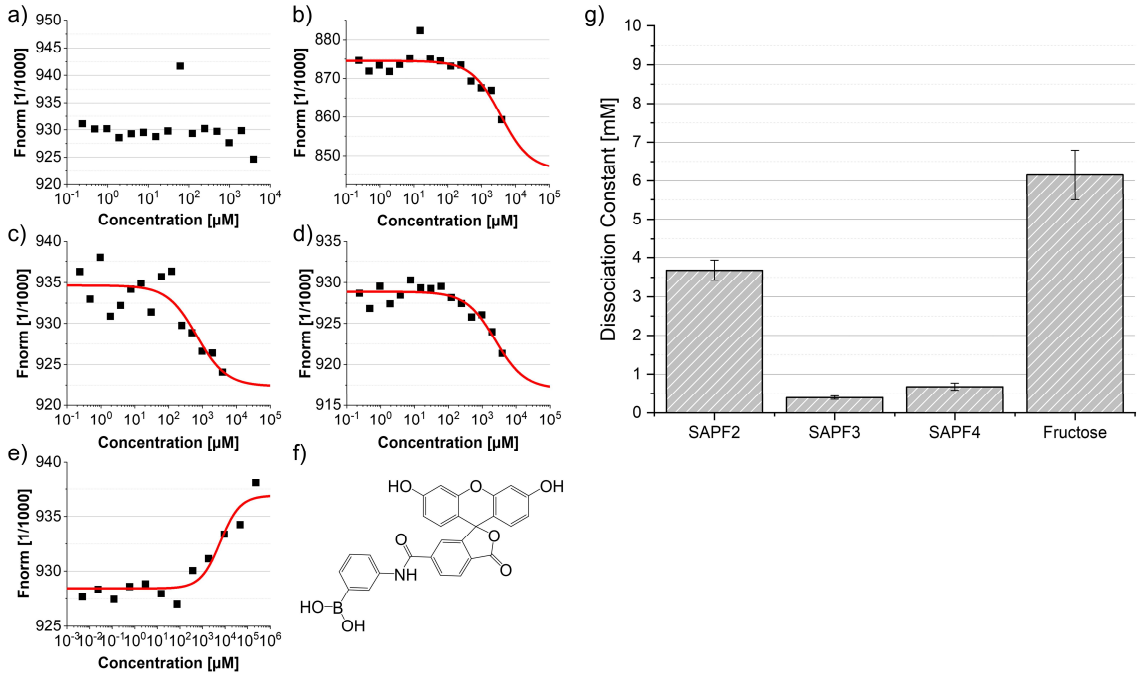

Figure 24: MST of SAPFs with ABA-Fluorescein: MST titration experiments of SAPFs using ABA-Fluorescein as a BA reaction partner. Changes in fluorescence intensities and temperatures are depicted for (a) SAPF1, (b) SAPF2, (c) SAPF3, (d) SAPF4 and (e) fructose. (f) Molecular structure of ABA-Fluorescein. (g) Dissociation constants of SAPFs and fructose as determined by the sigmoidal fits (red lines). Measurements were carried out in 1:9 vol/vol DMSO ABC buffer pH 7.4 10 mM. 0.12 µM was used as a dye concentration. Error bars are standard deviations obtained from the sigmoidal fit.

All SAPFs and fructose reacted in the applicable concentration range except for SAPF1 which did not show significant changes in fluorescence and temperature (Figure 24 a). Only concentrations which showed good solubility as can be seen in the fluorescence decay signals were plotted and taken into account for the determination of dissociation constants (K_d) (Figure S 25). The K_d values which were calculated by the sigmoidal fits showed results in the lower mM to higher µM regime. SAPF3 with a K_d of 0.394 ± 0.045 mM thereby exhibited the highest affinity, however strong data scattering was observed (Figure 24 c). In line with the ARS displacement assay, the diserine peptide SAPF2 performed worse with a K_d of 3.68 ± 0.252 mM. Surprisingly, fructose exhibited an even higher dissociation constant of K_d = 6.15±0.646 mM even though a K_d in the µM range was expected (Figure 24 e, g) [59]. To ensure that the reaction was not sterically hindered by fluorescein, a short PEG-linker was inserted. As an additional control, SQINM (SAPF5), the natural appendix of the CKIKISQINM

sequence was screened as well for later experiments. Since the material was already present from previous experiments, it was not required to be synthesized.

4.1.2.9 Synthesis ABA-AEEAc-Fluorecein

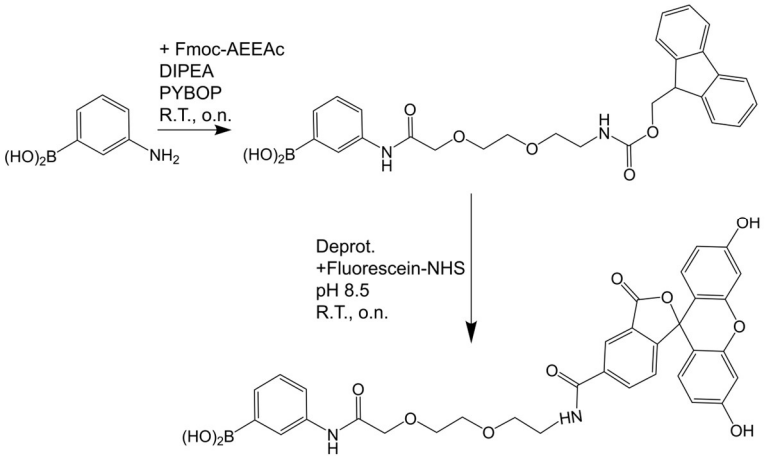

Figure 25: Synthesis route ABA-AEEAc-Fluorescein: ABA was first coupled to Fmoc-AEEAc via a condensation reaction and then Fmoc deprotected by means of piperidine. The free amine was then utilized to conjugate fluorescein.

The free amine of ABA and the carboxyl group of AEEAc first reacted via condensation. After Fmoc removal, Fluorescein-NHS was coupled to the free amine affording ABA-AEEAc-Fluorescein (Figure 25). Purification was successfully performed by reversed phase HPLC as determined by LCMS (Figure S 16).

4.1.2.10 ABA-AEEAc-Fluorescein MST

The insertion of the PEG linker decreased dissociation constants remarkably for all SAPFs (except for SAPF4) and fructose (Figure 26 g).

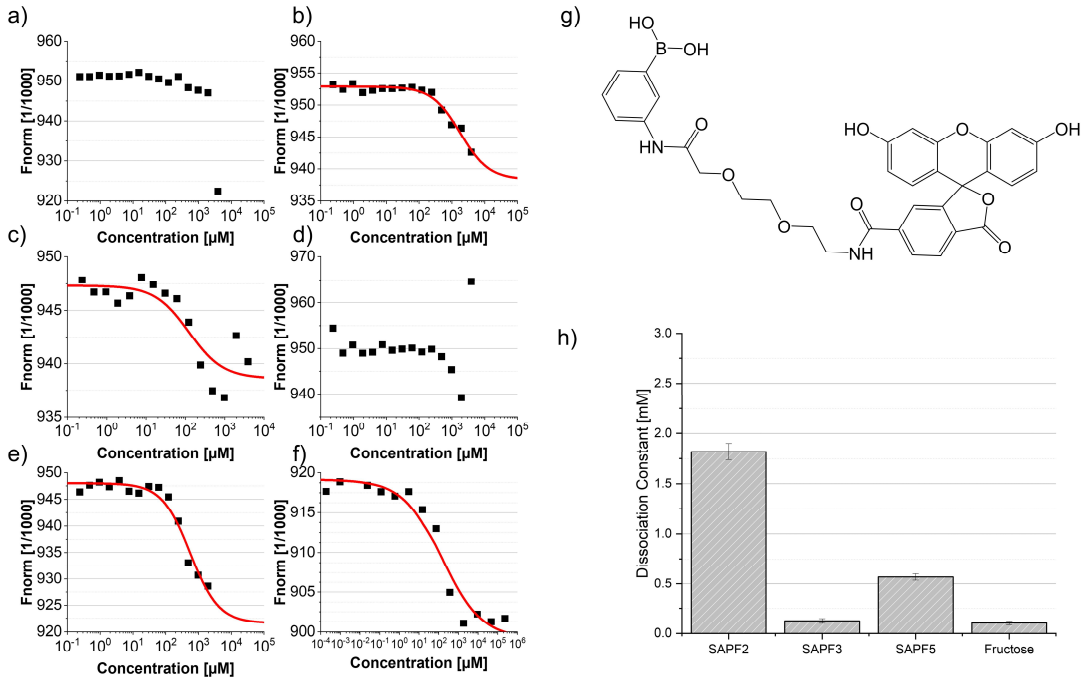

Figure 26: MST of SAPFs with ABA-AEEAc-Fluorescein: MST titration experiments of SAPFs using ABA-AEEAc-Fluorescein as a BA binder. Changes in fluorescence intensities and temperatures are depicted for (a) SAPF1, (b) SAPF2, (c) SAPF3, (d) SAPF4, (e) SAPF5 and (f) fructose. (g) Molecular structure of ABA-AEEAc-Fluorescein. (h) Dissociation constants of SAPFs and fructose as determined by the sigmoidal fit (red lines). Measurements were conducted in 1:9 vol/vol DMSO ABC buffer pH 7.4 10 mM. 0.072 µM was used as dye concentration. Error bars are standard deviations obtained from the sigmoidal fits.

For SAPF2 a 2-fold increase in binding affinity was achieved. For SAPF3 and fructose the difference was even 3.2-fold and 60-fold, respectively. The absence of binding for SAPF4 can be explained by particle aggregation as indicated by the fluorescence decay (Figure S 26). For SAP5 intermediate dissociation constants were reported (K_d = 0.568±0.0324 mM).

In line with the ARS displacement study, in MST, the diserine SAPFs showed lower binding affinities than monoserine peptides SAPF3 and SAPF4. The data suggests that the C-proximal glutamine and thus the chemical environment plays a role in stabilization of the BA-peptide complex. A certain space and orientation between the serine and glutamine residue is apparently required as SAPF3 showed higher affinities than SAPF4 and SAPF5. Even though the type of interaction was not fully resolved, SAPF3 and SAPF2 showing the highest affinities of mono-and diserine peptides, respectively, were selected for self-assembly studies which will be discussed later.

4.2 Tetraserine motifs

4.2.1 Tetraserine motif selection

Multivalency plays a crucial role for binding affinities of BAs and their reaction partners [61–63]. To investigate this effect for BA-diol interactions in peptides, tetraserine peptide motifs and corresponding diboronic acid peptide reaction partners were synthesized. Cooperative binding of the two reaction sites could eventually increase the overall binding affinity. Potential reaction partners were first determined by computational methods using three different force fields for energy minimization.

a)

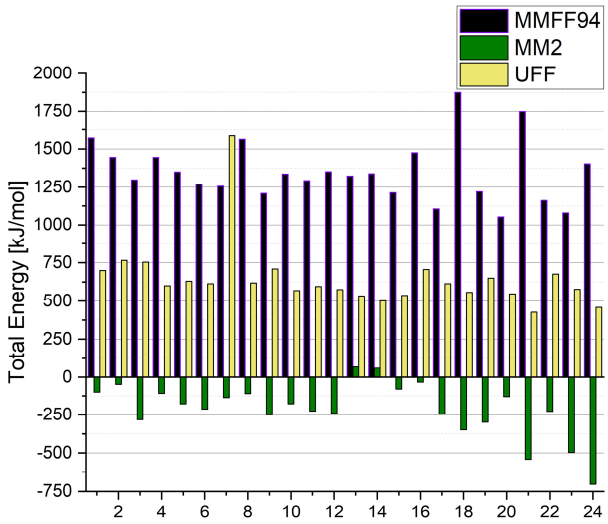

b)

Tetraserine peptide	Double BA peptide
TSP1: GSSGGSSK	BAP1: GG(BA)GP(BA)GK
TSP2: GSGGGSGGGSGGGSK	BAP2: GG(BA)GGG(BA)GK

Figure 27: Energy minimization of tetraserine-diboronic acid peptide complexes: (a) The force fields MMFF94, MM2 and UFF were utilized for energy minimization of potential reaction partners. Data points 23 and 24 represent the selected peptide sequences depicted in (b). AAs are abbreviated as one letter code, BPA as (BA). Complexes were drawn as bidentate binding partners.

A table of tested interaction partner is depicted in (Table S 1). Diboronic acid peptides were bound to various tetraserine motifs in a bidentate fashion and submitted for energy minimization. Since the force fields only rely on Newtonian physics, complexes from literature had also been taken into account to design new bisboronic acid tetraserine reaction partners [61,63]. Therefore, TSP1-BAP1 and TSP2-BAP2 were selected (Figure 27). The distance between reaction sites of TSP1-BAP1 is related to RhoBo and the tetraserine motif used in [63]. Since previous experiments have shown that an alanine spacer can significantly increase binding affinities, TSP3

(GSASGGSASGK) was later added to the tetraserine library. SAPF3 motif derivatives were not taken into consideration since its role as most promising binder was revealed after tetraserine peptide selection and purification.

The energy minimization has shown that spacers between the two boronic acids are required. Lysine spacers between boronic acids are commonly used to enhance solubility [61]. However, energy minimization revealed that lysine is sterically too demanding, therefore they were replaced by glycine. Besides, additional charges represent another variable which cannot be controlled in the system. Another observation was that the number of spacers is limited to a certain window. For TSP2, three glycine residues formed sterically low demanding loops to enable bidentate boronic acid binding. Furthermore, this sequence would allow several monodentate binding modes of the diboronic acid reaction partner. For post modification, an additional cysteine residue on the N-terminus was introduced to afford Cys-BAP1 and Cys-BAP2.

4.2.2 TSP and BAP synthesis

All tetraserine peptides were synthesized using standard Fmoc-SPPS and successfully purified by reversed phase HPLC (Figure S 12). For diboronic acid peptides, however, the unnatural AA first needed to be N-terminus and sidechain protected to be applicable in SPPS.

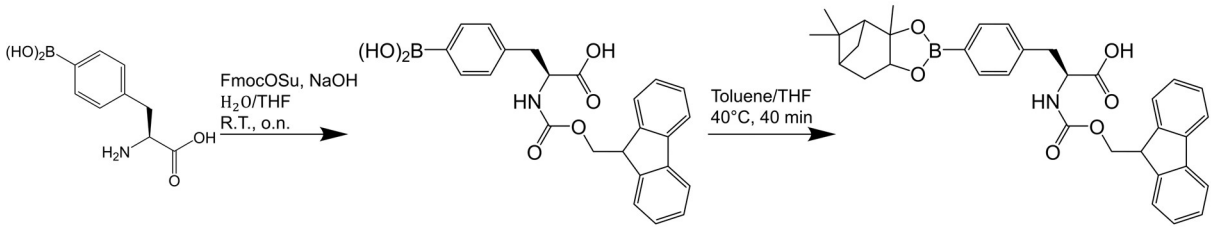

Figure 28: Synthesis route BPA protection: N-terminal and side chain protection procedure of BPA as described in [61].

The N-terminal Fmoc protection was followed by a pinanediol side chain protection of the BA (Figure 28). After column chromatography, however, a yellow oil instead of a white powder as described in literature was obtained [61]. Residual acetic acid was co-evaporated with toluol affording a white solid under HV (yield: 101.8%, literature

value 86%) [61]. The yield exceeding 100% can be explained by slight impurities and residual water (Figure 29). The successful coupling of protection groups was followed by ^{1}H NMR spectroscopy.

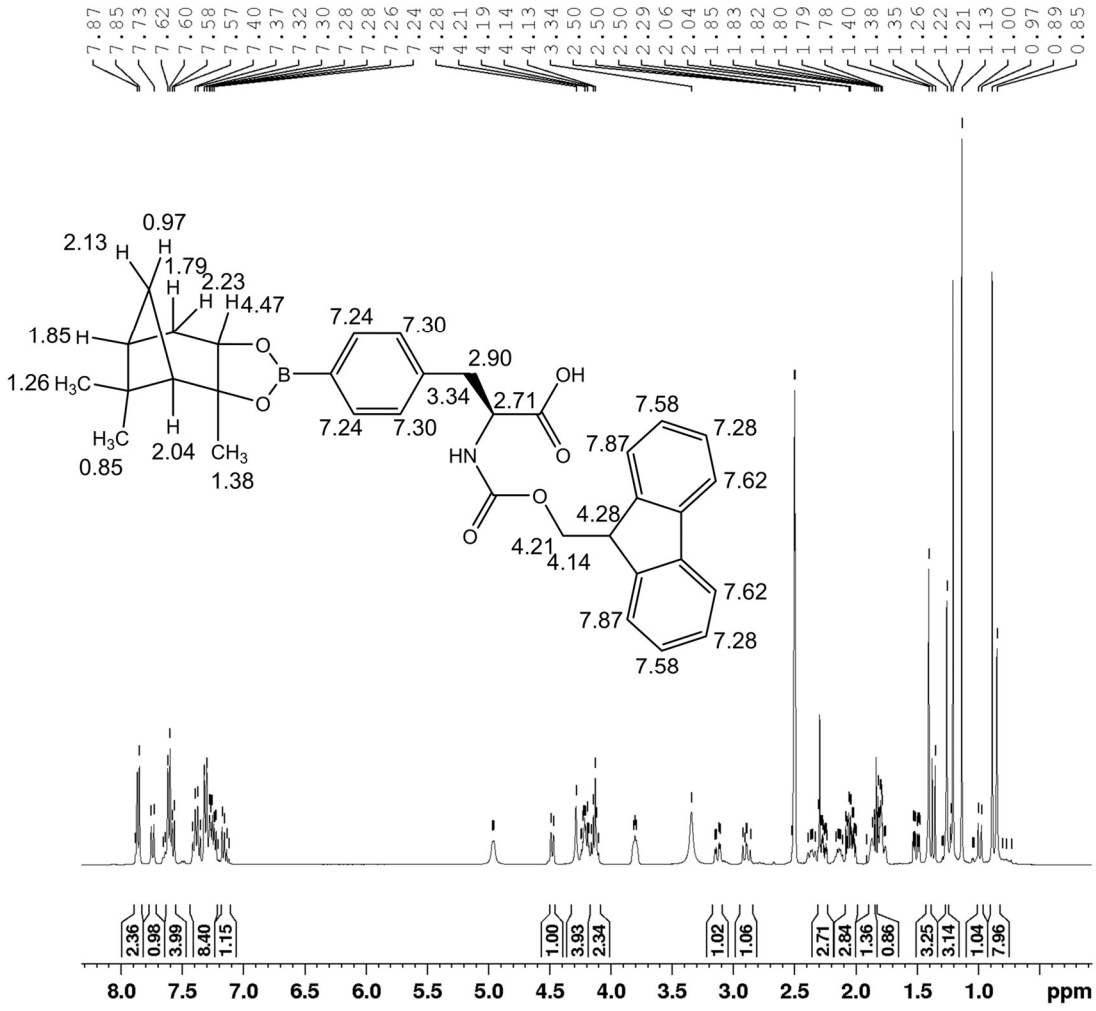

Figure 29: ^{1}H NMR of N-terminal and sidechain protected BPA. The spectrum was calibrated to the DMSO-d_6 signal (δ = 2.50 ppm). 298 K. 400 MHz.

Aromatic signals from the Fmoc and the strong signals from the methyl group of pinanediol indicated successful protection of BPA (Figure 29). The unnatural AA was then used in SPPS to afford BAP1 and BAP2. However, since the SPPS machinery was not functional, the last cysteine coupling step was carried out manually for BAP1. Unfortunately, as can be seen by LCMS analysis, the coupling was only partly successful and fully separation of Cys-BAP1 from BAP1 was not possible (Figure S 13, Figure S 14). However, pure fractions only consisting of BAP1 were collected for binding assays. The Cys-BAP1 BAP1 mixture could still be used for fluorescein-maleimide coupling.

4.2.3 Binding studies

4.2.3.1 ARS displacement study TSP and BAP

The ARS displacement assay was again performed to obtain a quantitative impression of the binding affinity between TSPs and BAPs. The calibration curve revealed stronger interactions between ARS and BAP1 as compared to 4CPBA alone (Figure S 24). However, since a plateau was observed, an ARS concentration of 45 µM was chosen. The ARS displacement assay was carried out with BAP1, TSP1 and TSP3. TSP2 served as negative, fructose as positive control.

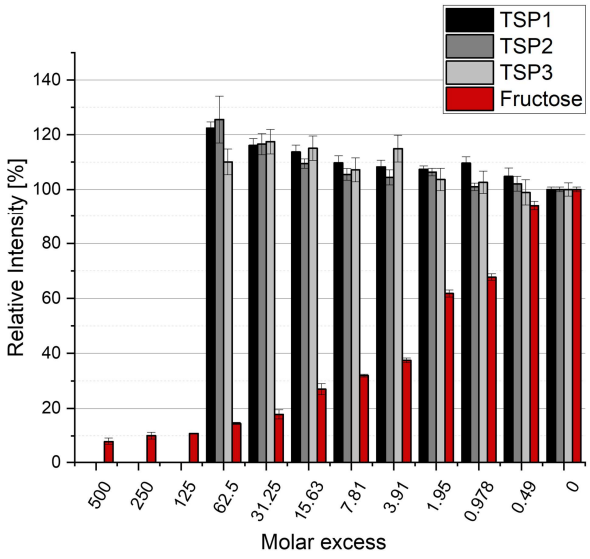

Figure 30: ARS displacement assay of TSPs with BAP1: Relative fluorescence intensities of ARS after the addition of SAPFs or fructose. Molar excess is referenced to the final ARS concentration of 45 µM which was double the concentration of BAP1. Due to the limit of solubility, data points for 125-500-fold molar excess of SAPFs are missing. Measurements were conducted in 1:9 vol/vol DMSO ABC buffer pH 7.4 10 mM using $\lambda_{excitation}$ = 495 nm, $\lambda_{emission}$ = 556 nm. Error bars are standard deviations calculated by error propagation.

None of the TSPs were able to displace BAP1 in the investigated concentration window. The only detectable decrease in relative fluorescence intensity was reported for fructose which showed an approximately 12.5-fold decrease at the highest concentration (Figure 30). As reported for the SAPFs at high concentrations, the relative fluorescence intensities even tend to increase most probably due to particle aggregation (Figure 22, Figure 30).

It is not possible to directly compare the binding affinities of fructose of the two ARS displacement experiments since the affinity of the 4CPBA-ARS and BAP1-ARS

complex might be different and therefore the number of free ARS molecules might differ. The absence of binding of TSPs to BAP1 is probably attributed to the steric hindrance caused by the peptide backbone of BAP1. 4CPBA-ARS complexes can presumably be better accessed than ARS-BAP1 complexes and therefore enable displacement by SAPFs. Since the displacement study was not applicable to diboronic-tetraserine systems, the assay was not conducted for BAP2 and MST was chosen instead to detect direct interactions. For this purpose, Cys-BAP1 and Cys-BAP2 were fluorescently labelled.

4.2.3.2 MST Tetraserine-diboronic acid peptides

4.2.3.3 Synthesis Fluorescein-diboronic acid peptide

To conduct MST measurements, fluorescein dyes were attached to cysteine containing diboronic acid peptides Cys-BAP1 and Cys-BAP2. As mentioned previously, Cys-BAP1 represents a peptide mixture of peptide with and without N-terminal cysteine. Nevertheless, BAP1 was coupled to fluorescein-maleimide via Michael type addition and successfully purified by reversed phase HPLC (Figure S 17).

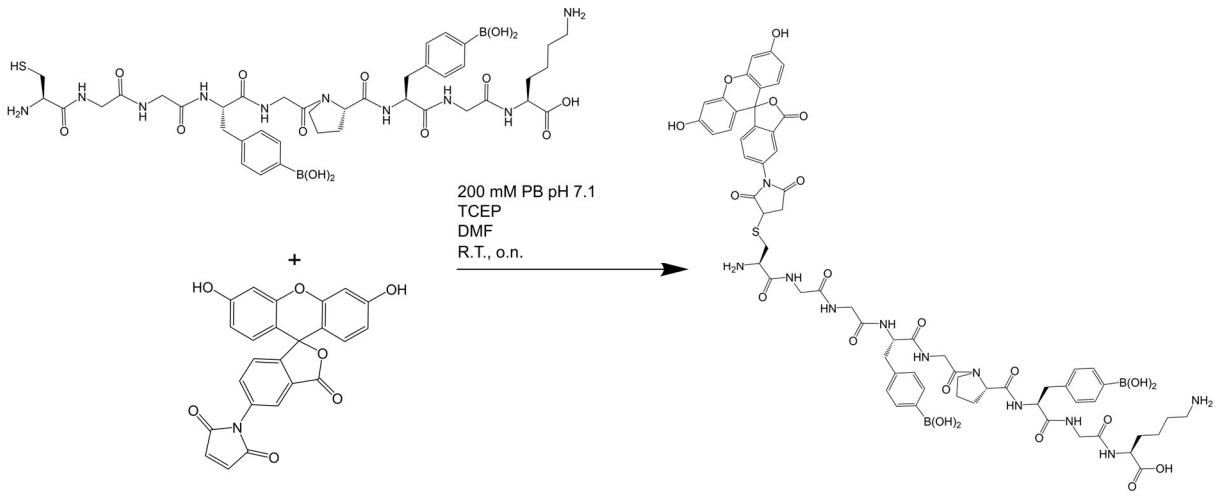

Figure 31: Synthesis route of BAP1-Fluorescein: Cysteine-BAP1 is attached to Fluorescein-Maleimide via Michael-type addition.

The same procedure was applied for BAP2 and a peptide-dye conjugate with sufficient purity was achieved (Figure S 18).

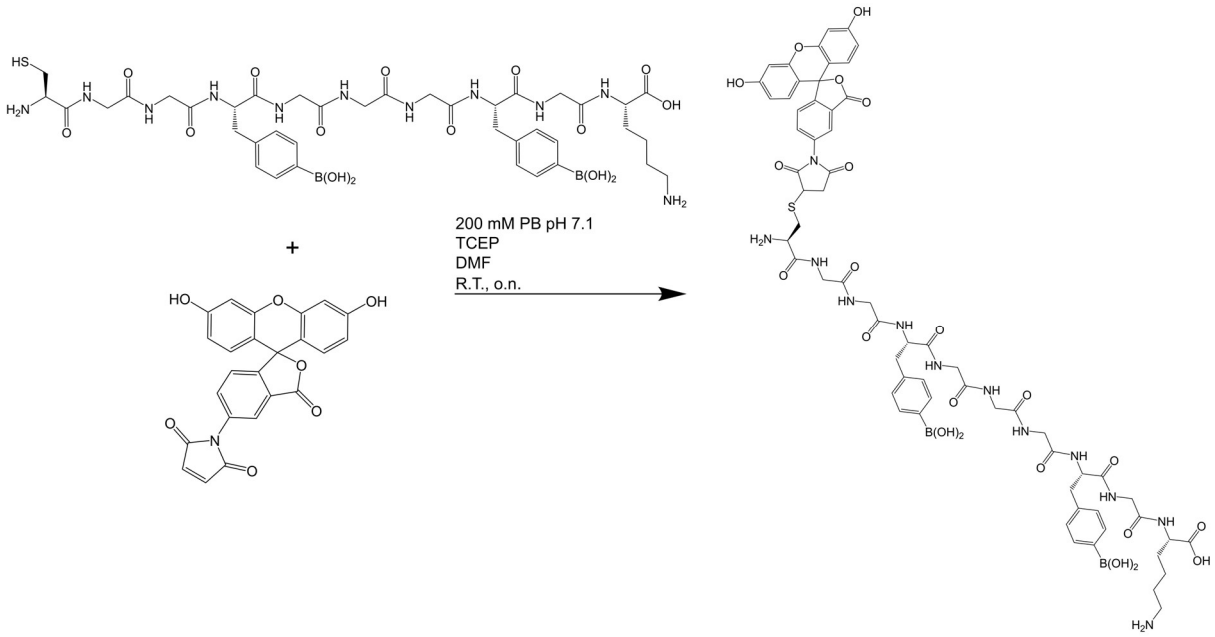

Figure 32: Synthesis route BAP2-Fluorescein: Cysteine-BAP2 is attached to fluorescein via Michael-type addition.

Next, BAP1-Fluorescein and BAP2-Fluorescein were utilized to screen their affinity towards tetraserine motifs.

4.2.3.4 MST BAP1-Fluorescein with TSP1 to TSP3

Before carrying out the MST experiment, BAP1-Fluorescein was again titrated to determine an appropriate concentration for the measurement (data not shown).

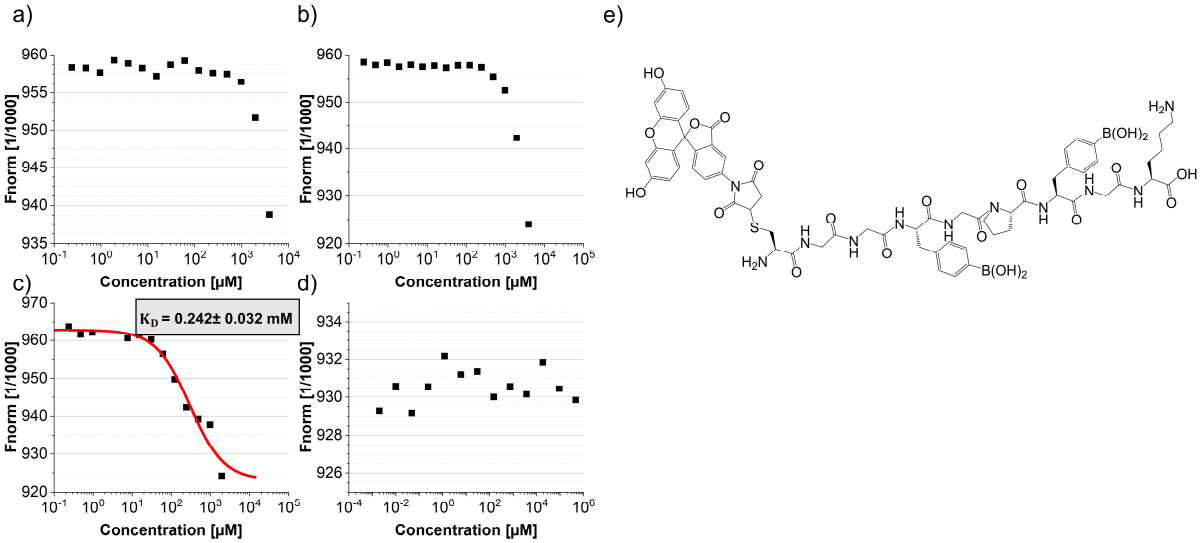

Figure 33: MST of TSPs with BAP1-Fluorescein: MST titration experiments of TSPs using BAP1-Fluorescein as a dye. Changes in fluorescence intensities and temperatures are depicted for (a) TSP1 (b) TSP2, (c) TSP3 and (d) fructose. (e) Molecular structure of BAP1-Fluorescein. The dissociation constant calculated by the sigmoidal fit of TSP3 is depicted. Measurements were conducted in 1:9 vol/vol DMSO ABC buffer pH 7.4 10 mM. 0.071 µM was used as dye concentration. Errors are standard deviations obtained from the sigmoidal fits.

As in the ARS displacement assay, TSP2 and fructose were also tested as a negative and positive control, respectively. Relevant interactions between BAP1-Fluorescein and diols were exclusively observed for alanine spacer containing TSP3 (Figure 33). Thus, only for this peptide, a sigmoidal binding curve could be fitted, and a K_d of 0.242± 0.032 mM determined. Contrarily, no reaction between fructose and BAP1-Fluorescein was detected independent of the fructose's concentration. For BAP2-Fluorescein, similar observations were made.

4.2.3.5 MST BAP2-Fluorescein with TSP2

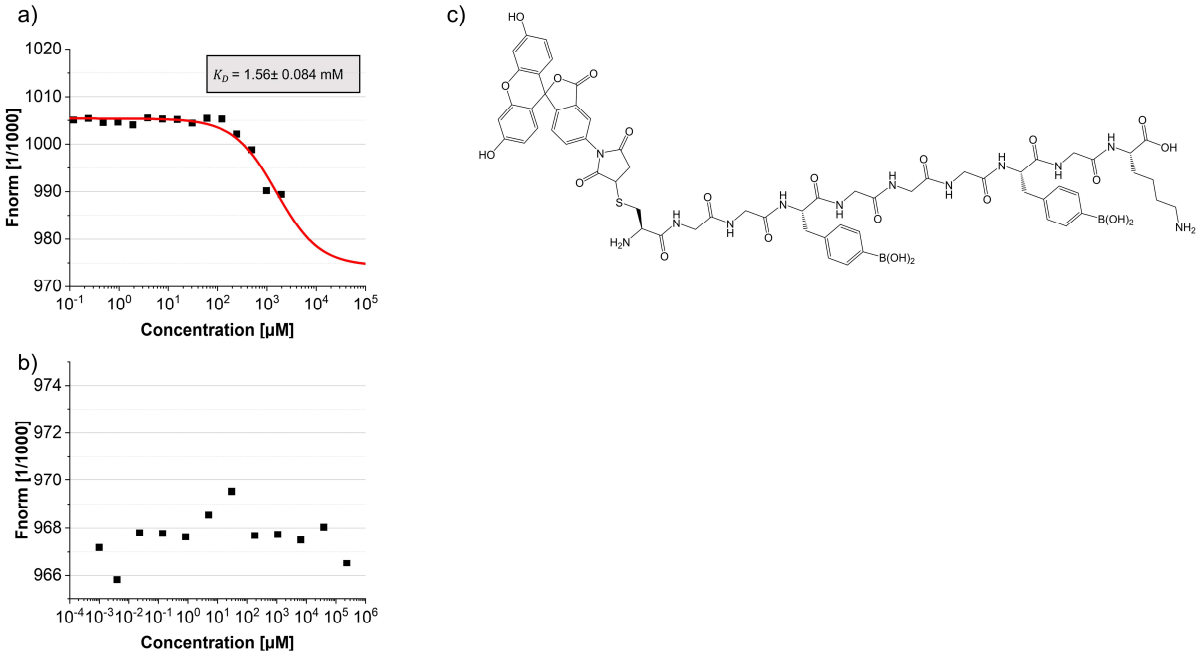

Figure 34: MST of TSP with BAP2-Fluorescein: MST titration experiments of TSP2 using BAP1-Fluorescein as a dye. Changes in fluorescence intensities and temperatures are depicted for (a) TSP2 and (b) fructose. (c) Molecular structure of BAP2-Fluorescein. Dissociation constant calculated by the sigmoidal fit of TSP3 is depicted in red. Measurements were conducted in 1:9 vol/vol DMSO ABC buffer pH 7.4 10 mM. 0.08 µM was used as dye concentration. Errors are standard deviations obtained from the sigmoidal fit.

As for BAP1-Fluorescein MST experiments, BAP2-Fluorescein also did not show any significant binding of fructose in the investigated concentration window (Figure 34). However, it was able to react with TSP2, but with a dissociation constant of 1.56±0.084 mM and hence with a lower binding affinity than the other tetraserine-bisboronic acid complex (Figure 33).

The fact that the introduction of a short PEG linker significantly increased the binding affinity in SAPF experiments (Figure 24, Figure 26) and that BA cannot interact with fructose when coupled to a peptide backbone (Figure 33), makes it probable that steric contributions are the origin.

4.3 SAPs

4.3.1 SAP selection

Multivalency cannot only be achieved by introducing two reactive sites into one peptide, but also by supramolecular self-assembly. Presenting hydroxyl groups on the

surface of an SAP nanofibril could lead to proximity effects and increase the local amount of possible reaction partners for BAs. For the SAP design, the previously determined interaction parameters of diserine peptides were taken into consideration. SAPF2 and SAPF3 which exhibited promising binding affinities towards BAs were coupled to the CKIK motif affording SAP1 and SAP3 (Figure 35).

SAP1: CKIKISAQINM	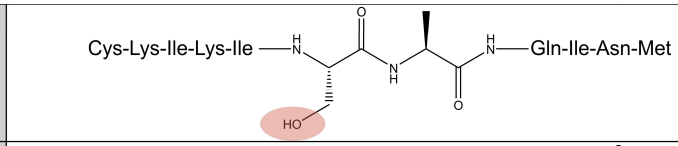
SAP2: KIKI + SAP1	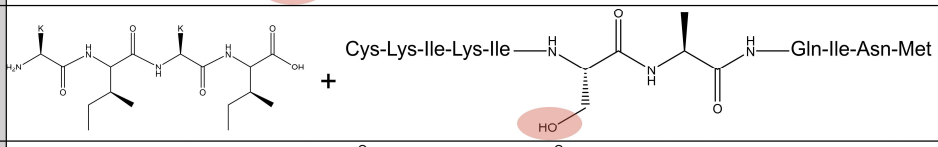
SAP3: CKIKISASQINM	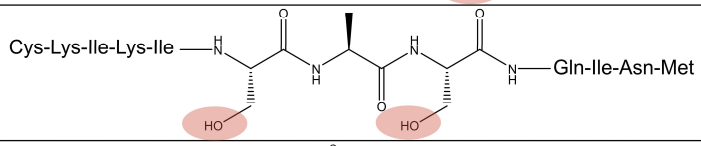
SAP4: CKIKINQINM	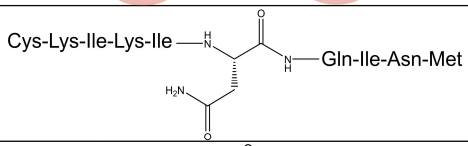
SAP5: CKIKISQINM	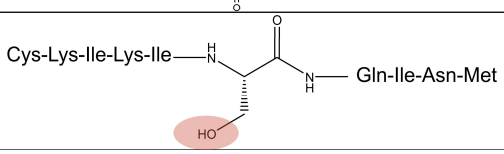

Figure 35: SAP selection: Abbreviations and molecular structures are depicted. For better visualization, three or one letter codes of AA which are not involved in BA binding are utilized. Possible BA-interaction partners are labelled in red.

SAP2 represents a co-assembly approach of KIKI and SAP1. Since the hydroxyl groups could in principle also be shielded by the peptide nanofibril, better accessibility could be achieved by co-assembly. SAP2[b], the co-assembly of SAP3 and KIKI is not illustrated since it was not further used after CD measurements. SAP4 served as a negative control where the serine was substituted by a structurally and chemically related asparagine residue. SAP5 with the standard peptide sequence CKIKISQINM was chosen as an additional reference (Figure 35). The SAPs were synthesized using standard Fmoc SPPS synthesis and successfully purified by reversed phase HPLC (Figure S 10, Figure S 11). KIKI was obtained from Yu-Liang Tsai and CKIKI(O-C(O))SQINM was purchased. Since the depsipeptide function did not play a role in the following experiments, it will be abbreviated as CKIKISQINM in the following.

4.3.2 TEM imaging SAP

TEM images of SAPs were prepared to investigate the effect of AA shuffling. The results revealed distinct morphologies.

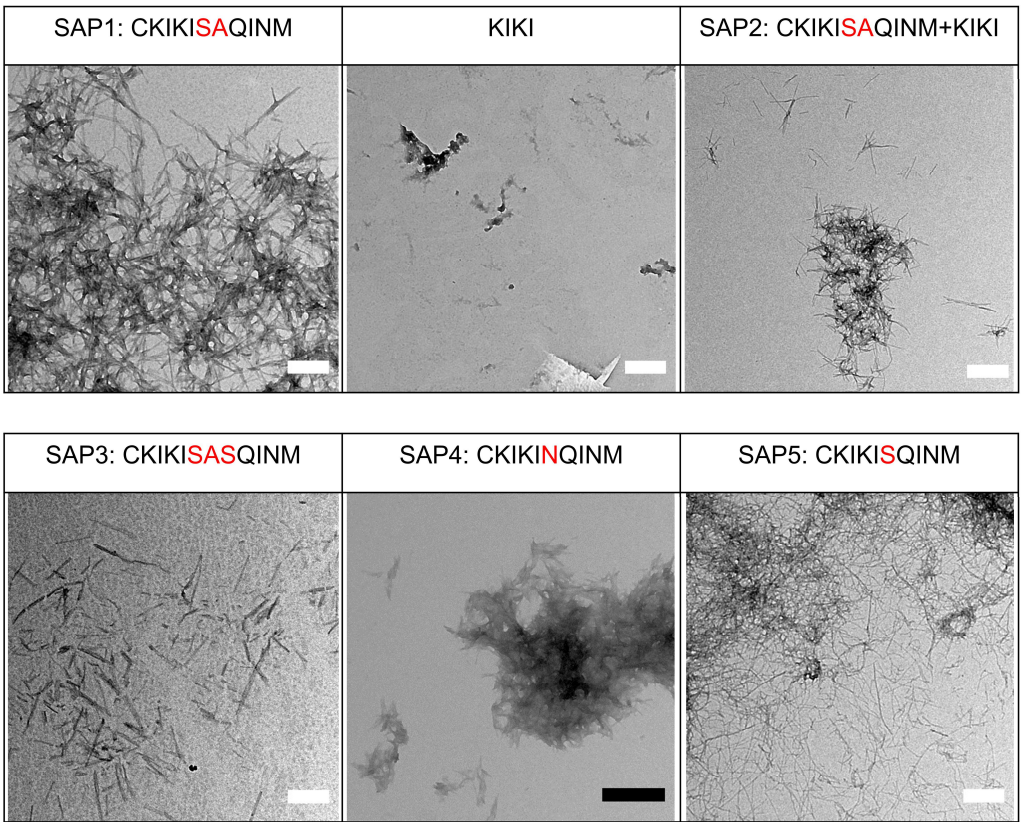

Figure 36: TEM images of designed SAPs: Sequences are presented as AA one letter code and relevant residues marked in red. Scale bars are 0.5 µm. Concentrations are 1 mg mL^{-1} in 10 vol% DMSO ABC buffer pH 7.4.

The substitution of a single AA had a drastic impact on the final morphology. SAP1 exhibited well-defined nanofibers (Figure 36). To assess the impact of KIKI on the dynamics of SAP1, this peptide was screened as well. However, no nanostructure formation occurred under the given conditions. Co-assembled with SAP1 (SAP2), KIKI led to the disruption of the nanofibers and short nanofiber formation resulted. Interestingly, expanding the sequence with one additional serine residue (SAP3) would also have a negative impact on the fibre's stability. Substituting the serine with an asparagine, led to aggregation of short nanofibers. As expected, SAP5 formed well-defined nanofibrils (Figure 36).

4.3.3 CD of SAPs

To investigate the secondary structures of the SAPs and confirm the observations from TEM imaging analysis, circular dichroism (CD) measurements were carried out. The spectra of SAP1, SAP3, SAP4 and SAP5 indicated that residue shuffling did not have a strong impact on the secondary structure.

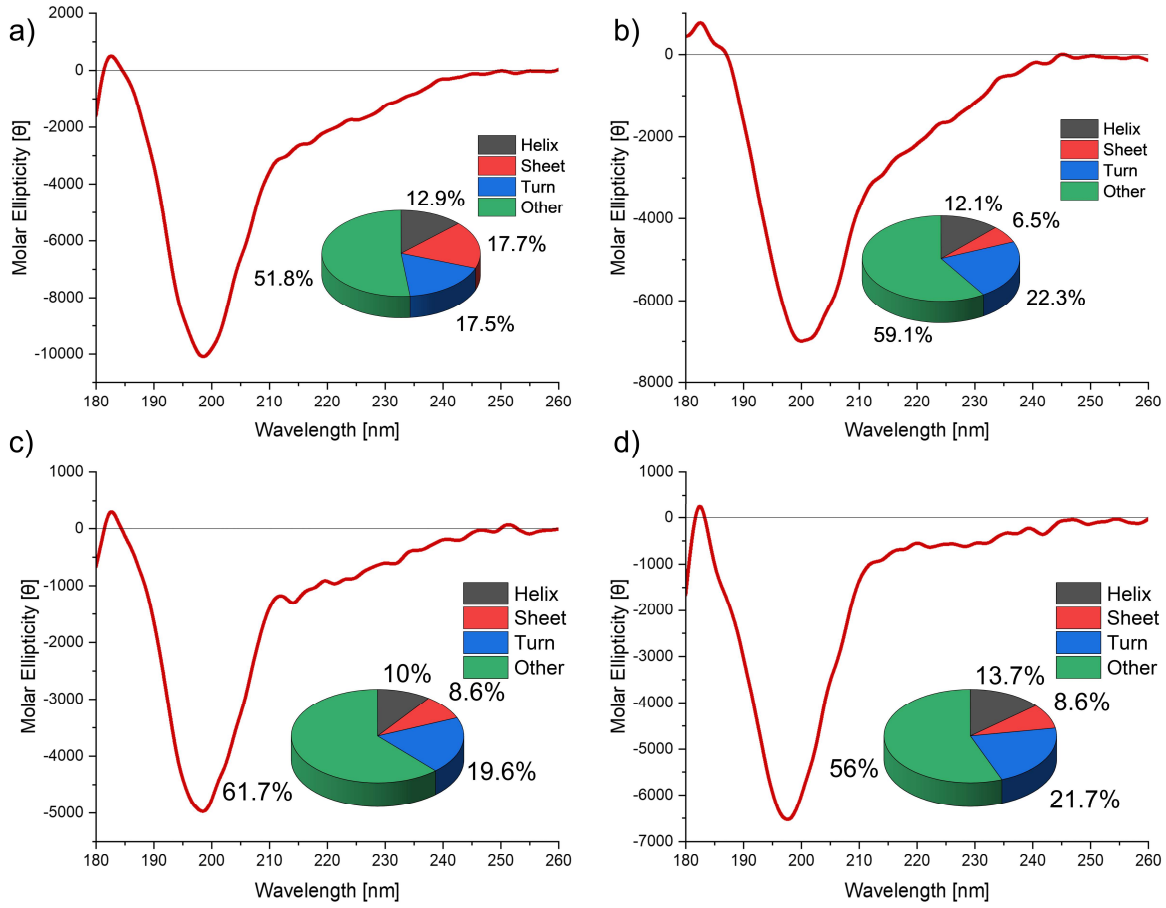

Figure 37: CD spectra of SAP1, SAP3, SAP4 and SAP5: The molar ellipticities of (a) SAP1, (b) SAP3, (c) SAP4 and (d) SAP5 are depicted. Inlets show secondary structures in percentages as calculated by the PLS model. Measurements were performed in MQ water at a concentration of 100 µM.

All four SAPs showed negative bands at approximately 200 nm and a positive band at around 180 nm which is characteristic for β-sheets. However, a maximal β-sheet content of 17.7 % was calculated for SAP1 (Figure 37). Surprisingly, the secondary structures of SAP3, SAP4 and SAP5 were predicted to be almost identical. High portions above 50 % of random coil structures were predicted for all four SAPs. Similar results were reported for SAP2, SAP2[b] and KIKI.

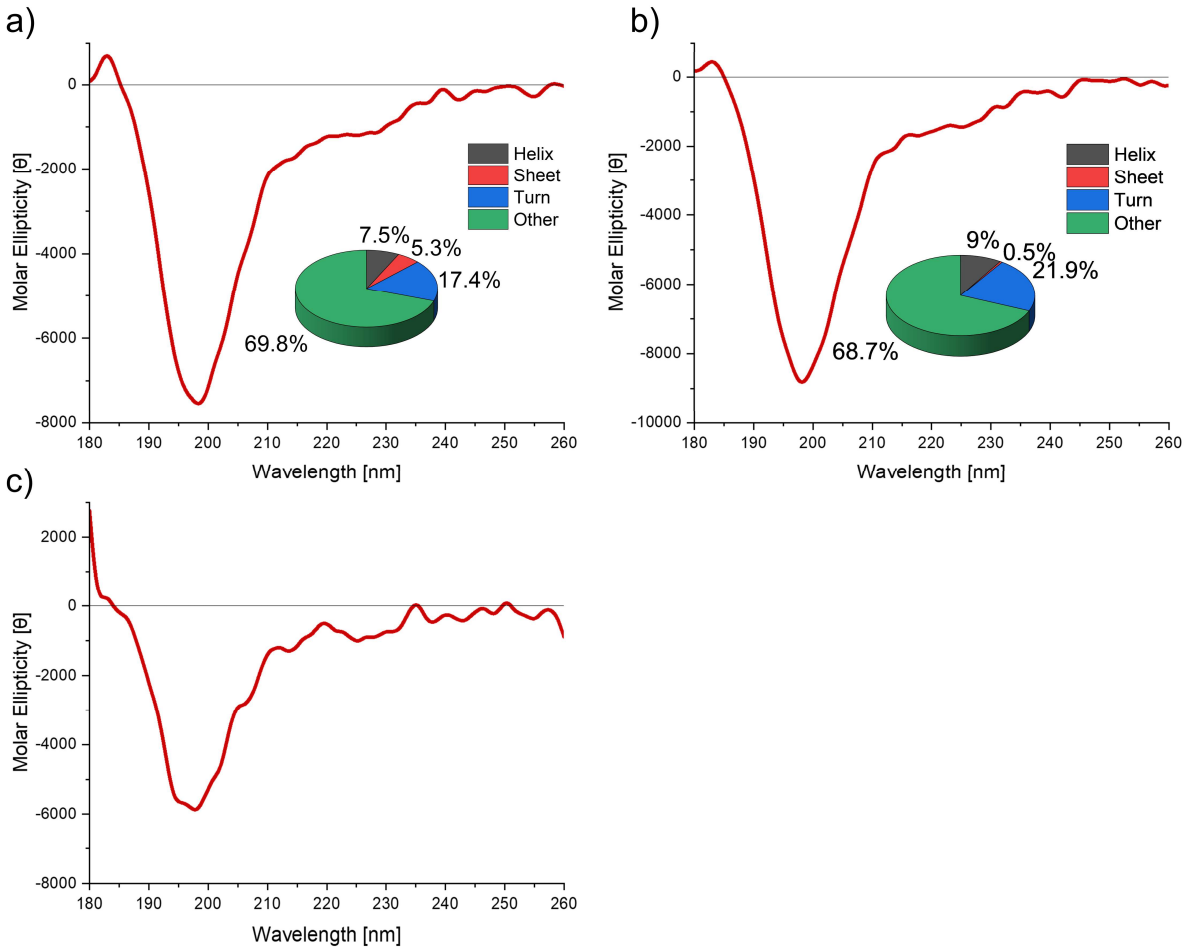

Figure 38: CD of SAP2, SAP2^{b} and KIKI: The molar ellipticities of (a) SAP2, (b) SAP2^{b} and (c) KIKI are depicted. Inlets show secondary structures as calculated by the PLS model. Measurements were carried out in MQ water at a concentration of 100 µM.

The β-sheet content of SAP1 was decreased from 17.7 % to 5.3 % when co-assembled with KIKI as can be seen by the SAP2 CD spectrum (Figure 38 a). This trend was also observed for SAP2^{b} where the co-assembly decreased the β-sheet content from 6.5 % to 0.5 %. KIKI itself did not form any β-sheets according to the CD spectrum the model failed to predict reliable data for this peptide (Figure 38 c).

The destabilization of KIKI co-assembled peptides was observed for TEM and CD analyses. However, the substitution of one or two amino acids did not drastically change the secondary structures according to the CD results. Furthermore, CD analysis predicted at least 50 % random coil content for all SAPs even though in TEM analysis organized structures for SAP1 and SAP5 were reported.

The discrepancies between TEM and CD results can be explained by different preparation methods. As described previously, the self-assembly is affected by pH, ionic strength, temperature, and peptide concentration, to name a few. Since it is more crucial to assess the final morphology of the SAPs in the buffer conditions used for later experiments, this was chosen as condition in TEM sample preparation. However, using these conditions in CD would not allow to detect the characteristic peak for β-sheets below 190 nm. The absence of ions and the lowered pH value of MQ water presumably changed the way of assembly and therefore the secondary structures. Since the destabilizing effect of KIKI was more severe for SAP3 than for SAP2, SAP2^{b} was not considered anymore for follow-up experiments.

4.3.4 Fibril binding assay

Since MST is not suitable for molecules which do not dissolve molecularly, a new fibril affinity assay was established which can provide semi-quantitative information about binding affinities between serine containing peptide nanofibrils and fluorescently labelled BAs.

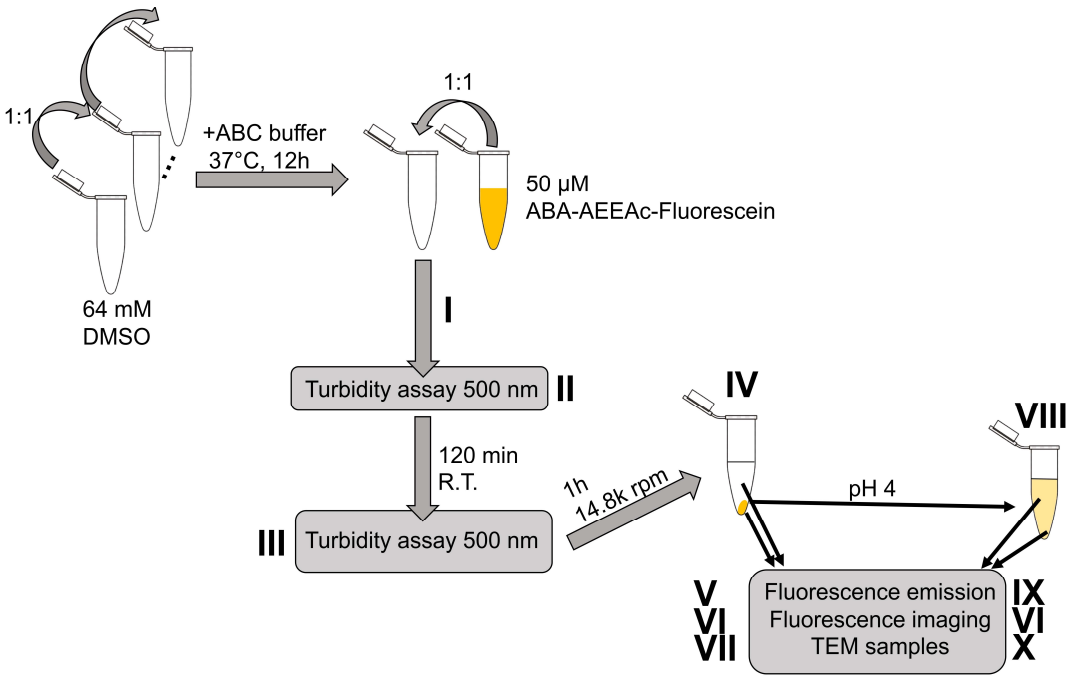

Figure 39: Fibril binding assay: The pipeline of the fibril binding assay. Roman numbers indicate steps in which data was collected. Peptides were dissolved in DMSO and serially diluted. ABA-AEEAc-BA was added and turbidity assays were conducted before and after incubation. After centrifugation, supernatants and pellets were analysed with fluorescence imaging and TEM imaging. Additionally, fluorescence emission was measured for the supernatant. The pellet was then acidified, and the supernatant and the pellet were analysed with the same methods.

However, this assay does not only allow to distinguish between strong and weak interaction, but also determine the level of specificity. ABA-AEEAc-BA (BA-dye) was chosen as a representative for BA drugs such as bortezomib. After serially diluting the peptides in DMSO, self-assembly was induced (Figure 39). Interestingly, after the addition of the BA-dye, a change in fluorescence for high peptide concentrations could be observed by naked eyes.

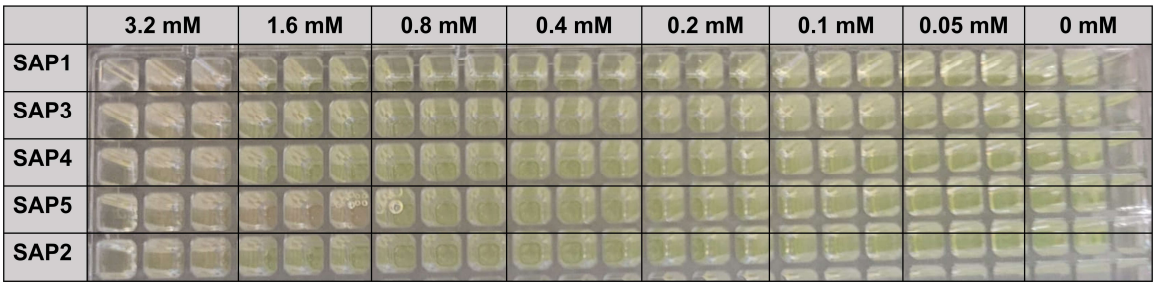

b)

Figure 40: Macroscopic observations of SAP-BA-dye mixtures in absoprtion plate: (a) SAP-BA-dye mixtures with different amounts of SAPs. The top row indicates peptide concentration. The BA-dye concentration was held constant at 25 µM. (b) Representative picture of the 3.2 mM and 1.6 mM SAP1 samples. Measurements were conducted in 1:9 vol/vol DMSO ABC buffer pH 7.4 10 mM. Pictures correspond to **I** in Figure 39.

Titration of the different SAPs to a constant amount of BA-dye revealed that all SAPs interacted with the dye at a concentration of 3.2 mM leading to a change in colour (Figure 40). Furthermore, SAP5 showed this macroscopic effect also for 1.6 mM (Figure 40 a). This suggests interaction between the peptide nanostructures and the BA-dye. To assess whether the interaction with the BA-dye would change particle aggregation overtime, a turbidity assay was performed next (Figure 39 **II, III**).

4.3.4.1 Turbidity assay

The turbidity assay is a measure of particle aggregation where the number of aggregates correlates with absorption at 500 or 600 nm [93]. By measuring this value overtime, changes in particle aggregation can be detected. However, due to high standard deviations, the results obtained at 600 nm did not allow to deduce relevant trends (Figure S 29). Since fluorescein exhibits an absorption peak at 500 nm, these measurements provided more meaningful data.

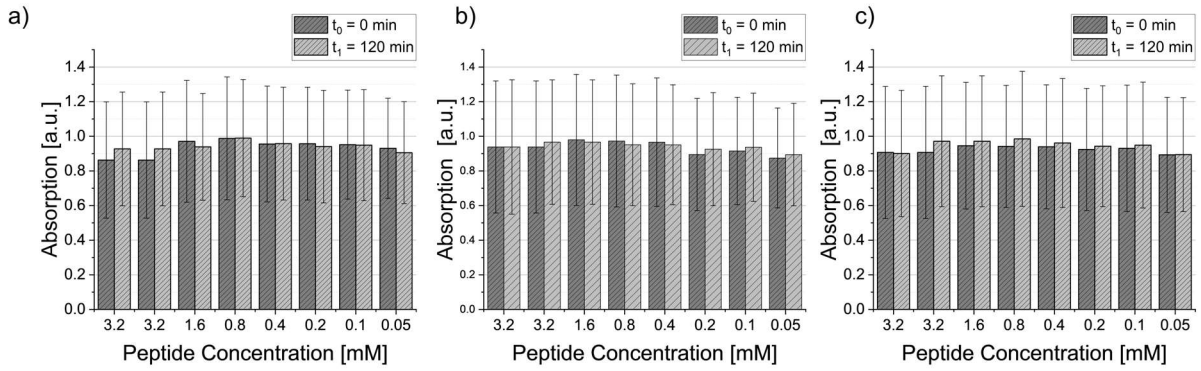

Figure 41: Absorption measurements SAP1, SAP2, SAP3: Absorption of (a) SAP1, (b) SAP2 and (c) SAP3 was detected before and after incubation for two hours. No drastic change in absorption was observed after the incubation of 120 min. Highest peptide concentrations show lower absorption signals. Error bars are standard deviations calculated by error propagation. Results correspond to **II** and **III** in Figure 39. Absorption was measured at 500 nm. N=3.

For SAP1, SAP2 and SAP3, incubation of two hours did not lead a change in absorption of the incident light beam (Figure 41). Further to note was the slight decrease in absorption at the highest peptide concentration of 3.2 mM. This trend was even more apparent for the SAP4 and SAP5 samples.

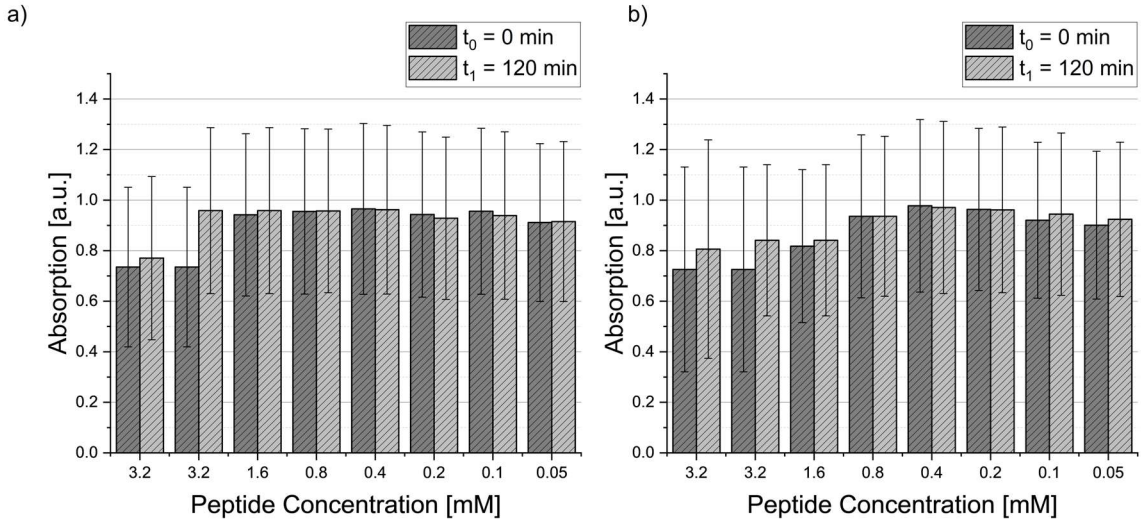

Figure 42: Absorption measurements of SAP4, SAP5: Absorption of (a) SAP4 and (b) SAP5 was detected before and after incubation for two hours. No relevant change in absorption was detected after the incubation of 120 min. Highest peptide concentrations show lower absorption. Error bars are standard deviations calculated by error propagation. Results correspond to **II** and **III** in Figure 39. Absorption was measured at 500 nm. N=3.

The detected absorptions for SAP4 and SAP5 corresponded well to the macroscopic observations (Figure 40). The lowest absorption was detected at the highest peptide

concentration. SAP5 also showed this trend at lower concentrations as compared to all other SAPs, consequently pure quenching effects due to an increased amount of peptide can be excluded (Figure 41, Figure 42). By increasing the peptide's concentration, peptide eventually interacts with the BA-dye and precipitates. Hence less fluorescein molecules are dissolved and thus cannot contribute to the absorption. To note, the absorption signal did not change drastically overtime for all samples indicating no relevant changes of interaction. Next, the samples were centrifuged to pelletize the peptide nanofibril-BA-dye precipitate.

4.3.4.2 Fluorescence emission 1st supernatant

In line with the absorption measurements, BA-dye mixtures at high peptide concentrations formed an orange pellet after centrifugation (Figure 43).

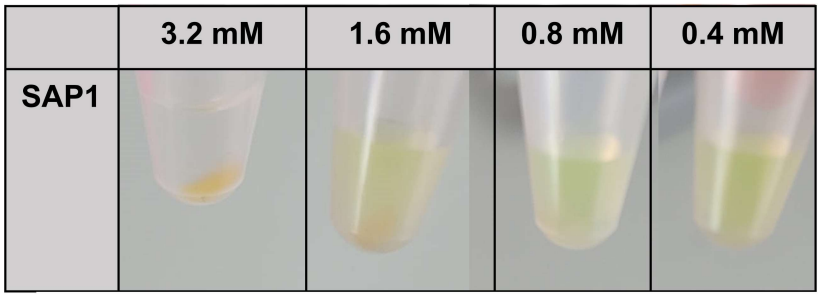

Figure 43: Pellet formation after centrifugation: After centrifugation of peptide-BA-dye mixtures, the formation of fluorescent pellets was observed. SAP1 at different concentrations is shown representatively. The BA-dye concentration was held constant at 25 µM for all samples. Measurements were conducted in 1:9 vol/vol DMSO ABC buffer pH 7.4 10 mM. Pictures correspond to **IV** in Figure 39.

The supernatant was removed, and the fluorescence emission measured. Strong interaction between the SAPs and the BA-dye would lead to a low fluorescence intensity.

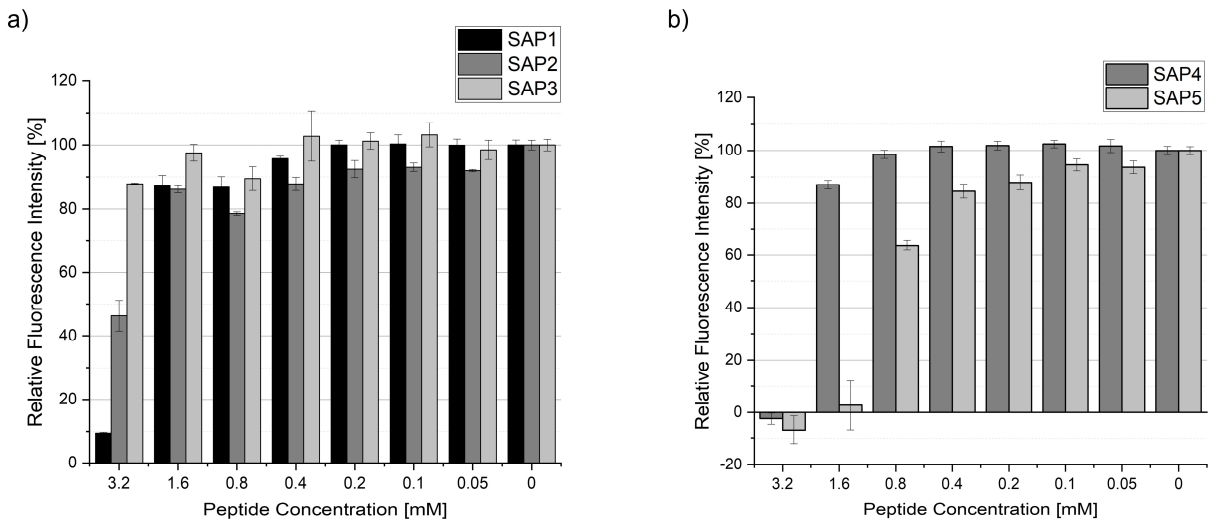

Figure 44: Relative fluorescence intensities of the first supernatant of SAP-BA-dye mixtures: High peptide concentrations show a decrease in relative fluorescence intensity as compared to BA-dye alone (0 mM peptide). (a) Relative fluorescence intensities of SAP1, SAP2, SAP3 at different concentrations (b) Relative fluorescence intensities of SAP4, SAP5 at different concentrations. Fluorescence emission was referenced against samples without peptide. The BA-dye concentration was held constant at 25 µM for all samples. Measurements were conducted in 1:9 vol/vol DMSO ABC buffer pH 7.4 10 mM. Pictures correspond to **V** in Figure 39. Error bars are standard deviations calculated by error propagation. $\lambda_{excitation}$ = 495 nm, $\lambda_{emission}$ = 556 nm. N=3.

A significant decrease in relative fluorescence intensity was detected at a peptide concentration of 3.2 mM for all SAPs except for SAP3 (Figure 44). As also observed macroscopically and by absorption measurements (Figure 40, Figure 42), the affinity of SAP5 was the highest towards the BA-dye. At a SAP5 concentration of 0.8 mM an approximately 60 % decrease in fluorescence intensity was detected.

Next, to simulate drug release, a defined volume of the SAP-BA-dye pellets was diluted and the pH value adjusted to pH 4 (Figure 39). This step was required to determine whether the interaction between the SAPs and the BA-dye was unspecific or if the SAPs interact specifically with the BA-dye by the formation of boronic esters. By decreasing the pH, the acid labile ester bonds would be cleaved, and the BA-dye released. After centrifugation, the BA-dye would be evenly distributed in solution. This is valid under the constraint that the peptide nanofibril is stable under pH adjustment. If the interaction was purely unspecific, the SAP-BA-dye precipitate would pelletize again. After centrifugation, SAP5 showed distribution of fluorescence throughout the whole Eppendorf tube (Figure 45).

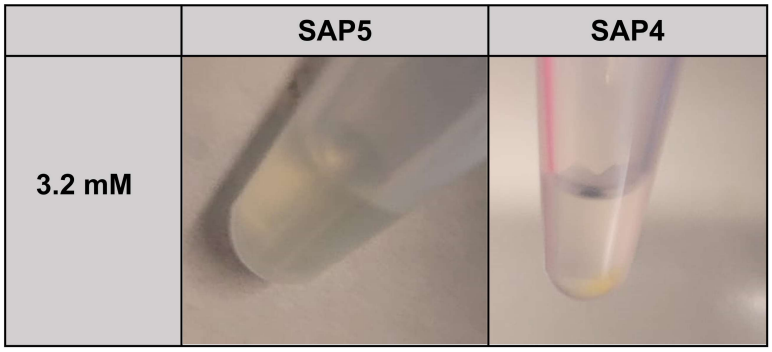

Figure 45: Macroscopic observation of supernatants after acidification: Distribution of BA-dye in solution was observed for SAP5 after centrifugation. In contrast, SAP4 showed the formation of a BA-dye pellet and is representatively shown for all other SAPs. 0.01 vol% TFA MQ was utilized to adjust the pH to 4.0. Pictures refer to **VIII** in Figure 39.

The other SAPs showed again a formation of a pellet after centrifugation (Figure 45). For SAP5, the results indicate that the BA-dye was released from the peptide nanofibril and thereby goes back in solution which prevents the formation of an orange pellet. The supernatant was then collected, and fluorescence emission was measured.

4.3.4.3 Fluorescence emission 2nd supernatant

From macroscopic observations, a high fluorescence signal for the supernatant of SAP5 was expected. However, the fluorescence signals of the SAPs were too low to obtain meaningful data (data not shown) This can be explained by the fact that only a part of the pellet after the first centrifugation step was transferred and acidified. To obtain more meaningful data, the final pellet obtained from **XIII** (Figure 39) and depicted in Figure 45 was diluted and fluorescence emission measurements were carried out.

4.3.4.4 Fluorescence emission 2nd pellet

The fluorescence emission of the final diluted pellet in **VIII** (Figure 39) was measured. Unspecific binding would lead to pellet formation and therefore to an increase of fluorescence intensity after acidification. Specific binding, in turn, would show a fluorescence intensity like the reference since the BA-dye would be evenly distributed in the supernatant and the pellet.

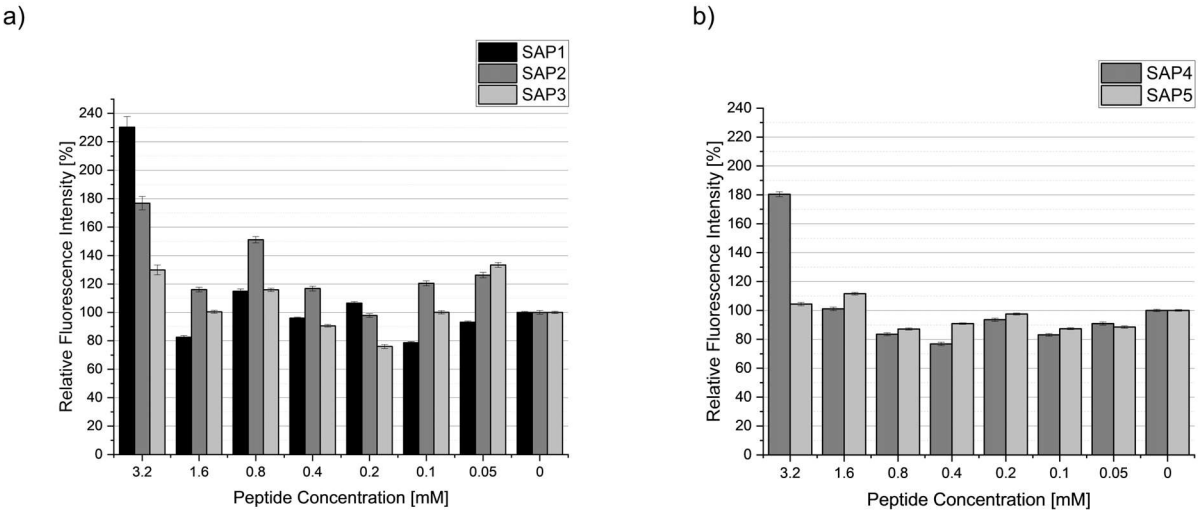

Figure 46: Relative fluorescence intensities of the final pellet of SAP-BA dye mixtures: High peptide concentrations show an increase in relative fluorescence intensity as compared to BA-dye alone for SAP1 to SAP4 (0 mM peptide). (a) Relative fluorescence intensities of SAP1, SAP2, SAP3 at different concentrations (b) Relative fluorescence intensities of SAP4, SAP5 at different concentrations. Fluorescence emission was referenced against samples without peptide. Measurements were conducted after acidification, centrifugation, and dilution. Pictures correspond to **IX** in Figure 39. Error bars are standard deviations of several measurements per well and were corrected for error propagation. $\lambda_{excitation}$ = 495 nm, $\lambda_{emission}$ = 556 nm. N=1.

The relative fluorescence intensities of the final pellet are in line with the macroscopic observations and the absorption measurements described previously (Figure 45, Figure 46). SAP5 was the only investigated SAP which showed similar fluorescence intensities as compared to the BA-dye reference indicating that the BA-dye was released from the peptide nanofibril given that the fibrils were still intact (Figure 46 b). The comparably low relative fluorescence intensity of around 130 % for SAP3 could be attributed to the drawbacks of the assay itself. Since SAP3 already has already lost a portion of BA-dye in the first centrifugation step due to inefficient BA-dye complexation, the final pellet consequently also showed a decrease in relative fluorescence signal (Figure 44). This can better be visualized in the fluorescence intensity double plot.

4.3.4.5 BA-dye release: a comparison

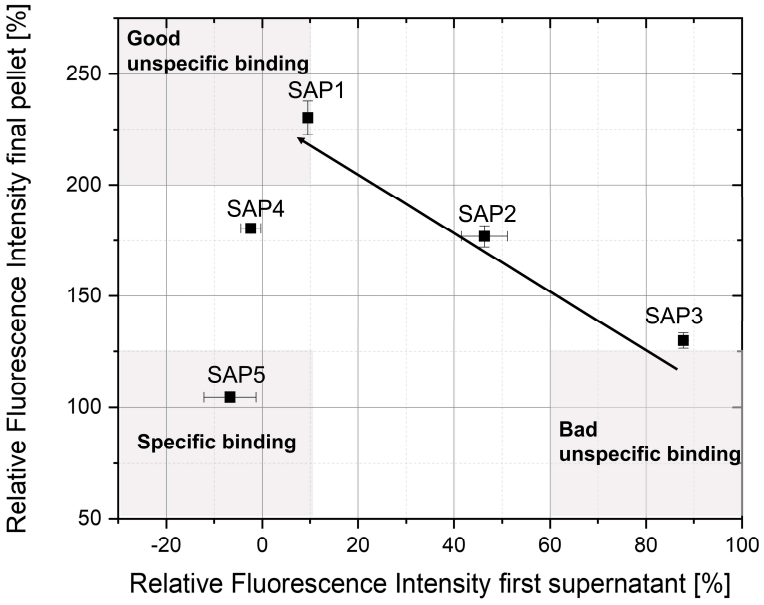

Figure 47: Summary of fibril affinity assay: Relative fluorescence intensities of the first supernatant and the final pellet are plotted. For better visualization, only the 3.2 mM peptide concentrations are depicted. SAP5 is the only candidate showing properties expected from specific binders. Error bars are standard deviations corrected for error propagation.

The plot visualizes the regimes expected from BA-dye interaction partners with specific and unspecific binding (Figure 47). Even though the thresholds of the regimes were chosen arbitrarily, the plot still provides information about the tendencies between the SAPs. The plot only shows the 3.2 mM peptide concentration samples. Due to weaker binding affinities of lower peptide concentrations, this regime would need to be adjusted and therefore, these concentrations were omitted. A general trend from SAP3 to SAP1 was observed where the binding affinity increased subsequently. In line with the previous experiments, SAP5 was the only candidate laying in the regime of specific binding. As SAP4 was still closest to the regime of specific binding and represents the negative control, SAP5 and SAP4 were further investigated with fluorescence microscopy and TEM imaging.

4.3.4.6 TEM imaging SAP4 and SAP5 BA dye samples

TEM samples of the fibril affinity assay exhibited different morphologies for SAP4 and SAP5 (Figure 39).

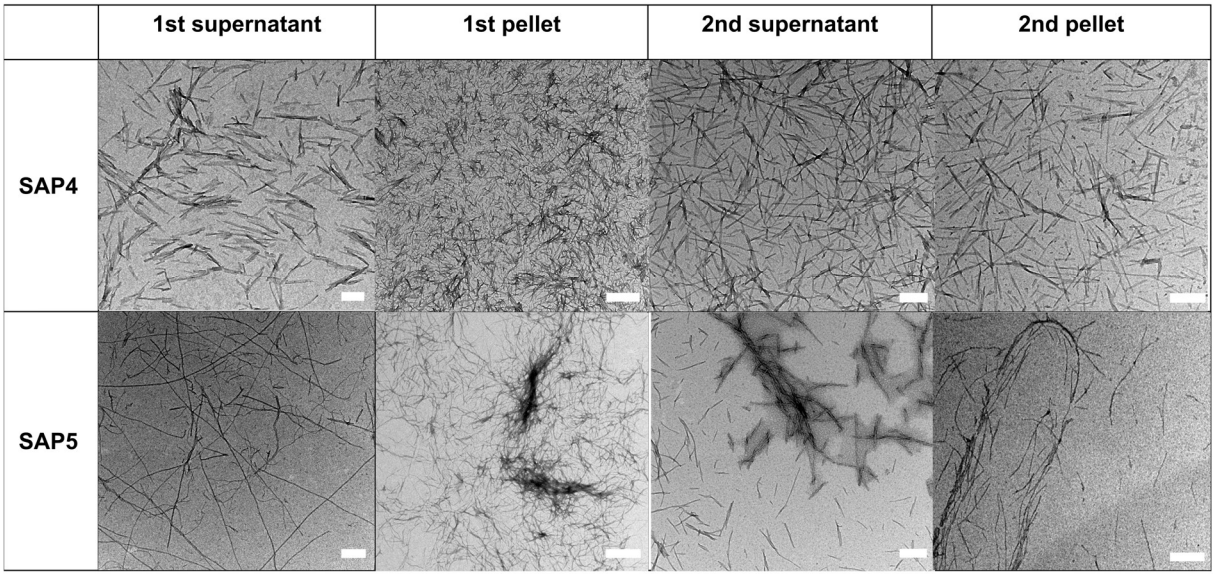

Figure 48: TEM images of SAP4 and SAP5 supernatants and pellets: TEM images depict supernatants and pellets of SAP4 and SAP5 as described accordingly. Only the highest peptide concentration (3.2 mM) is shown for better visualization. Scale bars are 0.2 µm for supernatants and 0.5 µm for pellets, respectively.

Interestingly, the morphology of SAP4 slightly changed upon addition of the BA-dye as compared to the native TEM measurement from high aggregated to less aggregated nanofibers (Figure 36, Figure 48). The morphology of SAP5, in contrast remained the same and the nanofibrils were still intact after the first centrifugation step. However, after acidification and centrifugation individual peptide nanofibril fragments were reported presumably due to acid induced fragmentation.

The peptide fibril binding assay provided insights into the interaction between a BA-dye and SAPs of different primary sequence and morphology. Even though all SAPs interacted with the BA-dye at a concentration of 3.2 mM, different binding affinities were detected. The SAPs' morphology seemed dictated the affinity towards the BA-dye. Less ordered structures such as SAP3 and SAP2 as determined by TEM imaging, cannot interact strongly resulting in poor binding efficiencies (Figure 36, Figure 48). High surface area increases potential interaction sites and thus SAP1 and SAP5 that form nanofibers and nanofibrils are more efficient binders. SAP4 exhibited stable short fibre formation upon BA-dye addition and therefore intermediate binding strength (Figure 47). However, the drawbacks of the assay are several fold. First, the two centrifugation steps and the pH adjustment can eventually lead to SAP disassembly which was also observed for SAP5 (Figure 48) and second, the dilution

of the pellet upon acidification does not allow to detect reliable fluorescent signals for the supernatant. Furthermore, the absolute fibril mass also has an impact on the final affinity. However, due to the lack of time similar conversion rates were assumed. Possible solutions will be discussed later.

4.3.5 SAP-BA hydrogel

4.3.5.1 Synthesis bisboronic acid PEG cross-linker

The intramolecular rearrangement of the depsipeptide shift reveals a hydroxyl group than can potentially react with BAs. By cross-linking the peptide nanofibrils with a bisboronic acid cross-linker, a novel self-healing hydrogel could be afforded (Figure 1). To this end, linear PEG_{1000}-diamine was chosen to couple 4CPBAs via a condensation reaction on the free amines. The product was further purified by reversed phase HPLC as determined by LCMS (Figure S 20).

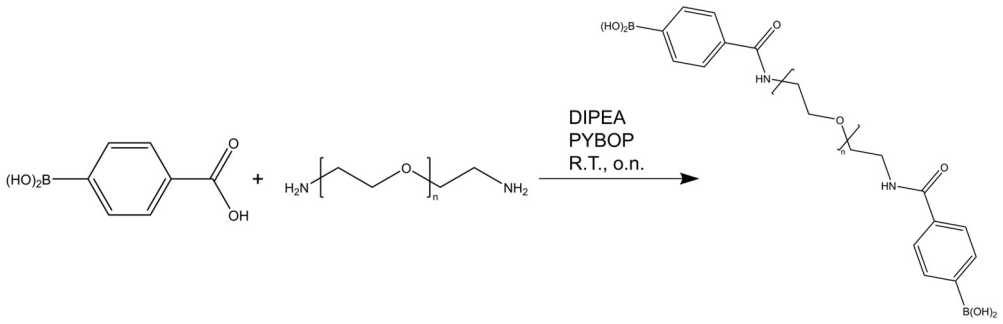

Figure 49: Synthesis of bisboronic acid PEG cross-linker: The linear PEG_{1000} cross-linker was synthesized by a condensation reaction assisted by DIPEA and PYBoP as activator base and activator, respectively.

Even though the most abundant mass peaks of the product corresponded to the bifunctional molecule, signals of lower molecular weight that indicate mono-functionalization were detected as well. Nevertheless, a vial inversion test was carried out to assess whether the cross-linker would provide additional stability to the SAP hydrogel.

4.3.5.2 SAP-BA vial inversion test

To investigate whether the depsipeptide SAP5 can form hydrogels by itself, a titration experiment was carried out to determine a suitable test concentration (data not shown). A final hydrogel concentration of 0.15 wt% was chosen since at this concentration the

peptide would start to form granules but would still fail the vial inversion test. The cross-linker was mixed in half molarity compared to the peptide to keep the potential reaction partners (hydroxyl and BA) constant. The amount of depsipeptide SAP5 was decreased accordingly to keep the final concentration of 0.15 wt% constant. Since PEG itself could have an impact on the viscosity, the non-functionalized molecule PEG-diamine served as a negative control. Unfortunately, none of the samples passed the vial inversion test.

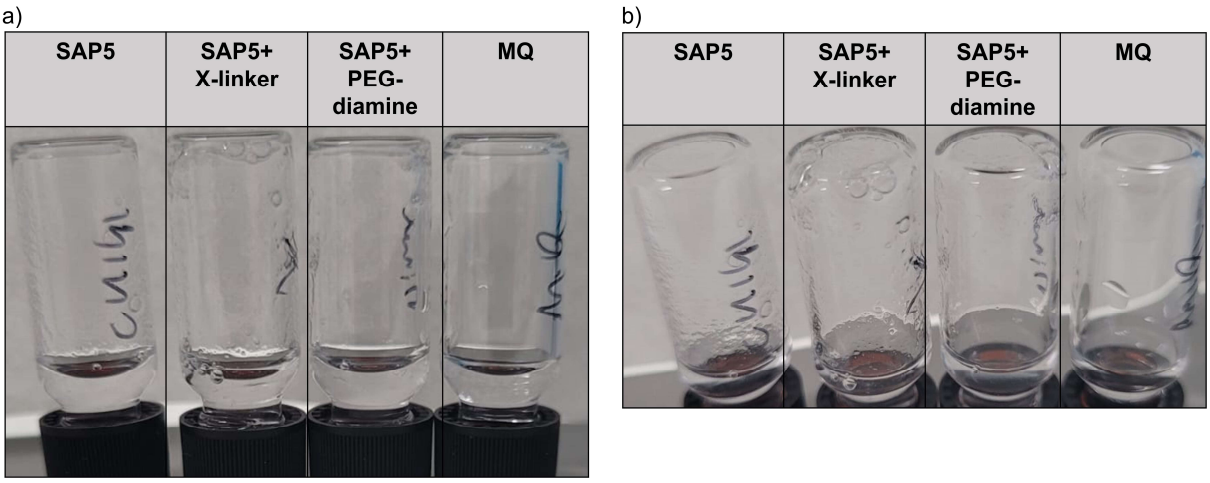

Figure 50: SAP-BA hydrogel vial inversion test: (a) Vial inversion test of SAP5, SAP5 + bisboronic acid cross-linker, SAP5 + PEG-diamine and MQ. Final concentration of all samples was 0.15 wt% (except for MQ) (b) Magnification of (a) showing granules in SAP5 and SAP5+bisboronic acid cross-linker sample. Samples were first dissolved in MQ 0.1 vol% TFA and then pH neutralized with PB pH 9 300 mM.

Small granules were formed for SAP5 and SAP5 + cross-linker samples (Figure 50 b). This observation was absent for the two negative control SAP-PEG-diamine and MQ samples which indicates that the boronic acids at least contributed partly to the gelation. However, the granule formation was still strongest for SAP5 without any cross-linker. Thus, the expected stabilizing effect of the BA cross-linker remained absent. However, the experiment could be optimized which will be discussed in the next section.

5 Conclusions and Outlook

Responsive biomaterials are promising candidates for biomedical applications. The spatial-temporal control is crucial to make clinical translation ultimately possible. In this study, pH-responsive depsipeptides were chosen to react with boronic acids. This combines pH responsive reversible (boronate ester) and pH responsive irreversible (depsi-shift) chemistry which possibly opens the door for new smart biomaterials. To first examine the ability of BAs to react with hydroxyl groups on a peptide backbone, simple C-terminal peptide fragments of CKIKISQINM were designed and synthesized by standard Fmoc-SPPS. Interestingly, the ARS displacement and MST results suggest that not the number of serine residues, but the relative position of the C-proximal glutamine residue plays a crucial role for the affinity towards boronic acids. Most of the MST measured dissociation constants were in the same order of magnitude as reported for sorbitol and fructose (higher µM range) [59]. The dissociation constant between SAP3 and BA, however, was in the lower µM range similarly detected for catechols [61]. The C-proximal glutamine could probably provide similar stabilization effects as salicylhydroxamate. The mode of interaction still remains unresolved, however, DFT calculations and experimental data strongly suggest that a bidentate reaction is more prone to occur when two serine residues are spaced by an alanine residue. This is not in line with published data where only a fluorescence was reported when two consecutive serine residues reacted with a bisboronic acid rhodamine derivative [63]. The discrepancies are possibly related to the differences in geometry. NOESY analysis could be conducted to address the lack of knowledge regarding the mode of binding and the stabilization effect of the glutamine residue [61]. Furthermore, a negative control peptide sequence lacking the glutamine residue could synthesized and its binding affinity measured.

Since multivalency can function as a potentiator for binding affinities, possible diboronic acid peptides and their corresponding tetraserine binding partners were simulated *in silico* and synthesized. Exchanging ISASQINM with GSASGGSASGK and increasing the number of BA binding partners from one to two, resulted in a 7.5-fold increase in binding affinity. However, since the fructose binding was absent for the bisboronic acid condition and these observations could not be confirmed independently by other methods such as ARS, the experiment should be repeated. Moreover, the adjacent residues to the BA binding site are not identical. To make the systems more

comparable, control peptide sequences such as GSAGGSAGGK (control to TSP1) would be required. Even though the diboronic acid peptide sequences were designed such that two glycines space the boronic acids from the attached dye, it would still be favourable to introduce an AEEAc spacer to improve the binding affinity. The absence of fructose binding for dye-labelled diboronic acid peptides could be an indication that the fluorophore was attached too close to the binding site.

To achieve multivalency through supramolecular chemistry, promising peptide sequences containing or lacking serine residues were attached on the CKIK backbone to afford SAPs. The affinity towards boronic acids was assessed by a fibril affinity assay which was established in this work. Through centrifugation and acidification steps, the ability to complexate and release a BA-dye was investigated. The assay would in principle allow to distinguish between unspecific and specific interaction by reversible BA chemistry. The SAP morphology and eventually the total amount of fibrils dictated the overall BA binding affinity. Higher surface area of thin nanofibrils formed by CKIKISQINM promoted strong peptide-BA dye interaction as determined by fluorescence emission and imaging analyses. However, since the conversion rates of the SAPs were not determined yet, it could be that the total fibril mass had an effect on the binding affinity as well. Even though the nanofibrils were partly disassembled after acidification, it remains to be determined whether CKIKISQINM interacted specifically in the first place since increased surface area also comes with better accessible hydroxyl groups. However, since the assay comes with drawbacks such as possible rupture of nanofibrils and dilution steps, alternative measurement techniques are required. Fluorescence correlation spectroscopy would be one possible option [94]. Both molecules would require fluorescence labelling and it would be necessary to investigate whether co-assembled dye-labelled molecules disrupt the nanostructure. Alternatively, dialysis could also be conducted. The dialysate could be freeze dried and the fluorescence measured by fluorescence microscopy. Label-free methods such as SPR are in principle feasible as well, however, it would be favourable to employ a technique which does not rely on immobilized molecules [95]. To establish an assay which is closer to the final application, the BA-containing anticancer drug Bortezomib could be used.

To avoid the disintegration of supramolecular structures upon pH change, milder conditions (pH 6) could be tested. Sticking to the CKIKISQINM motif would require

thorough investigation of pH effects. Alternatively, co-assembly studies could be used to obtain a better control over pH stability and hydroxyl accessibility effects. Since KIKI seemed to destabilize the β-sheets when co-assembled to SAP1 as determined by CD and TEM analyses, CKIKIQI might be the better option [35]. Furthermore, peptide sequences that are persistent against pH changes could be chosen as well [53].

When the contribution of specific interaction is investigated thoroughly, disassembly strategies for the peptide nanofibrils must follow. The CKIKISQINM offers several vulnerable possibilities for disassembly. Serine could for example be phosphorylated by the tumor biomarker PKA; or the methionine residue oxidized by ROS which was already reported to induce disassembly [96,97]. This would be required for clearance *in vivo.*

Based on the results obtained in the nanofibril affinity assay, the depsipeptide CKIKI(O-C(O))SQINM was chosen to induce self-assembly and cross-linking by a bifunctional BA molecule simultaneously. The linear bisboronic acid PEG_{1000} cross-linker was selected to increase the stability of the self-healing hydrogel. Unfortunately, the samples failed the vial inversion test even though the peptide nanofibrils could bind to the BA-dye in the fibril affinity assay. This can be explained in several ways. First, the buffer systems utilized for switching the depsipeptides were different from the buffer used in the fibril affinity assay which could affect the binding affinities between the BA-crosslinker and the peptide nanofibril. Second, for the fibril assay, peptide nanofibrils were first assembled and then the BA-dye was added. In contrast for hydrogel formation, the components were first dissolved together in acidic conditions and then pH neutralized. Third, local concentration effects could play a role as well, since for the fibril affinity assay a 1:1 diol-BA interaction would lead to a change in observation, whereas for the hydrogel, two interactions need to occur to change the outcome. Screening higher concentrations (not only 1:1 BA-hydroxyl ratios), using a star-peg cross-linker and different molecular weight linkers could eventually help to overcome this issue. Higher molecular weight PEG cross-linkers could potentially entangle physically with the network allowing to increase the overall stability. Another approach would be to couple the synthesized diboronic acid peptides to maleimide SAPs and to co-assemble these nanofibrils then with serine containing peptide nanofibrils.

Once an increase in stability of the hydrogel is achieved, caging groups could be introduced to the N-terminus of the serine. Caging groups that are enzymatic- photo-, or redox-sensitive are suitable candidates for this.

Taken together, this study gives insights into reactions of BAs and hydroxyl groups presented by peptides which are different in 3D architecture and multivalency. This paves the way for pH responsive smart biomaterials that can be applied in biomedicine for drug delivery and as self-healing hydrogels.

6 Appendix

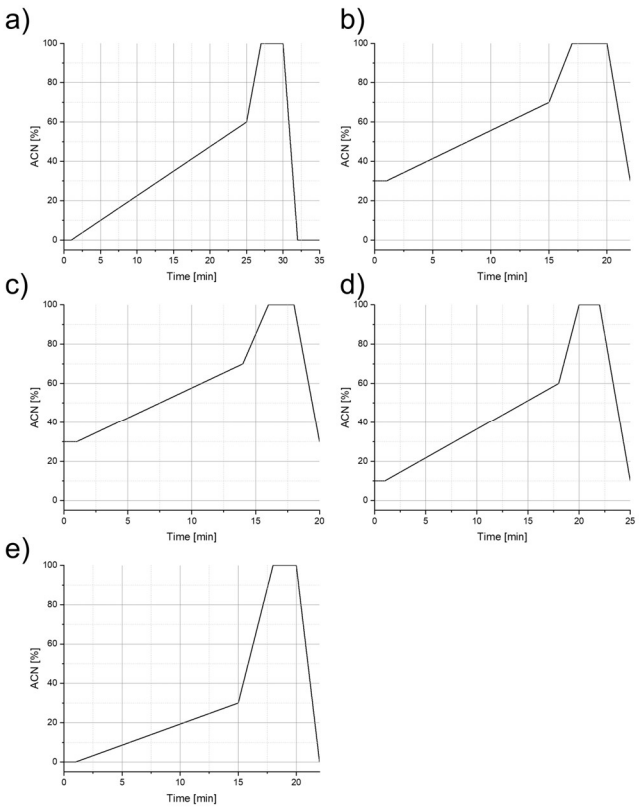

Figure S 1: HPLC methods: (a) Standard method, (b) method used to purify SAP3, (c) method used to purify SAP4, (d) method used to purify BAP2-Fluorescein and (e) method used to purify TSP2. ACN content is given in vol%.

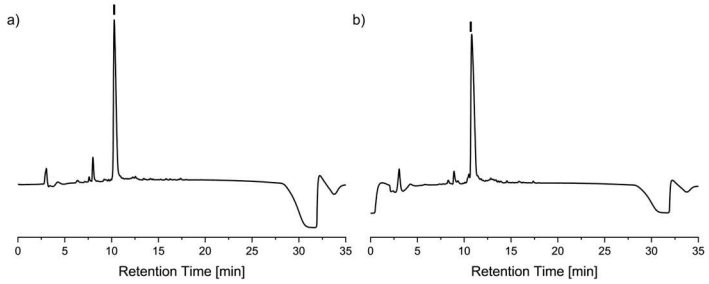

Figure S 2: HPLC chromatogram SAPF1, SAPF2: HPLC chromatograms of (a) SAP1 and (b) SAP2. The retention times correspond to the method depicted in (Figure S 1 a). Product peaks are labelled with I. Detector wavelength: 190 nm.

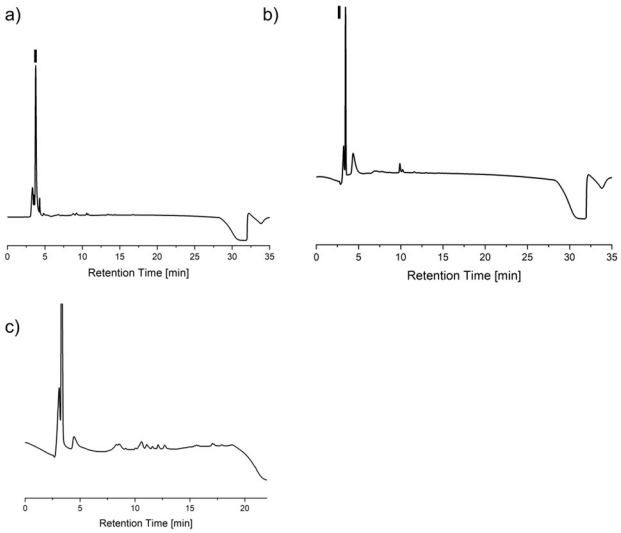

Figure S 3: HPLC chromatogram of TSP1, TSP3, TSP2: HPLC chromatograms of (a) TSP1, (b) TSP3 and (c) TSP2. The retention times correspond to the method depicted in (Figure S 1 a, and Figure S 1 e). Product peaks are labelled with I. Detector wavelength: 190 nm.

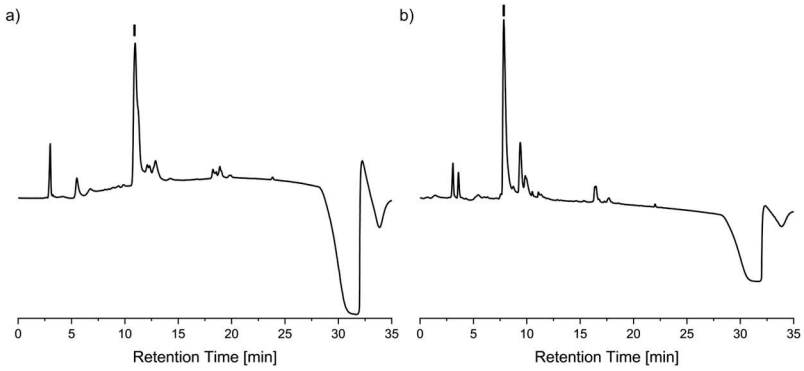

Figure S 4: HPLC chromatogram BAP1 and BAP2: HPLC chromatograms of (a) BAP1 and (b) BAP2. The retention times correspond to the method depicted in (Figure S 1 a). Product peaks are labelled with I. Detector wavelength: 190 nm.

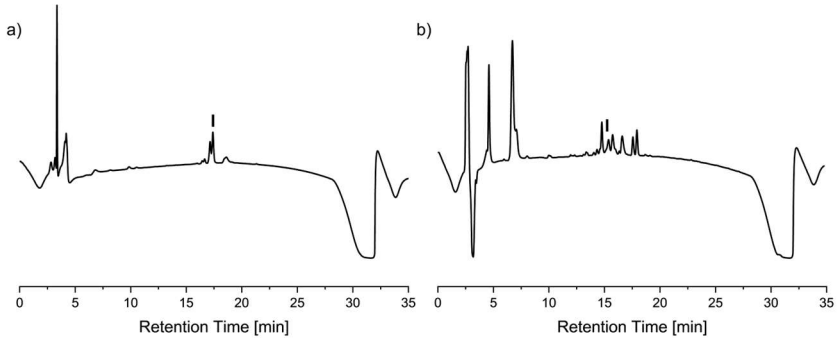

Figure S 5: HPLC chromatogram ABA-Fluorescein, ABA-AEEAc-Fluorescein: HPLC chromatograms of (a) ABA-Fluorescein and (b) ABA-AEEAc-Fluorescein. The retention times correspond to the method depicted in (Figure S 1 a). Product peaks are labelled with I. Detector wavelength: 190 nm.

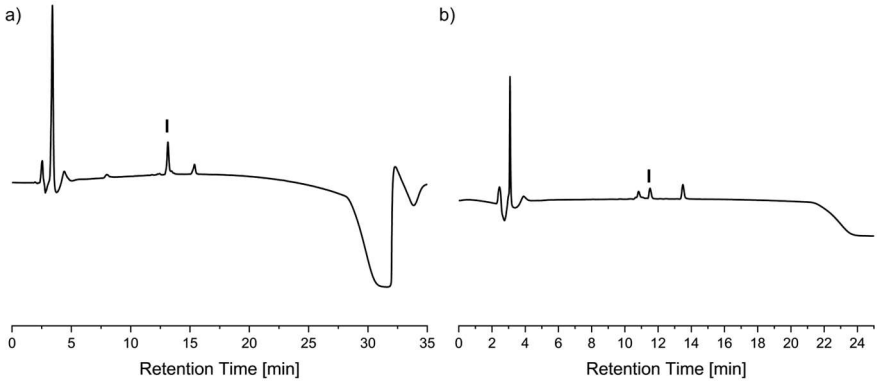

Figure S 6: HPLC chromatogram BAP1-Fluorescein, BAP2-Fluorescein: HPLC chromatograms of (a) BAP1-Fluorescein and (b) BAP2-Fluorescein. The retention times correspond to the method depicted in (Figure S 1 a, Figure S 1 d). Product peaks are labelled with I. Detector wavelength: 190 nm.

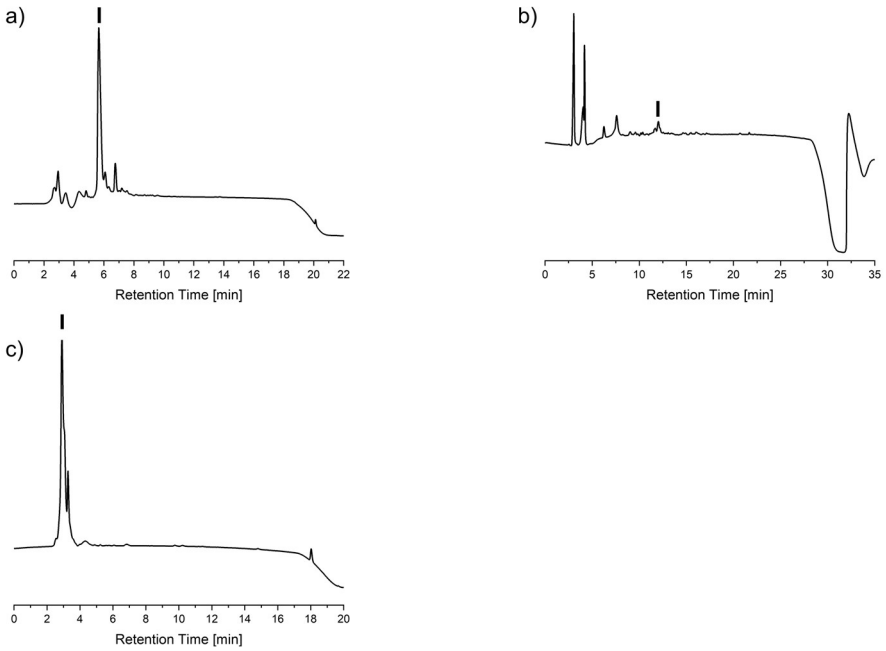

Figure S 7: HPLC chromatogram SAP3, SAP1 and SAP4: HPLC chromatograms of (a) SAP3, (b) SAP1 and (c) SAP4. The retention times correspond to the method depicted in (Figure S 1a, b and c). Product peaks are labelled with I. Detector wavelength: 190 nm.

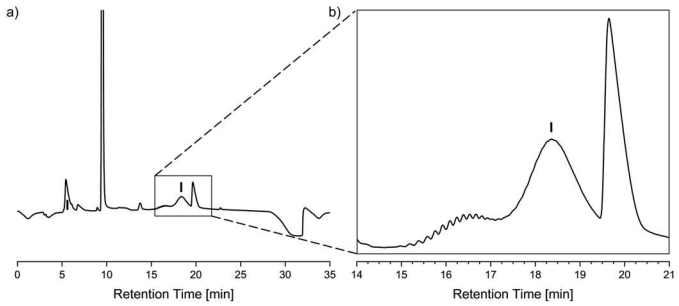

Figure S 8: HPLC chromatogram bisboronic acid cross-linker: (a) Whole spectrum and (b) magnification of the HPLC trace of bisboronic acid cross-linker. The retention time corresponds to the method depicted in (Figure S 1 a). Product peaks are labelled with I. Detector wavelength: 190 nm.

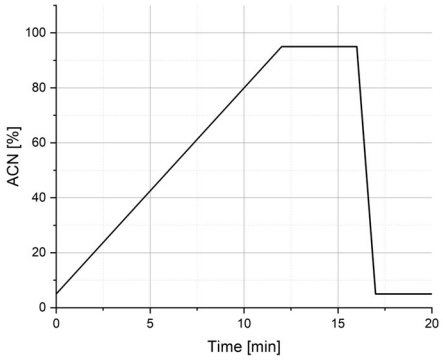

Figure S 9: LCMS method: Standard method utilized for all samples. ACN content is given in vol%.

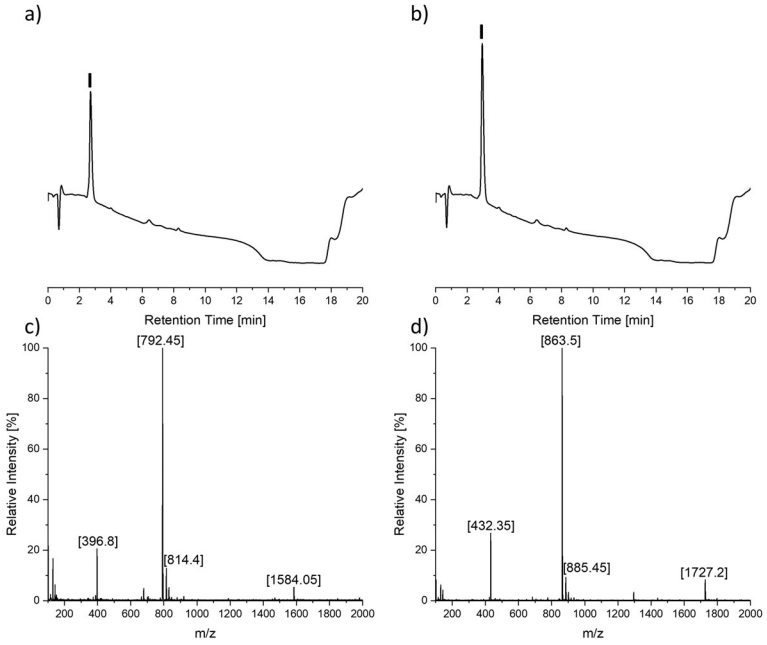

Figure S 10: LCMS of SAPF1 and SAPF2: LC of (a) SAPF1, (b) SAPF2 and their corresponding ESI+ measurements of integrated peaks (I). (c) calc. $[M+H]^+$ = 792.92 m/z; found $[M+H]^+$ 792.45 m/z. Chemical Formula: $C_{32}H_{57}N_9O_{12}S$ (d) calc. $[M+H]^+$ = 864.00 m/z, found $[M+H]^+$ = 863.5 m/z Chemical Formula: $C_{35}H_{62}N_{10}O_{13}S$. Higher and lower molecular weight peaks correspond to dimers and doubly charged species, respectively. The standard method was used as depicted in Figure S 9, detector wavelength 190 nm, since the standard protocol is calibrated to 214 nm, no blank subtraction was conducted.

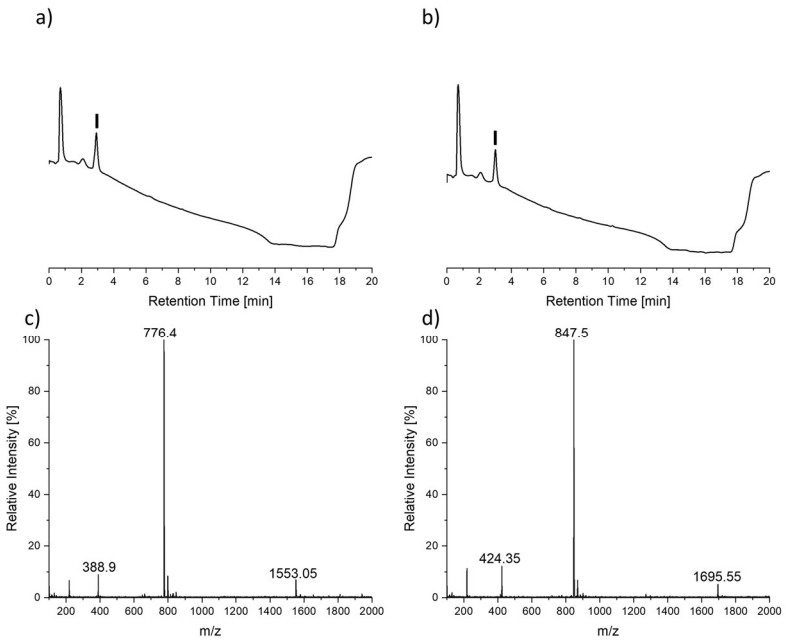

Figure S 11: LCMS of SAPF3 and SAPF4: LC of (a) SAPF3, (b) SAPF4 and their corresponding ESI+ measurements of integrated peaks (I). (c) calc. $[M+H]^+$ = 776.92 m/z; found $[M+H]^+$ = 776.4 m/z. Chemical Formula: $C_{32}H_{57}N_9O_{11}S$. (d) calc. $[M+H]^+$ = 848.0 m/z, found $[M+H]^+$ = 847.5 m/z. Chemical Formula: $C_{35}H_{62}N_{10}O_{12}S$. Higher and lower molecular weight peaks correspond to dimers and doubly charged species, respectively. First peak represents injection peak. The standard method was used as depicted in Figure S 9, detector wavelength 190 nm, since the standard protocol is calibrated to 214 nm, no blank subtraction was conducted.

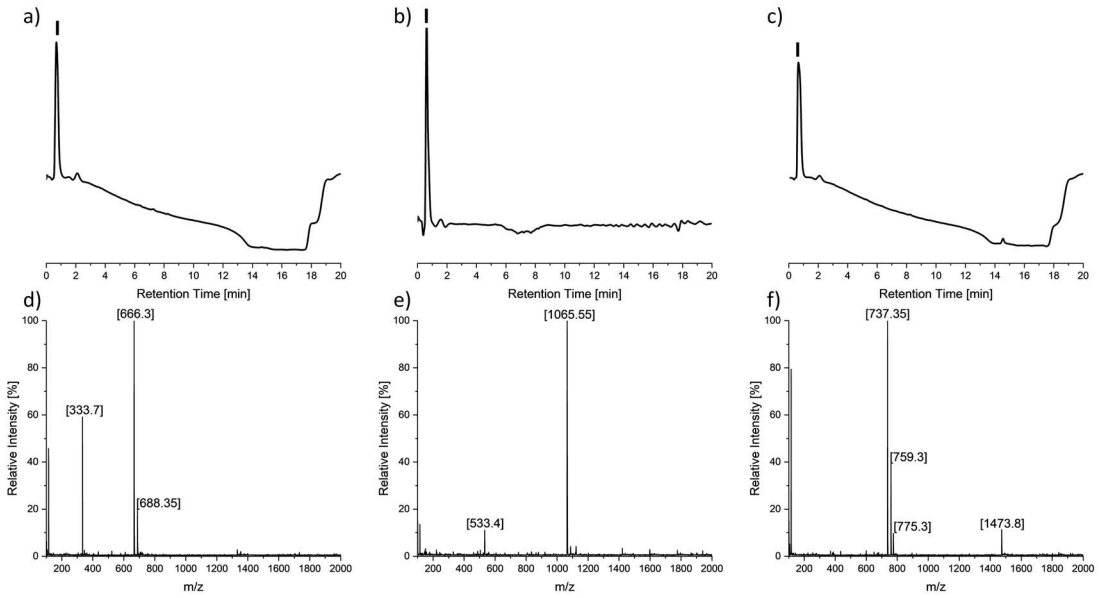

Figure S 12: LCMS of TSP1, TSP3 and TSP2: LC of (a) TSP1, (b) TSP2 and (c) TSP3 and their corresponding ESI+ measurements of integrated peaks (I). (d) calc. $[M+H]^+$= 666.66 m/z; found $[M+H]^+$ = 666.3 m/z. Chemical Formula: $C_{24}H_{43}N_9O_{13}$ (e) calc. $[M+H]^+$ = 1066.02 m/z, found $[M+H]^+$ = 1065.55 m/z. Chemical Formula: $C_{38}H_{64}N_{16}O_{20}$. (f) calc. $[M+H]^+$ = 737.7 m/z, found $[M+H]^+$ = 737.5 m/z. Chemical Formula: $C_{26}H_{44}N_{10}O_{15}$. Higher and lower molecular weight peaks correspond to dimers and doubly charged species, respectively. First peak represents injection peak. The standard method was used as depicted in Figure S 9, detector wavelength 190 nm, since the standard protocol is calibrated to 214 nm, no blank subtraction was conducted.

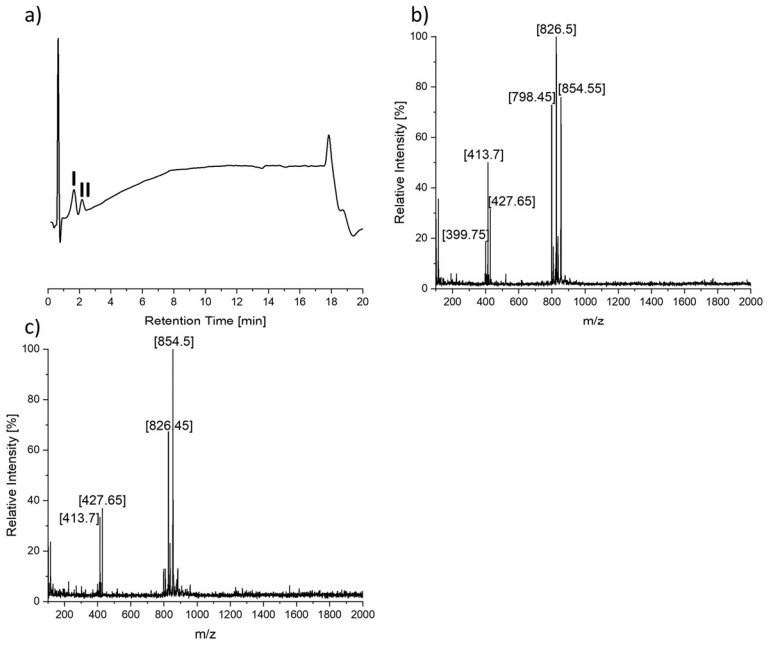

Figure S 13: LCMS of BAP1: LC of BAP1 (a) and its corresponding ESI+ measurement of product peaks. (b) (I) calc. $[M+H]^+$= 854.50 m/z; found $[M+H]^+$= 854.55 m/z, [Dimer - 3 H_2O + $2H]^{2+}$= 827.5 m/z, found [Dimer – 3 H_2O + $2H]^{2+}$= 826.5 m/z, calc. [Dimer- 6 H_2O+ $2H]^{2+}$ = 800.55 m/z, found [Duplex- 6 H_2O $2H]^{2+}$ = 798.45 m/z. Lower molecular weight compounds correspond to doubly charged species (c) (II) calc. $[M+H]^+$= 854.50 m/z; found $[M+H]^+$= 854.50 m/z, calc. [Dimer –$3H_2O$+$2H]^{2+}$= 827.5 m/z, found [Dimer-$3H_2O$+$2H]^{2+}$. Chemical formula $C_{37}H_{53}B_2N_9O_{13}$. The standard method was used as depicted in Figure S 9, detector wavelength 214 nm.

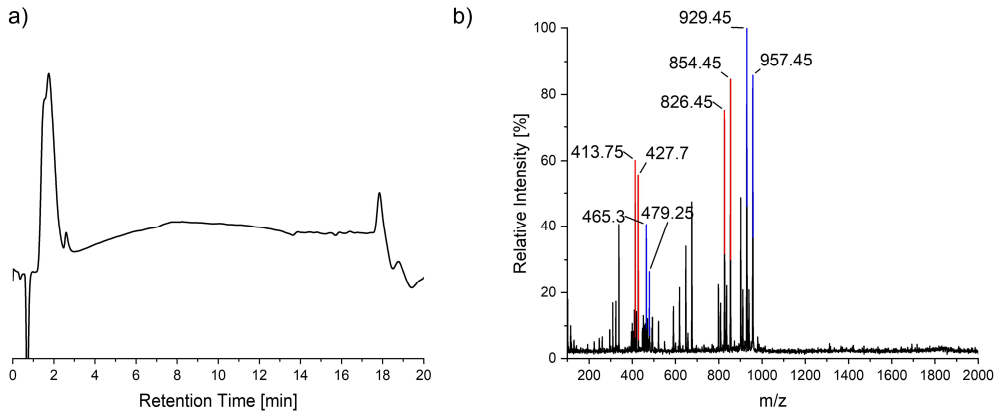

Figure S 14: LCMS of Cys-BAP1 mixture: LC of BAP1 mixture (a) and its corresponding ESI+ measurement of product peaks. Peaks that correspond to BAP1 and BAP1-cystein are colour coded in blue and red, respectively. (b) calc. $[M+H]^+$= 957.64 m/z; found $[M+H]^+$= 957.45 m/z, [Dimer-$3H_2O$+$2H]^{2+}$ = 930.64 m/z found [Duplex-3-H_2O+$2H]^{2+}$ = 929.45 m/z. [M-Cys+H]$^+$= 854.50 m/z; found $[M+H]^+$= 854.45 m/z. Chemical formula Cys-BAP1 $C_{40}H_{58}B_2N_{10}O_{14}S$. Chemical formula BAP1 $C_{37}H_{53}B_2N_9O_{13}$. Labelled lower molecular weight peaks represent doubly charged products. The standard method was used as depicted in Figure S 9, detector wavelength 214 nm.

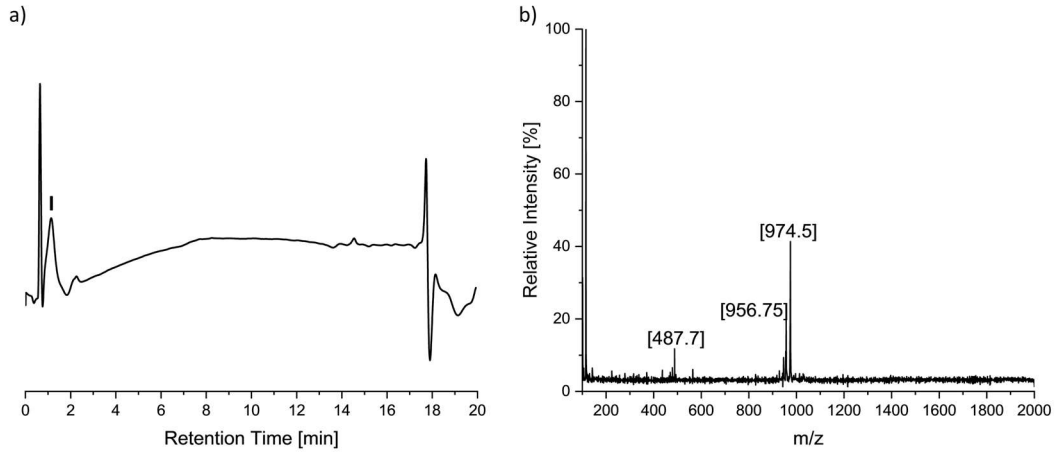

Figure S 15: LCMS of Cys-BAP2: LC of BAP2 (a) and its corresponding ESI+ measurement of the product peak (I). (b) (I) calc. $[M+H]^+$= 974.64 m/z; found $[M+H]^+$ = 974.5 m/z. Lower molecular weight peaks correspond to the dehydration product and doubly charged species. Chemical formula $C_{39}H_{57}B_2N_{11}O_{14}S$. Standard method was used as depicted in Figure S 9, detector wavelength 214 nm. First peak represents injection peak.

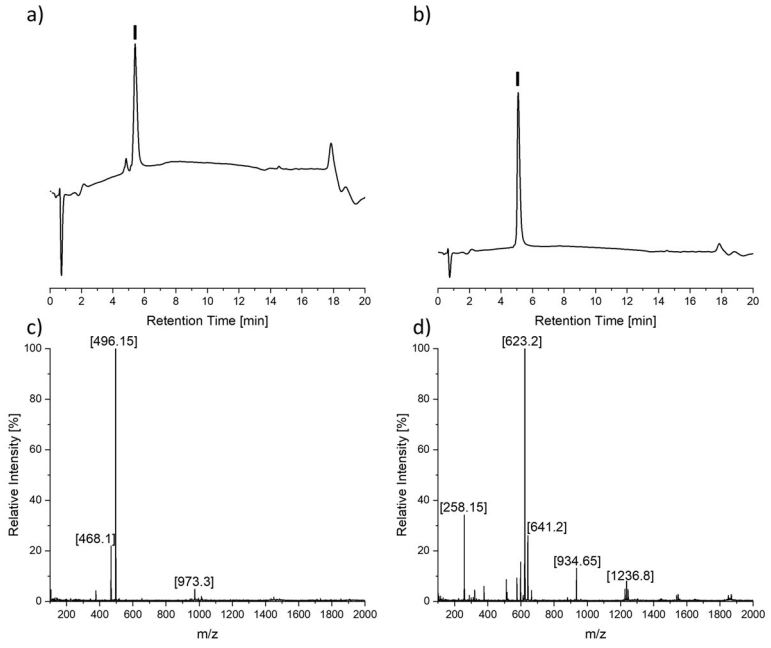

Figure S 16: LCMS of ABA-Fluorescein and ABA-AEEAc-Fluorescein: LC of ABA-Fluorescein (a) and ABA-AEEAc-Fluorescein (b) and their corresponding ESI+ measurements of product peaks (I). (c) calc. $[M+H]^+$= 496.25 m/z; found $[M+H]^+$= 496.15 m/z. Chemical formula $C_{39}H_{57}B_2N_{11}O_{14}S$. (d) calc. $[M-H_2O+H]^+$= 623.41 m/z; found $[M-H_2O+H]^+$= 623.2 m/z. Chemical formula $C_{39}H_{57}B_2N_{11}O_{14}S$. Standard method was used as depicited in Figure S 9, detector wavelength 214 nm.

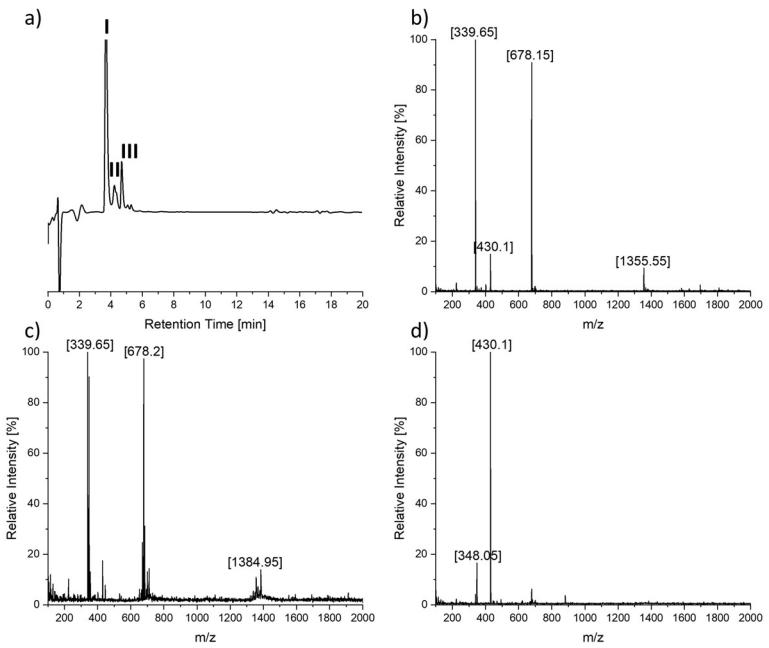

Figure S 17: LCMS of BAP1-Fluorescein: LC of BAP1-Fluorescein (a) and its corresponding ESI+ measurements of integrated peaks (I, II, III). (b) (I) calc. $[Dimer\text{-}3H_2O+2H]^{2+}$ = 678.76 m/z; found 678.15 m/z. Chemical formula $C_{64}H_{71}B_2N_{11}O_{21}S$. (c) (II) calc. $[Dimer\text{-}3H_2O+2H]^{2+}$= 678.76 m/z; found 678.20 m/z. Chemical formula $C_{64}H_{71}B_2N_{11}O_{21}S$. (d) (III) Fluorescein-Maleimide calc. $[M+H]^+$ = 428.37 m/z, found $[M+H]^+$ = 430.10 m/z. Chemical formula $C_{40}H_{58}B_2N_{10}O_{14}S$. Standard method was used as depicted in Figure S 9, detector wavelength 214 nm.

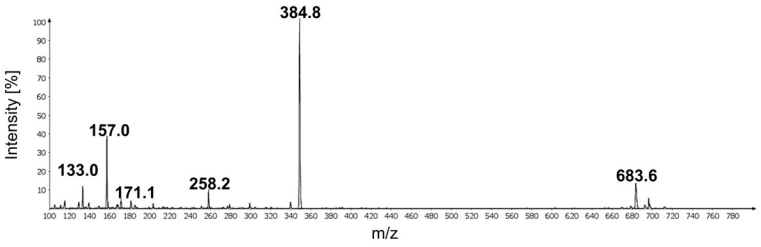

Figure S 18: ESI-MS of BAP2-Fluorescein: ESI+ measurement of BAP2-Fluorescein. calc. $[M\text{-}H_2O+2H]^{2+}$= 683 m/z; found $[M\text{-}H_2O+2H]^{2+}$= 683.6 m/z. 384.8 m/z signal corresponds to doubly charged species. Chemical formula $C_{63}H_{70}B_2N_{12}O_{22}S$.

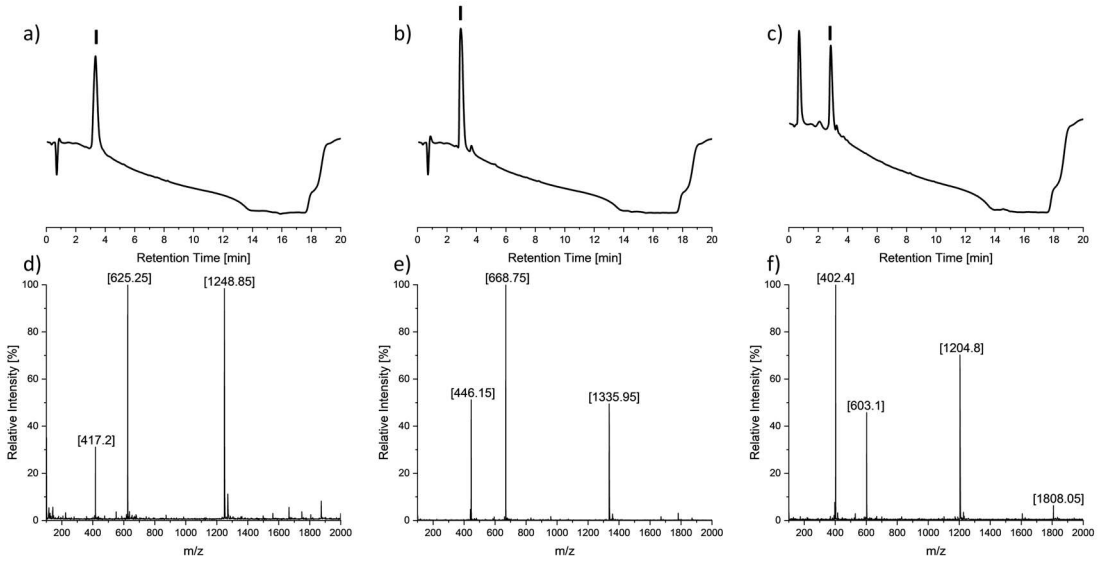

Figure S 19: LCMS SAP1, SAP3 and SAP4: LC of (a) SAP1, (b) SAP3, (c) SAP4 and their corresponding ESI+ measurements of integrated peaks (I). (d) calc. $[M+H]^+$ = 1249.55 m/z; found $[M+H]^+$ = 1248.85 m/z. Chemical formula $C_{53}H_{97}N_{15}O_{15}S_2$. (e) calc. $[M+H]^+$ = 1336.63 m/z; found $[M+H]^+$ = 1335.95 m/z. Chemical formula $C_{56}H_{71}B_2N_{11}O_{21}S_2$. (f) $[M+H]^+$ = 1205.5 m/z, found $[M+H]^+$ = 1204.8 m/z. Chemical formula $C_{51}H_{93}N_{15}O_{14}S_2$. Higher and lower molecular weight peaks correspond to dimers and doubly charged species, respectively. First peak represents injection peak. The standard method was used as depicted in Figure S 9, detector wavelength 190 nm, since the standard protocol is calibrated to 214 nm, no blank subtraction was conducted.

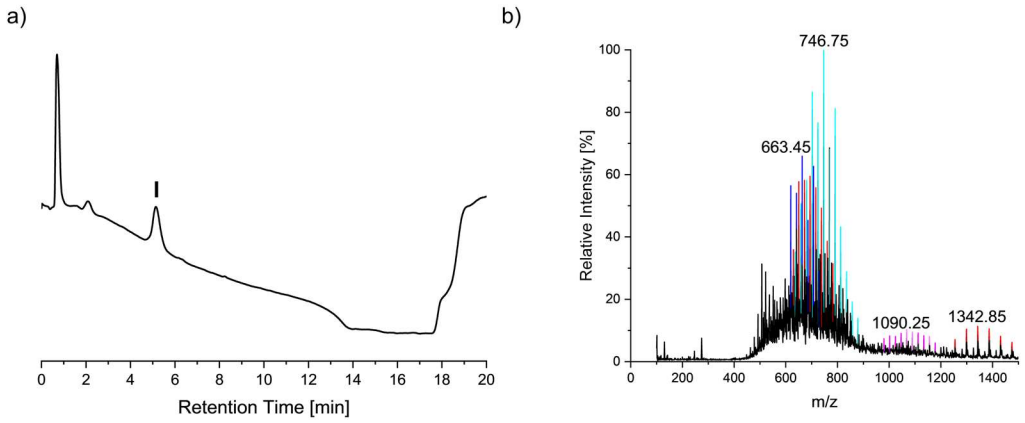

Figure S 20: LCMS of bisboronic acid cross-linker: LC of bisboronic acid cross-linker (a) and its corresponding ESI+ measurement of product peaks (b). Bifunctional signals are depicted in bue, light blue and red. Monofunctional signals in purple. (I) calc. $[Dimer_{25\ repeats}\text{-}6H_2O+2H]^{2+}$= 746.64 m/z; found $[Duplex_{25\ repeats}\text{-}6H_2O+H]^{2+}$ = 746.75 m/z, calc $[M_{22repeats}+2H]^{2+}$ = 663.55 m/z, found $[M_{22repeats}+2H]^{2+}$ = 663.45 m/z, calc. $[M_{22\ repeats}+OH^-+H]^+$ = 1343.11 m/z, found $[M_{22\ repeats}+OH^-+H]^+$ = 1342.85 m/z. Chemical formula 22 repeats bifunctional: $C_{60}H_{106}B_2N_2O_{28}$. The standard method was used as depicted in Figure S 9, detector wavelength 214 nm.

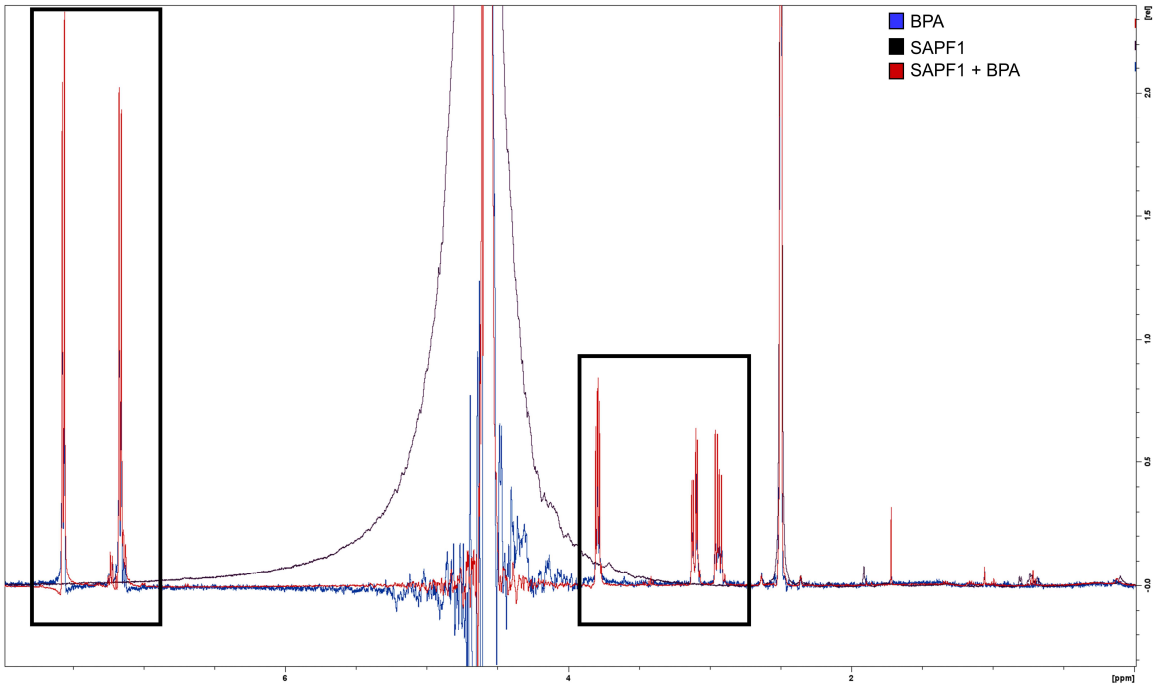

Figure S 21: ^{1}H NMR of SAPF1 with PBA: Magnified regions of interest are framed in black and correspond to the regions in Figure 16. Measurements were conducted in DMSO-d_6 : ABC buffer pH 7.4 10 mM 1:9 at 500 MHz using water suppression at 298 K. ^{1}H NMR spectra were calibrated to the DMSO-d_6 signal (δ = 2.50 ppm).

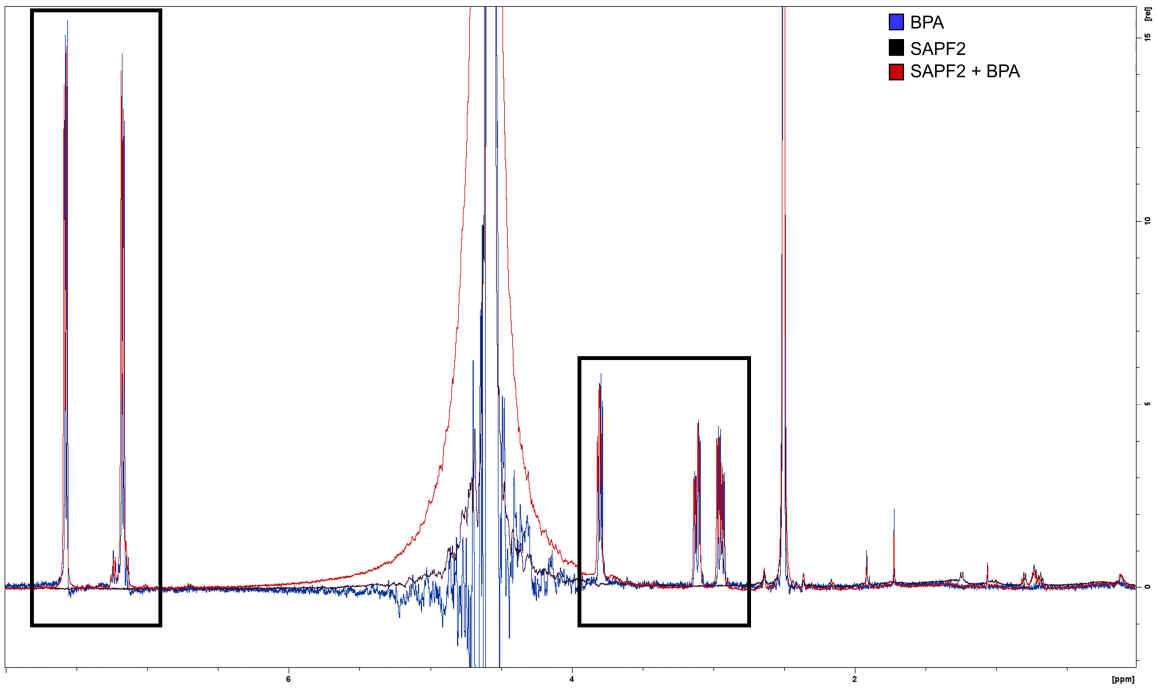

Figure S 22: ^{1}H NMR of SAPF2 with PBA: Magnified regions of interest are framed in black and correspond to the regions in Figure 16. Measurements were conducted in DMSO-d_6 : ABC buffer pH 7.4 10 mM 1:9 at 500 MHz using water suppression at 298 K. ^{1}H NMR spectra were calibrated to the DMSO-d_6 signal (δ = 2.50 ppm).

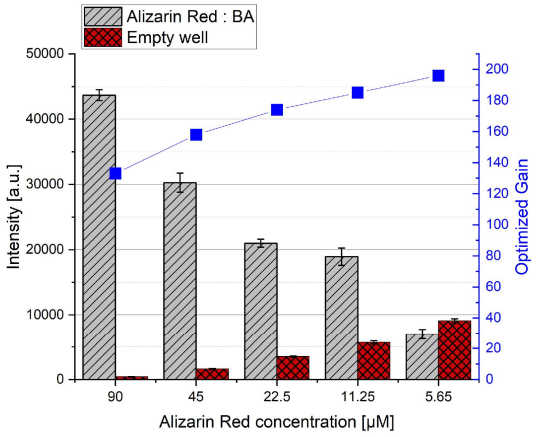

Figure S 23: Calibration curve ARS:4CPBA: ARS-4CPBA (1:1 molar ratio) complexes of different concentration were titrated and a concentration of 22 µM ARS was chosen for displacement assays.

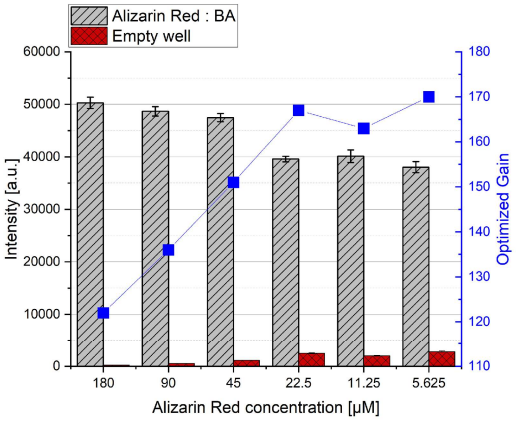

Figure S 24: Calibration curve ARS:BAP1: ARS-BAP1 (2:1 molar ratio) complexes of different concentration were titrated and a concentration of 45s µM ARS was chosen for displacement assays.

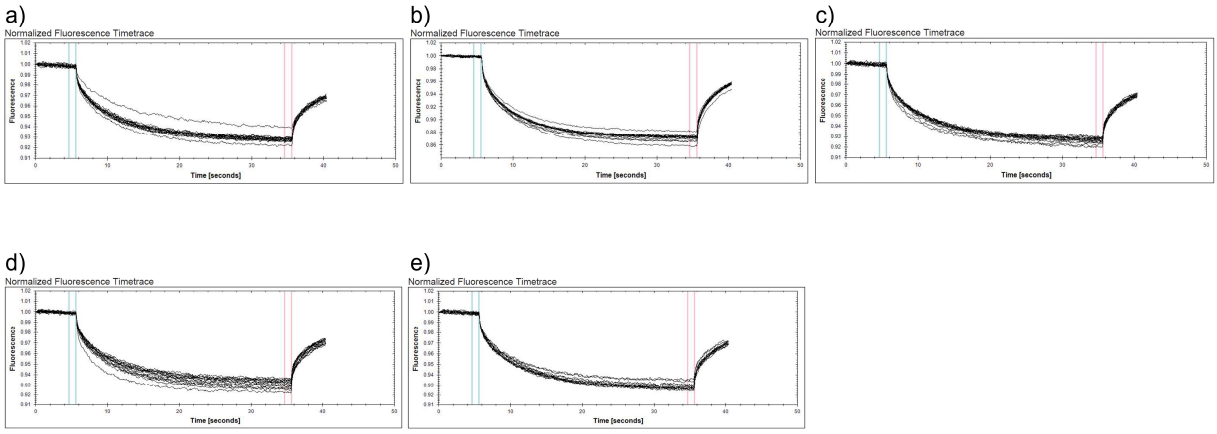

Figure S 25: Fluorescence decays of ABA-Fluorescein MST measurements: Fluorescence decays of (a) SAPF1, (b) SAPF2, (c) SAPF3, (d) SAPF4 and (e) Fructose. Measurements were carried out in 10 vol% DMSO, 10 mM ABC buffer pH 7.4.

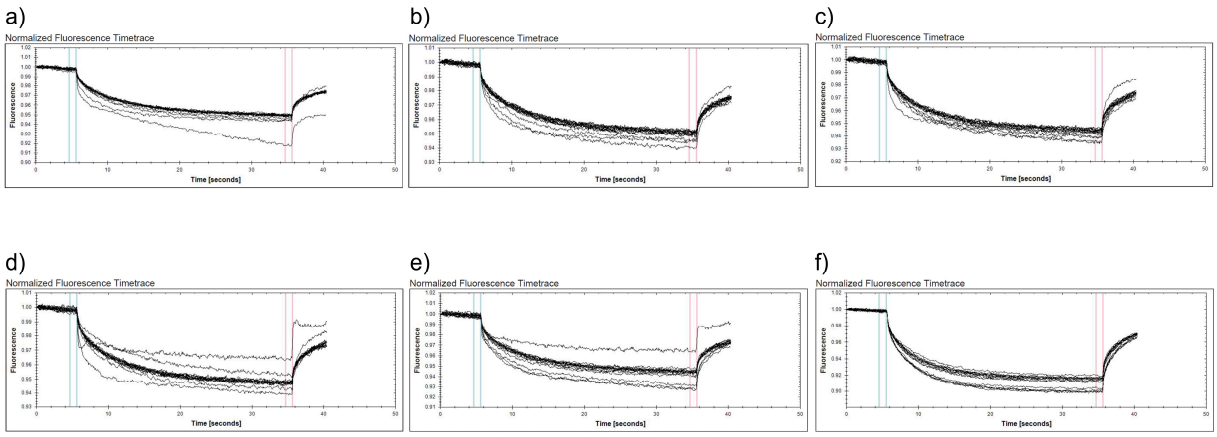

Figure S 26: Fluorescence decays of ABA-AEEAc-Fluorescein MST measurements: Fluorescence decays of (a) SAPF1, (b) SAPF2, (c) SAPF3, (d) SAPF4, (e) SAPF5 and (f) Fructose. Measurements were carried out in 10 vol% DMSO, 10 mM ABC buffer pH 7.4.

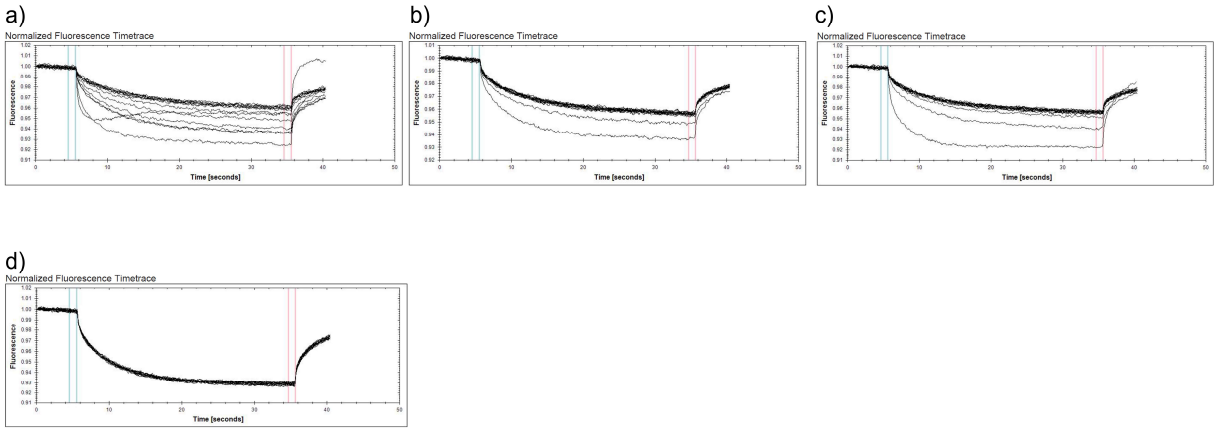

Figure S 27: Fluorescence decays of BAP1-Fluorescein MST measurements: Fluorescence days of (a) TSP3, (b) TSP1, (c) TSP2 and (d) Fructose. Measurements were carried out in 10 vol% DMSO, 10 mM ABC buffer pH 7.4.

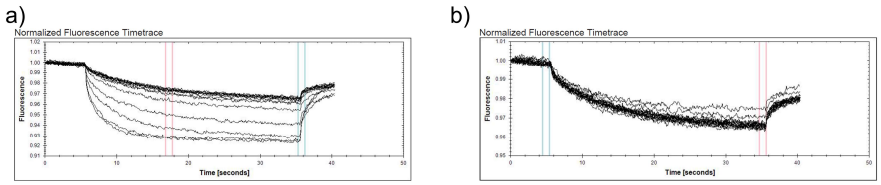

Figure S 28: Fluorescence decays of BAP2-Fluorescein MST measurements: Fluorescence days of (a)TSP2 and (d) Fructose. Measurements were carried out in 10 vol% DMSO, 10 mM ABC buffer pH 7.4.

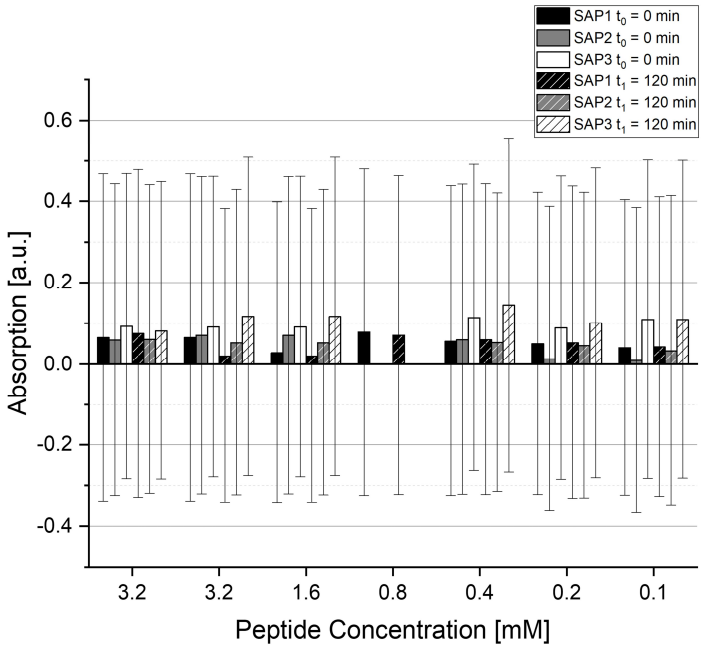

Figure S 29: Absorption measurements of SAPs with ABA-AEEAc-Fluorescein at 600 m: Absorption before and after 2 hours of incubation with 25 µM of ABA-AEEAc-Fluorescein. Error bars are standard deviations which were corrected for error propargation.

Table S 1: Diboronic acid tetraserine complexes tested for energy minimization with the force fields UFF, MM2 and MMFF94. Numbers correspond to data points in (Figure 27).

1	KKBGPBKK	KSSGPSSK
2	KKBGPBKK	KSSKKSSK
3	KKBGPBKK	KSSGGSSK
4	KKBGGBKK	KSSGPSSK
5	KKBGGBKK	KSSKKSSK
6	KKBGGBKK	KSSGGSSK
7	KKBKBKK	KSSKSSK
8	KKBKBKK	KSSPSSK
9	KKBGPBKK	KSSGGGSSK
10	KKBGGGBKK	KSSGGSSK
11	KKBGGGBKK	KSSGGGSSK
12	KKBGGBKK	KSSGGSSK
13	KKBBKK	KKSSSSKK
14	KKBGBKK	KKSSSSKK
15	KKBGGBKK	KKSSSSKK
16	KKBPBKK	KKSSSSKK
17	KKBPGKK	KKSSSSKK
18	KKBGGGBKK	KSGGSGGGSGGSK

19	GGBGPBGG	GSSGGSSG
20	BGPB	SSGGSS
21	GGBGGGBGG	GSGGSGGGSGGSG
22	GGBGPBGK	GSSGGSSG
23	GGBGPBGK	GSSGGSSK
24	GGBGGGBGK	GSGGGSGGGSGGGSK

Table S 2: XYZ coordinates of SGS-4CPBA optimized structure.

	x	y	z
N	1.056760491	4.540566155	-0.939865352
C	2.155254848	3.631358869	-0.613559343
C	2.532006831	3.630841178	0.87983653
O	2.654000765	4.691177027	1.50717418
H	1.863485827	2.616780842	-0.915397081
C	3.385553716	4.055025459	-1.442253002
H	3.155177455	3.918707868	-2.505332115
H	3.610500121	5.113262589	-1.257647757
O	4.506735585	3.224724298	-1.113922181
H	1.213077071	5.439340497	-0.483683566
H	0.182346375	4.177430437	-0.565565139
N	2.747660371	2.411247411	1.429661038
C	3.371847542	2.202047217	2.733830275
C	4.745053054	1.56185592	2.502434837
O	4.838239353	0.357522015	2.242529661
H	3.437975089	3.170001774	3.238769093
H	2.768254387	1.5130296	3.336426035
H	2.63885341	1.598194956	0.83605804
N	5.809657179	2.405194775	2.527399941
C	7.123400875	2.005439195	2.064142203
C	8.179158925	2.199623931	3.156428644
O	8.057924852	2.979047016	4.077632567
H	7.054819882	0.940876209	1.810236022
C	7.539572608	2.791974454	0.790693283
H	8.470098493	2.371309157	0.390485542
H	7.703033844	3.849178998	1.037124773
O	6.512951789	2.638882389	-0.182805201
H	5.658286925	3.376913634	2.770092404
O	9.313201845	1.481901753	3.036810177
H	9.276328039	0.846354913	2.302163621
O	7.149077171	10.06663204	0.831702434
C	6.034141313	7.367525249	0.677889573
C	7.362040577	9.325084067	-0.279239067
C	6.907411319	7.900589737	-0.284758457
C	5.626352484	6.033464724	0.600205714
B	5.674460538	3.666259255	-0.557834964
C	7.368131852	7.069638136	-1.320405477
C	6.087389786	5.188203663	-0.426075087

H	6.761483773	9.545332769	1.551823547
C	6.97192851	5.734218545	-1.380213016
O	7.915587982	9.855005043	-1.227533761
H	5.633818443	7.979069093	1.487912662
H	4.930194179	5.654679393	1.347397078
H	8.042623314	7.477316584	-2.071697227
H	7.358421213	5.11028117	-2.187522082

Table S 3: XYZ coordinates of SAS-4CPBA optimized structure

	x	y	z
N	0.159909988	2.937554385	-1.641706648
C	1.494839481	2.646826429	-1.10981234
C	1.542575426	2.579643492	0.426257477
O	1.205446759	3.550050112	1.117746892
H	1.824851746	1.687945678	-1.530350095
C	2.44076897	3.758745977	-1.586323637
H	2.540423387	3.701255861	-2.676947649
H	2.014832696	4.731098381	-1.312200296
O	3.736799283	3.590969529	-0.986618348
H	-0.248360123	3.724946821	-1.138349524
H	-0.458125108	2.143320492	-1.488467446
N	1.979695085	1.406790281	0.947108672
C	2.371320546	1.224317861	2.350168426
C	3.9129079	1.239879206	2.339097133
O	4.575076178	0.212415312	2.160354606
H	2.266184091	0.683301011	0.297916979
H	1.995870447	2.097844636	2.893278605
C	1.797143416	-0.058643506	2.941142067
H	0.701096246	-0.013564817	2.924070399
H	2.127564999	-0.936287037	2.371522634
H	2.129142802	-0.174590575	3.981331294
N	4.473064862	2.471795533	2.43427982
C	5.864050215	2.710352698	2.099454218
C	6.410961966	3.846002742	2.964846898
O	5.716133326	4.566119581	3.649947929
H	6.429057414	1.795200084	2.325194524
C	6.056324942	3.00504931	0.593601743
H	5.519574078	2.243014897	0.018458378
H	7.12227948	2.955930924	0.337611434
O	5.601354618	4.322614576	0.274733828
H	3.880198372	3.276943665	2.593950879
O	7.741871908	4.044691168	2.928634185
H	8.201815839	3.380699365	2.388951703
O	3.242234638	10.96825087	-2.266027991
C	3.625436101	8.074751136	-2.074871228
C	3.581205174	10.42722946	-1.074116205
C	3.787936756	8.947485066	-0.985773219
C	3.821551981	6.701254791	-1.913250975

B	4.485706898	4.613225807	-0.474761945
C	4.165797207	8.416056164	0.260012002
C	4.201449821	6.154979305	-0.671944621
H	3.169285161	10.30398747	-2.96870609
C	4.378913151	7.046586548	0.40641365
O	3.703409677	11.17646481	-0.119889107
H	3.341332988	8.435300299	-3.064182211
H	3.686665336	6.056222046	-2.781413089
H	4.296224229	9.087294553	1.106988362
H	4.686909649	6.663307611	1.379207925

Table S 4: XYZ coordinates of SSA-4CPBA optimized structure.

	x	y	z
N	-0.366117426	0.787705533	0.172371158
C	1.006424809	1.273819199	0.204108128
C	1.94485483	0.534904759	1.170602893
O	1.520061517	0.037191692	2.217384985
H	1.41923526	1.234078477	-0.812953831
C	0.993701584	2.75478948	0.675406542
H	0.567029787	3.380259167	-0.118603814
H	0.36672616	2.839109118	1.573973651
O	2.330565834	3.180744587	0.952302278
H	-0.670191753	0.575542629	1.12275736
H	-0.416251041	-0.086765826	-0.346265104
N	3.26497064	0.607186932	0.832873124
C	4.364898195	0.763112178	1.787835036
C	4.983795305	-0.593683004	2.195503632
O	4.375460535	-1.663085417	2.118472259
H	5.144173065	1.318494109	1.249335661
C	3.999259028	1.589109489	3.04116232
H	3.096559628	1.184161987	3.508057423
H	4.824647372	1.511128854	3.755794602
O	3.821453979	3.003473949	2.836465613
H	3.438137111	1.084024693	-0.042429767
N	6.263954345	-0.521352341	2.636590994
C	6.989523105	-1.696177514	3.082700148
C	6.466077239	-2.189613911	4.441006878
O	5.932864905	-1.482721458	5.270036885
H	6.726493726	0.377195576	2.698569158
H	6.825722034	-2.49781883	2.349190409
C	8.491248088	-1.388147532	3.181616191
H	8.867912231	-1.089179595	2.195703811
H	8.672802707	-0.575838755	3.89835169
H	9.042112156	-2.277295202	3.510369754
O	6.670729725	-3.494373837	4.716700776
H	7.06619111	-3.967035214	3.965298605
O	2.173415044	9.730290426	4.923610456
C	2.712447903	6.938236503	4.257573651

C	1.574895508	9.185885203	3.840538463
C	1.94571855	7.791204588	3.443880369
C	3.007774957	5.642100506	3.832003212
B	2.882875954	3.688344349	2.106802069
C	1.484785253	7.320590384	2.202086125
C	2.557807713	5.15620878	2.588046311
H	2.842749396	9.142434873	5.307200286
C	1.791579539	6.02601379	1.784888018
O	0.756650274	9.857844112	3.236246588
H	3.07445815	7.254817032	5.237015771
H	3.597049732	4.995002865	4.481048195
H	0.891345535	7.97927561	1.570337018
H	1.430200703	5.687707003	0.813694019

Table S 5: XYZ coordinates of SSA-4CPBA optimized structure.

	x	y	z
N	-0.143019476	0.321749795	-0.538955141
C	0.658643431	1.323173861	0.162241224
C	1.814970987	0.730143184	0.976421104
O	1.729798899	-0.376690447	1.514035849
H	1.044456563	2.043768482	-0.571309097
C	-0.282690248	2.082359027	1.138452888
H	-1.146784799	2.423561476	0.559356374
H	-0.624259982	1.39886392	1.927261431
O	0.30487437	3.261391913	1.716059243
H	0.382885105	-0.042273382	-1.331359756
H	-0.299601689	-0.473823285	0.080265681
N	2.884632686	1.55661326	1.159647452
C	3.684152287	1.526598111	2.373353398
C	4.738948968	0.401119164	2.363892921
O	5.070106547	-0.183646773	1.329280517
H	4.2575625	2.463411877	2.368451652
C	2.773288975	1.525219495	3.657701177
H	2.625390774	0.506558004	4.027509824
H	3.26505406	2.119258583	4.439159714
O	1.469362835	2.028232952	3.371892486
H	2.900058724	2.418479385	0.629812787
N	5.317198514	0.139519122	3.558010847
C	6.377273422	-0.837517416	3.694446397
C	6.850477669	-0.884795774	5.134003959
O	6.387815377	-0.197274293	6.022261194
H	6.033524301	-1.842178987	3.402551509
H	7.233957806	-0.590104088	3.047894778
H	5.067152537	0.651884116	4.396300148
O	7.842309468	-1.750342176	5.405480301
H	8.128588603	-2.237236428	4.613777226
O	3.886733002	8.672934242	5.595803648
C	2.804418918	6.052948101	4.90045596

C	3.534073673	8.43002444	4.31380439
C	2.957414511	7.092448231	3.967721614
C	2.265223016	4.827135257	4.504565402
B	1.205656241	3.23056122	2.747660596
C	2.551295894	6.881555861	2.637762367
C	1.848881309	4.603029542	3.177577617
H	3.711452719	7.916543576	6.176761373
C	2.00006458	5.659894128	2.255878245
O	3.701832555	9.316788211	3.494226246
H	3.098711115	6.168600006	5.944431781
H	2.152928369	4.04256928	5.252705785
H	2.667338395	7.685828209	1.913370408
H	1.682416488	5.523597017	1.22209648

7 References

1 Mendes, A. C., Baran, E. T., Reis, R. L. and Azevedo, H. S. (2013) Self-assembly in nature: using the principles of nature to create complex nanobiomaterials. Wiley interdisciplinary reviews. Nanomedicine and nanobiotechnology **5**, 582–612

2 O'Leary, L. E. R., Fallas, J. A., Bakota, E. L., Kang, M. K. and Hartgerink, J. D. (2011) Multi-hierarchical self-assembly of a collagen mimetic peptide from triple helix to nanofibre and hydrogel. Nature chemistry **3**, 821–828

3 Prahl, L. S., Castle, B. T., Gardner, M. K. and Odde, D. J. (2014) Quantitative analysis of microtubule self-assembly kinetics and tip structure. Methods in enzymology **540**, 35–52

4 Fritzsche, M. (2017) Self-organizing actin patterns shape cytoskeletal cortex organization. Communicative & integrative biology **10**, e1303591

5 Jisna, V. A. and Jayaraj, P. B. (2021) Protein Structure Prediction: Conventional and Deep Learning Perspectives. The protein journal **40**, 522–544

6 Merrifield, R. B. (1963) Solid Phase Peptide Synthesis. I. The Synthesis of a Tetrapeptide. J. Am. Chem. Soc. **85**, 2149–2154

7 Münzker, L., Oddo, A. and Hansen, P. R. (2017) Chemical Synthesis of Antimicrobial Peptides. Methods in molecular biology (Clifton, N.J.) **1548**, 35–49

8 Stupp, S. I., Zha, R. H., Palmer, L. C., Cui, H. and Bitton, R. (2013) Self-assembly of biomolecular soft matter. Faraday discussions **166**, 9–30

9 Liu, R. and Hudalla, G. A. (2019) Using Self-Assembling Peptides to Integrate Biomolecules into Functional Supramolecular Biomaterials. Molecules (Basel, Switzerland) **24**

10 Bemporad, F., Taddei, N., Stefani, M. and Chiti, F. (2006) Assessing the role of aromatic residues in the amyloid aggregation of human muscle acylphosphatase. Protein Science : A Publication of the Protein Society **15**, 862–870

11 Aggeli, A., Nyrkova, I. A., Bell, M., Harding, R., Carrick, L., McLeish, T. C., Semenov, A. N. and Boden, N. (2001) Hierarchical self-assembly of chiral rod-like molecules as a model for peptide beta -sheet tapes, ribbons, fibrils, and fibers. Proceedings of the National Academy of Sciences of the United States of America **98**, 11857–11862

12 La Manna, S., Di Natale, C., Onesto, V. and Marasco, D. (2021) Self-Assembling Peptides: From Design to Biomedical Applications. International journal of molecular sciences **22**

13 Wiley Online Library (2022) Nanostructured Hydrogels for Three-Dimensional Cell Culture Through Self-Assembly of Fluorenylmethoxycarbonyl–Dipeptides. https://onlinelibrary.wiley.com/doi/10.1002/adma.200501522

14 Álvarez, Z., Kolberg-Edelbrock, A. N., Sasselli, I. R., Ortega, J. A., Qiu, R., Syrgiannis, Z., Mirau, P. A., Chen, F., Chin, S. M. and Weigand, S. et al. (2021) Bioactive scaffolds with enhanced supramolecular motion promote recovery from spinal cord injury. Science (New York, N.Y.) **374**, 848–856

15 Gelain, F., Unsworth, L. D. and Zhang, S. (2010) Slow and sustained release of active cytokines from self-assembling peptide scaffolds. Journal of controlled release : official journal of the Controlled Release Society **145**, 231–239

16 Reches, M. and Gazit, E. (2004) Formation of Closed-Cage Nanostructures by Self-Assembly of Aromatic Dipeptides. Nano Lett. **4**, 581–585

17 Adler-Abramovich, L., Reches, M., Sedman, V. L., Allen, S., Tendler, S. J. B. and Gazit, E. (2006) Thermal and chemical stability of diphenylalanine peptide nanotubes: implications for nanotechnological applications. Langmuir : the ACS journal of surfaces and colloids **22**, 1313–1320

18 Reches, M. and Gazit, E. (2005) Self-assembly of peptide nanotubes and amyloid-like structures by charged-termini-capped diphenylalanine peptide analogues. Isr. J. Chem. **45**, 363–371

19 Diaferia, C., Morelli, G. and Accardo, A. (2019) Fmoc-diphenylalanine as a suitable building block for the preparation of hybrid materials and their potential applications. Journal of materials chemistry. B **7**, 5142–5155

20 Woolfson, D. N. (2010) Building fibrous biomaterials from alpha-helical and collagen-like coiled-coil peptides. Biopolymers **94**, 118–127

21 Zimenkov, Y., Conticello, V. P., Guo, L. and Thiyagarajan, P. (2004) Rational design of a nanoscale helical scaffold derived from self-assembly of a dimeric coiled coil motif. Tetrahedron **60**, 7237–7246

22 Rele, S., Song, Y., Apkarian, R. P., Qu, Z., Conticello, V. P. and Chaikof, E. L. (2007) D-periodic collagen-mimetic microfibers. J. Am. Chem. Soc. **129**, 14780–14787

23 Schneider, J. P., Pochan, D. J., Ozbas, B., Rajagopal, K., Pakstis, L. and Kretsinger, J. (2002) Responsive hydrogels from the intramolecular folding and self-assembly of a designed peptide. J. Am. Chem. Soc. **124**, 15030–15037

24 Salick, D. A., Kretsinger, J. K., Pochan, D. J. and Schneider, J. P. (2007) Inherent antibacterial activity of a peptide-based beta-hairpin hydrogel. J. Am. Chem. Soc. **129**, 14793–14799

25 Zhang, S., Holmes, T., Lockshin, C. and Rich, A. (1993) Spontaneous assembly of a self-complementary oligopeptide to form a stable macroscopic membrane. Proceedings of the National Academy of Sciences of the United States of America **90**, 3334–3338

26 Nagai, Y., Unsworth, L. D., Koutsopoulos, S. and Zhang, S. (2006) Slow release of molecules in self-assembling peptide nanofiber scaffold. Journal of controlled release : official journal of the Controlled Release Society **115**, 18–25

27 Wang, J., Han, S., Meng, G., Xu, H., Xia, D., Zhao, X., Schweins, R. and Lu, J. R. (2009) Dynamic self-assembly of surfactant-like peptides A6K and A9K. Soft Matter **5**, 3870

28 Israelachvili, J. N. (2015) Intermolecular and Surface Forces, Elsevier Science, Saint Louis

29 Schilling, C., Mack, T., Lickfett, S., Sieste, S., Ruggeri, F. S., Sneideris, T., Dutta, A., Bereau, T., Naraghi, R. and Sinske, D. et al. (2019) Sequence-Optimized Peptide Nanofibers as Growth Stimulators for Regeneration of Peripheral Neurons. Adv. Funct. Mater. **29**, 1809112

30 Kiss, L., Mándity, I. M. and Fülöp, F. (2017) Highly functionalized cyclic β-amino acid moieties as promising scaffolds in peptide research and drug design. Amino acids **49**, 1441–1455

31 Bowerman, C. J. and Nilsson, B. L. (2012) Self-assembly of amphipathic β-sheet peptides: insights and applications. Biopolymers **98**, 169–184

32 Yang, J., An, H.-W. and Wang, H. (2021) Self-Assembled Peptide Drug Delivery Systems. ACS applied bio materials **4**, 24–46

33 Oosawa, F. and Kasai, M. (1962) A theory of linear and helical aggregations of macromolecules. Journal of Molecular Biology **4**, 10–21

34 Yolamanova, M., Meier, C., Shaytan, A. K., Vas, V., Bertoncini, C. W., Arnold, F., Zirafi, O., Usmani, S. M., Müller, J. A. and Sauter, D. et al. (2013) Peptide

nanofibrils boost retroviral gene transfer and provide a rapid means for concentrating viruses. Nature nanotechnology **8**, 130–136

35 Sieste, S., Mack, T., Lump, E., Hayn, M., Schütz, D., Röcker, A., Meier, C., Kaygisiz, K., Kirchhoff, F. and Knowles, T. P. J. et al. (2021) Supramolecular Peptide Nanofibrils with Optimized Sequences and Molecular Structures for Efficient Retroviral Transduction. Adv. Funct. Mater. **31**, 2009382

36 Gačanin, J., Hedrich, J., Sieste, S., Glaßer, G., Lieberwirth, I., Schilling, C., Fischer, S., Barth, H., Knöll, B. and Synatschke, C. V. et al. (2019) Autonomous Ultrafast Self-Healing Hydrogels by pH-Responsive Functional Nanofiber Gelators as Cell Matrices. Advanced materials (Deerfield Beach, Fla.) **31**, e1805044

37 Han, W., MacEwan, S. R., Chilkoti, A. and López, G. P. (2015) Bio-inspired synthesis of hybrid silica nanoparticles templated from elastin-like polypeptide micelles. Nanoscale **7**, 12038–12044

38 Weitzhandler, I., Dzuricky, M., Hoffmann, I., Garcia Quiroz, F., Gradzielski, M. and Chilkoti, A. (2017) Micellar Self-Assembly of Recombinant Resilin-/Elastin-Like Block Copolypeptides. Biomacromolecules **18**, 2419–2426

39 Huang, R., Wang, Y., Qi, W., Su, R. and He, Z. (2014) Temperature-induced reversible self-assembly of diphenylalanine peptide and the structural transition from organogel to crystalline nanowires. Nanoscale Res Lett **9**, 653

40 Fleming, S. and Ulijn, R. V. (2014) Design of nanostructures based on aromatic peptide amphiphiles. Chemical Society reviews **43**, 8150–8177

41 Gong, Z., Liu, X., Dong, J., Zhang, W., Jiang, Y., Zhang, J., Feng, W., Chen, K. and Bai, J. (2019) Transition from vesicles to nanofibres in the enzymatic self-assemblies of an amphiphilic peptide as an antitumour drug carrier. Nanoscale **11**, 15479–15486

42 Ma, H., Fei, J., Li, Q. and Li, J. (2015) Photo-induced reversible structural transition of cationic diphenylalanine peptide self-assembly. Small (Weinheim an der Bergstrasse, Germany) **11**, 1787–1791

43 Lee, H.-K., Soukasene, S., Jiang, H., Zhang, S., Feng, W. and Stupp, S. I. (2008) Light-induced self-assembly of nanofibers inside liposomes. Soft Matter **4**, 962–964

44 Cao, C., Cao, M., Fan, H., Xia, D., Xu, H. and Lu, J. R. (2012) Redox modulated hydrogelation of a self-assembling short peptide amphiphile. Chin. Sci. Bull. **57**, 4296–4303

45 Hartgerink, J. D., Beniash, E. and Stupp, S. I. (2001) Self-assembly and mineralization of peptide-amphiphile nanofibers. Science (New York, N.Y.) **294**, 1684–1688

46 Dao, H. M., Parajuli, S., Urena-Benavides, E. and Jo, S. (2020) Self-assembled peptide fibrils with pH-sensitive reversible surface-active properties. Colloid and Interface Science Communications **39**, 100325

47 Yamamoto, S., Nishimura, K., Morita, K., Kanemitsu, S., Nishida, Y., Morimoto, T., Aoi, T., Tamura, A. and Maruyama, T. (2021) Microenvironment pH-Induced Selective Cell Death for Potential Cancer Therapy Using Nanofibrous Self-Assembly of a Peptide Amphiphile. Biomacromolecules **22**, 2524–2531

48 Li, Y., Yu, H.-B., Zhang, Y., Leao, T., Glukhov, E., Pierce, M. L., Zhang, C., Kim, H., Mao, H. H. and Fang, F. et al. (2020) Pagoamide A, a Cyclic Depsipeptide Isolated from a Cultured Marine Chlorophyte, Derbesia sp., Using MS/MS-Based Molecular Networking. J. Nat. Prod. **83**, 617–625

49 Sohma, Y., Sasaki, M., Hayashi, Y., Kimura, T. and Kiso, Y. (2004) Novel and efficient synthesis of difficult sequence-containing peptides through O-N intramolecular acyl migration reaction of O-acyl isopeptides. Chemical communications (Cambridge, England), 124–125

50 Guruge, C., Ouedraogo, Y. P., Comitz, R. L., Ma, J., Losonczy, A. and Nesnas, N. (2018) Improved Synthesis of Caged Glutamate and Caging Each Functional Group. ACS chemical neuroscience **9**, 2713–2721

51 Muraoka, T., Cui, H. and Stupp, S. I. (2008) Quadruple helix formation of a photoresponsive peptide amphiphile and its light-triggered dissociation into single fibers. J. Am. Chem. Soc. **130**, 2946–2947

52 Mason, S. D. and Joyce, J. A. (2011) Proteolytic networks in cancer. Trends in cell biology **21**, 228–237

53 Pieszka, M., Han, S., Volkmann, C., Graf, R., Lieberwirth, I., Landfester, K., Ng, D. Y. W. and Weil, T. (2020) Controlled Supramolecular Assembly Inside Living Cells by Sequential Multistaged Chemical Reactions. J. Am. Chem. Soc. **142**, 15780–15789

54 Xu, Y., Zhang, L. and Lu, H. (2013) Use of boronic acid nanoparticles in glycoprotein enrichment. Methods in molecular biology (Clifton, N.J.) **951**, 45–55

55 Egawa, Y., Miki, R. and Seki, T. (2014) Colorimetric Sugar Sensing Using Boronic Acid-Substituted Azobenzenes. Materials (Basel, Switzerland) **7**, 1201–1220

56 Takeshima, K., Mizuno, K., Nakahashi, H., Aoki, H. and Kanekiyo, Y. (2017) Ratiometric Sensing of Hydrogen Peroxide Utilizing Conformational Change in Fluorescent Boronic Acid Polymers. Journal of analytical methods in chemistry **2017**, 7829438

57 Hall, D. G. (2019) Boronic acid catalysis. Chemical Society reviews **48**, 3475–3496

58 Arzt, M., Seidler, C., Ng, D. Y. W. and Weil, T. (2014) Reversible click reactions with boronic acids to build supramolecular architectures in water. Chemistry, an Asian journal **9**, 1994–2003

59 Brooks, W. L. A., Deng, C. C. and Sumerlin, B. S. (2018) Structure-Reactivity Relationships in Boronic Acid-Diol Complexation. ACS omega **3**, 17863–17870

60 Shin, S. B. Y., Almeida, R. D., Gerona-Navarro, G., Bracken, C. and Jaffrey, S. R. (2010) Assembling ligands in situ using bioorthogonal boronate ester synthesis. Chemistry & biology **17**, 1171–1176

61 Hebel, M., Riegger, A., Zegota, M. M., Kizilsavas, G., Gačanin, J., Pieszka, M., Lückerath, T., Coelho, J. A. S., Wagner, M. and Gois, P. M. P. et al. (2019) Sequence Programming with Dynamic Boronic Acid/Catechol Binary Codes. Journal of the American Chemical Society **141**, 14026–14031

62 Zegota, M. M., Müller, M. A., Lantzberg, B., Kizilsavas, G., Coelho, J. A. S., Moscariello, P., Martínez-Negro, M., Morsbach, S., Gois, P. M. P. and Wagner, M. et al. (2021) Dual stimuli-responsive dynamic covalent peptide tags: Towards sequence-controlled release in tumor-like microenvironments

63 Halo, T. L., Appelbaum, J., Hobert, E. M., Balkin, D. M. and Schepartz, A. (2009) Selective recognition of protein tetraserine motifs with a cell-permeable, pro-fluorescent bis-boronic acid. J. Am. Chem. Soc. **131**, 438–439

64 Slaughter, B. V., Khurshid, S. S., Fisher, O. Z., Khademhosseini, A. and Peppas, N. A. (2009) Hydrogels in regenerative medicine. Advanced materials (Deerfield Beach, Fla.) **21**, 3307–3329

65 Nichol, J. W., Koshy, S. T., Bae, H., Hwang, C. M., Yamanlar, S. and Khademhosseini, A. (2010) Cell-laden microengineered gelatin methacrylate hydrogels. Biomaterials **31**, 5536–5544

66 Li, H., Liu, Y., Shu, X. Z., Gray, S. D. and Prestwich, G. D. (2004) Synthesis and biological evaluation of a cross-linked hyaluronan-mitomycin C hydrogel. Biomacromolecules **5**, 895–902

67 Zhao, Y., Song, S., Ren, X., Zhang, J., Lin, Q. and Zhao, Y. (2022) Supramolecular Adhesive Hydrogels for Tissue Engineering Applications. Chemical reviews **122**, 5604–5640

68 Hou, S., Wang, X., Park, S., Jin, X. and Ma, P. X. (2015) Rapid Self-Integrating, Injectable Hydrogel for Tissue Complex Regeneration. Advanced healthcare materials **4**, 1491-5, 1423

69 Zhang, G., Lv, L., Deng, Y. and Wang, C. (2017) Self-Healing Gelatin Hydrogels Cross-Linked by Combining Multiple Hydrogen Bonding and Ionic Coordination. Macromolecular rapid communications **38**

70 Nalbandian, R. M., Henry, R. L. and Wilks, H. S. (1972) Artificial skin. II. Pluronic F-127 Silver nitrate or silver lactate gel in the treatment of thermal burns. Journal of biomedical materials research **6**, 583–590

71 Miller, B., Hansrisuk, A., Highley, C. B. and Caliari, S. R. (2021) Guest-Host Supramolecular Assembly of Injectable Hydrogel Nanofibers for Cell Encapsulation. ACS biomaterials science & engineering **7**, 4164–4174

72 Moyer, T. J., Finbloom, J. A., Chen, F., Toft, D. J., Cryns, V. L. and Stupp, S. I. (2014) pH and amphiphilic structure direct supramolecular behavior in biofunctional assemblies. J. Am. Chem. Soc. **136**, 14746–14752

73 Luo, Z., Wang, S. and Zhang, S. (2011) Fabrication of self-assembling D-form peptide nanofiber scaffold d-EAK16 for rapid hemostasis. Biomaterials **32**, 2013–2020

74 Elgersma, S. V., Ha, M., Yang, J.-L. J., Michaelis, V. K. and Unsworth, L. D. (2019) Charge and Peptide Concentration as Determinants of the Hydrogel Internal Aqueous Environment. Materials **12**

75 Han, Y., Cao, Y. and Lei, H. (2022) Dynamic Covalent Hydrogels: Strong yet Dynamic. Gels (Basel, Switzerland) **8**

76 Seow, W. Y. and Hauser, C. A. E. (2013) Tunable mechanical properties of ultrasmall peptide hydrogels by crosslinking and functionalization to achieve the 3D distribution of cells. Advanced healthcare materials **2**, 1219–1223

77 Deng, C. C., Brooks, W. L. A., Abboud, K. A. and Sumerlin, B. S. (2015) Boronic Acid-Based Hydrogels Undergo Self-Healing at Neutral and Acidic pH. ACS macro letters **4**, 220–224

78 Zhou, Q., Dong, X., Xiong, Y., Zhang, B., Lu, S., Wang, Q., Liao, Y., Yang, Y. and Wang, H. (2020) Multi-Responsive Lanthanide-Based Hydrogel with Encryption,

Naked Eye Sensing, Shape Memory, Self-Healing, and Antibacterial Activity. ACS applied materials & interfaces **12**, 28539–28549

79 Tamate, R., Takahashi, K., Ueki, T., Akimoto, A. M. and Yoshida, R. (2017) Self-Assembly of Thermoreversible Hydrogels via Molecular Recognition toward a Spatially Organized Coculture System. Biomacromolecules **18**, 281–287

80 An, H., Bo, Y., Chen, D., Wang, Y., Wang, H., He, Y. and Qin, J. (2020) Cellulose-based self-healing hydrogel through boronic ester bonds with excellent biocompatibility and conductivity. RSC Adv. **10**, 11300–11310

81 Li, Y., Yang, L., Zeng, Y., Wu, Y., Wei, Y. and Tao, L. (2019) Self-Healing Hydrogel with a Double Dynamic Network Comprising Imine and Borate Ester Linkages. Chem. Mater. **31**, 5576–5583

82 Zou, Y., Fang, Y., Meng, H., Meng, F., Deng, C., Zhang, J. and Zhong, Z. (2016) Self-crosslinkable and intracellularly decrosslinkable biodegradable micellar nanoparticles: A robust, simple and multifunctional nanoplatform for high-efficiency targeted cancer chemotherapy. Journal of controlled release : official journal of the Controlled Release Society **244**, 326–335

83 Cao, M., Wang, Y., Zhao, W., Qi, R., Han, Y., Wu, R., Wang, Y. and Xu, H. (2018) Peptide-Induced DNA Condensation into Virus-Mimicking Nanostructures. ACS applied materials & interfaces **10**, 24349–24360

84 Jain, R. K. and Stylianopoulos, T. (2010) Delivering nanomedicine to solid tumors. Nature reviews. Clinical oncology **7**, 653–664

85 Schroeder, A., Heller, D. A., Winslow, M. M., Dahlman, J. E., Pratt, G. W., Langer, R., Jacks, T. and Anderson, D. G. (2011) Treating metastatic cancer with nanotechnology. Nature reviews. Cancer **12**, 39–50

86 Koutsopoulos, S., Unsworth, L. D., Nagai, Y. and Zhang, S. (2009) Controlled release of functional proteins through designer self-assembling peptide nanofiber hydrogel scaffold. Proceedings of the National Academy of Sciences of the United States of America **106**, 4623–4628

87 Soukasene, S., Toft, D. J., Moyer, T. J., Lu, H., Lee, H.-K., Standley, S. M., Cryns, V. L. and Stupp, S. I. (2011) Antitumor activity of peptide amphiphile nanofiber-encapsulated camptothecin. ACS nano **5**, 9113–9121

88 Liu, J., Liu, J., Chu, L., Zhang, Y., Xu, H., Kong, D., Yang, Z., Yang, C. and Ding, D. (2014) Self-assembling peptide of D-amino acids boosts selectivity and

antitumor efficacy of 10-hydroxycamptothecin. ACS applied materials & interfaces **6**, 5558–5565

89 Zhao, Z., Zhang, Y., Tian, C., Yin, T. and Zhang, C. (2018) Facile dynamic one-step modular assembly based on boronic acid-diol for construction of a micellar drug delivery system. Biomaterials science **6**, 2605–2618

90 Su, J., Chen, F., Cryns, V. L. and Messersmith, P. B. (2011) Catechol polymers for pH-responsive, targeted drug delivery to cancer cells. J. Am. Chem. Soc. **133**, 11850–11853

91 Lee, C., Yang, W. and Parr, R. G. (1988) Development of the Colle-Salvetti correlation-energy formula into a functional of the electron density. Physical review. B, Condensed matter **37**, 785–789

92 Kendall, R. A., Dunning, T. H. and Harrison, R. J. (1992) Electron affinities of the first-row atoms revisited. Systematic basis sets and wave functions. The Journal of Chemical Physics **96**, 6796–6806

93 Zhao, R., So, M., Maat, H., Ray, N. J., Arisaka, F., Goto, Y., Carver, J. A. and Hall, D. (2016) Measurement of amyloid formation by turbidity assay-seeing through the cloud. Biophysical reviews **8**, 445–471

94 Yu, L., Lei, Y., Ma, Y., Liu, M., Zheng, J., Dan, D. and Gao, P. (2021) A Comprehensive Review of Fluorescence Correlation Spectroscopy. Front. Phys. **9**

95 Pattnaik, P. (2005) Surface plasmon resonance: applications in understanding receptor-ligand interaction. Applied biochemistry and biotechnology **126**, 79–92

96 Webber, M. J., Newcomb, C. J., Bitton, R. and Stupp, S. I. (2011) Switching of Self-Assembly in a Peptide Nanostructure with a Specific Enzyme. Soft Matter **7**, 9665–9672

97 Pieszka, M., Sobota, A. M., Gačanin, J., Weil, T. and Ng, D. Y. W. (2019) Orthogonally Stimulated Assembly/Disassembly of Depsipeptides by Rational Chemical Design. Chembiochem : a European journal of chemical biology **20**, 1376–1381